NTNU – Trondheim
Norwegian University of
Science and Technology

Comparison between Measured and Calculated Riser Response

Ivar Stange

Marine Technology
Submission date: June 2012
Supervisor: Bernt Johan Leira, IMT

Norwegian University of Science and Technology
Department of Marine Technology

NTNU
Norwegian University of Science and Technology
Department of Marine Technology

Master thesis, Spring 2012
for
Stud. Techn. Ivar Stange

Comparison between Measured and Calculated Riser Response

Sammenligning mellom Målt og Beregnet Respons av Stigerør

When performing response analysis and design calculations for marine risers, a large number of parameters related to representation of the loading, the floating vessel and the riser systems are required as input to the calculations. Generally, the precise values of these parameters (and even the type of calculation model which is to be applied) are not precisely known and have to be estimated e.g. based on previous experience.

There is accordingly a strong need for verification of the applied computational models as well as the relevant design parameters. Laboratory experiments play an important role in this context, but also full-scale measurements are strongly in demand. At present there seems to be only a limited number of reported results in the literature which deal with full-scale measurements of marine riser response. The objective of the present work is hence to improve this situation.

The following subjects are to be examined in this thesis:

1. A literature review is performed with respect to comparison between measured and calculated response of marine risers. Focus is on top-tensioned risers, but flexible risers are also to be considered.

2. A numerical model of the marine riser and the floater is to be established in the Riflex computer program. Information obtained from the contact person in 4Subsea is to be utilized for this purpose. A description of the connection between the physical properties of the riser and the corresponding numerical model is also to be given.

3. The available full-scale response measurements from the marine riser are to be processed such that they are on a format which is suitable for comparison with numerical calculations. This may e.g. be in the form of probability distributions, spectral density functions and standard deviations of the response.

4. The effects on the motion of the computed riser response due to change of the following parameters are to be investigated: (i)The boundary condition at the lower end of the marine riser and (ii)The directional spreading of the incoming waves (e.g. represented by means of a spreading exponent).

The work-scope may prove to be larger than initially anticipated. Subject to approval from the supervisor, topics may be deleted from the list above or reduced in extent.

In the thesis the candidate shall present his personal contribution to the resolution of problems within the scope of the thesis work. Theories and conclusions should be based on mathematical derivations and/or logic reasoning identifying the various steps in the deduction. The candidate should utilise the existing possibilities for obtaining relevant literature.

The thesis shall contain the following elements: A text defining the scope, preface, list of contents, summary, main body of thesis, conclusions with recommendations for further work, list of symbols and acronyms, references and (optional) appendices. All figures, tables and equations shall be numerated.

The supervisor may require that the candidate, at an early stage of the work, presents a written plan for the completion of the work. The plan should include a budget for the use of computer and laboratory resources which will be charged to the department. Overruns shall be reported to the supervisor.

The original contribution of the candidate and material taken from other sources shall be clearly defined. Work from other sources shall be properly referenced using an acknowledged referencing system.

The thesis shall be submitted in 3 copies:

- Signed by the candidate
- The text defining the scope included
- In bound volume(s)
- Drawings and/or computer prints which cannot be bound should be organised in a separate folder.

Supervisor: Professor Bernt J. Leira Contact person at 4Subsea: Harald Holden

Start: January 16th, 2012 Deadline: June 10th, 2012

Trondheim, 16 January 2012

Bernt J. Leira

Preface

This Master's thesis is part of the Master of Science program in Marine Structures, at the Department of Marine Technology at the Norwegian University of Science and Technology, NTNU. The work of this thesis was initiated by 4Subsea after the need for a discussion around the problem of comparing full scale data with computer simulations. I started working on my summer internship in 4Subsea in the summer of 2011 and wrote my project thesis for them in cooperation with Framo Engineering. The work on my project thesis and Master's thesis are unrelated, but I've gained a lot of useful experience from the project thesis that I've applied on my Master's thesis.

Although the challenges presented during the work has been difficult and time consuming they have given me a lot of insight into the world of marine drilling risers and the problems related to their operation and functions. Being able to study the difference in full scale riser measurements and computer simulations have taught me that there are still challenges in the time to come. I feel privileged to have worked on a topic that is of high practical relevance *right now* in the offshore industry.

I would like to thank 4Subsea for giving me the opportunity to work on such an interesting topic and especially my advisers Harald Holden and Trond Pytte for giving me all the support I needed to finish my work and spending their already precious time to give me guidance. I would also thank my advisor at the Department of Marine Technology, Prof. Bernt Johan Leira for guiding me through the whole process and for giving me feedback during my work. I would also like to thank my fellow students for valuable input pertaining to the use of LaTeX.

Trondheim, June 10^{th}, 2012

Ivar Stange

Summary

Well intervention operations can inflict large strains on a wellhead. The seabed in the North Sea is very rigid up to the point where the sea water meets the mud or sand. This is one of the reasons why wellheads operating on the Norwegian continental shelf are more exposed to fatigue damage. In search for more oil and the wish to increase the utilization rate of existing wells the oil companies drill more and more, causing more and more fatigue life consumption. The oil companies must provide sufficient documentation that the wellhead always has enough remaining fatigue life to perform a Plug and Abandon (P&A) operation.

Full scale measurements has been collected for a marine drilling riser connected to a moored Aker H-3 rig operating on a field with a depth of 325 m. The angles at the bottom of the riser above the lower marine riser package are used to calculate the consumed cumulative fatigue life using rainflow cycle counting and Miner-Palmgren summation.

A simulation model has been developed in the computer simulation program RIFLEX, which is a state of the art simulation program developed especially for slender structures such as a riser in a marine environment. The model was built with relatively conservative assumptions. This resulted on fatigue life assessments that gave a shorter operation life than what was found using the full scale measurements. Using such simulation is often the only tool available to document fatigue life consumption since full scale measurement tools are rarely installed and used. It is vital that the simulation yield reliable and correct results and as close to the true result as possible.

A series of similar simulation models were developed where we looked at the effect of taking away some of the conservatism in the original model. First we looked at the difference between a JONSWAP wave spectrum and a Torsethaugen wave spectrum. The difference lies in the assumption of that a sea state is a superposition of wind driven waves and swell waves, where the Torsethaugen use empirical data collected from the North Sea to account for the difference. A Torsethaugen is a double-peaked spectrum while the JONSWAP spectrum is a single-peaked spectrum. The difference between the two results gave little or no effect on the motion characteristics and fatigue life.

Then we introduce a directional wave spectrum, meaning that waves may be short-crested and spread around a mean wave direction. This reduced the angular motion in terms of standard deviation significantly. The reduction was between 10 % – 15 %.

It also affected the fatigue life positively. In the next model we introduced non-linear behaviour in the lower flex joint while the waves now were unidirectional. In terms of standard deviation the reduction was the same as for the model with wave spreading.

In the last comparison model we used both non-linear flex joint behaviour and wave spreading. The total reduction was again significant. For some of the simulation even up to 30 % compared to the original model. All the standard deviation from the full scale data has natural variances from data set to data set and most of the computer simulation fell within this margin of error.

For all simulation models the model was tested with different mean heading direction of the waves. The mean heading directions were 0°, 30°, 60° and 90° relative to the rig. While the full scale measurement had little correlation between the measured response direction and the weather direction, the simulation were very consistent on this matter.

Some simulations with current and support vessel offset was performed to find the effect on the standard deviation. While the presence of current damped the angular motion, the standard deviation increased with increasing support vessel offset. A discussion around the uncertainty of the true characteristics of the non-linear model explains some of the behaviour.

When comparing fatigue life the calculated fatigue life consumption became closer and closer to the measured value as we removed the conservatism. However, by a closer investigation of the angle range spectra which is used in the Miner-Palmgren summation there was found differences that need more attention. While the angle range spectrum from the full scale measurement show a close to linear relation between numbers of cycles exceeding ranges the shape for the simulated models were far from linear. In terms of the shape parameter in the Weibull distribution it was found through fitting the curve that the shape model for full scale and RIFLEX simulations were around 1.05 and 1.9, respectively.

It is this difference in shape that demands a closer investigation of the simulation models. The fact that the fatigue life approached the *true* fatigue life so closely should so far be regarded as a coincidence and not a result of good model approximations.

It was also found that the full scale motion for some of the time series are low frequency dominated, i.e. high energy in oscillating components with a frequency outside the wave spectrum. Some peak periods reach periods over a minute or even two. This is an effect that is unaccounted for in the models presented in this thesis.

Sammendrag

Brønnintervensjoner kan påføre store påkjenninger på et brønnhode. Havbunnen utenfor Norge er veldig stiv hele veien opp til punktet hvor havbunn møter havvann. Dette er en av grunnene til at brønnhoder som opererer på den norske kontinentalsokkelen er mer utsatt for utmattelsesbrudd. I letingen etter mer olje og ønske om å utnytte statig mer av hver brønn, borer oljeselskapene mer og mer. Oljeselskapet må alltid kunne dokumentere at brønnhodet har tilfredsstillende nok levetid til å utføre en "plugg og forlat"-operasjon.

Målinger har blitt samlet inn for fullskala borestigerørsrespons som er koblet til en oppankret Aker H-3 rigg som opererer på et felt med en vanndybde på 325 m. Vinklene nederst på stigerøret over den nedre stigerørspakken er brukt for å beregne den akkumulerte utmattelsesskaden ved bruk av rainflow telling og Miner-Palmgren-summering.

En simuleringsmodell har blitt utviklet i datasimuleringsverktøyet RIFLEX, som er et avansert simuleringsprogram spesielt utviklet for slanke strukturer som blant annet stigerør i et marint miljø. Modellen ble bygd med relativt konservative antagelser. Dette resulterte i vurderinger av akkumulert utmattelsesskade som var mye høyere enn den reelle verdien. Slike simuleringer er dessverre ofte det eneste tilgjengelige verktøyet for å dokumentere gjenværende utmatting siden fullskala stigerør sjelden blir installert med måleinstrumenter. Det er derfor av stor betydning at slike simuleringer gir et så korrekt bilde av det reelle resultatet som mulig.

En rekke lignende simuleringsmodeller ble utviklet hvor vi så på effekten av å ta bort konservativismen fra den opprinnelige modellen. Først så vi på forskjellen i responsen ved å bruke et JONSWAP bølgespekter og Torsethaugen bølgespekter. Forskjellen ligger i antagelsen om at en sjøtilstand består av to sjøtilstander som opptrer samtidig, altså vinddrevne bølger og dønninger. Bølgespekterer til Torsethaugen har to topper istedenfor en enkelt topp. Forskjellen mellom de to simularingene gav liten forskjell i resultatene.

Så introduserte vi bølgespektre med retningsspredning. Det betyr at bølgene er kortkammede og har en spredning om en gjennomsnittlig innkommende retning. Dette reduserte stigerørsresponsen (vinkel) i form av standardavvik betraktelig. Reduksjonen lå på mellom 10 % – 15 %. Det påvirket også utmattelsesberegningene i positiv forstand. I den neste modellen introduserte vi ikke-lineær stivhet av den nedre fleksible leddet, mens bølgespredningen ble satt tilbake til den opprinnelige uten spredning. I form av standardavvik ble reduksjonen omtrent den samme som for modellen med

bølgespredning.

I den siste sammenligningsmodellen ble både bølgespredning og ikke-lineær stivhet i det nedre fleksible leddet brukt. Den totale reduksjonen av responsen var signifikant, og i noen tilfeller opp til 30 % sammenlignet med den opprinnelige RIFLEX-modellen. Alle standardavvikene fra fullskaladataene varierer naturlig og de aller fleste simulerte standardavvik falt innenfor disse feilmarginene.

For alle simuleringsmodellene ble modellene testet med forskjellige hovedretninger på bølgene. Hovedretningene som ble bruk var 0°, 30°, 60° og 90°. Fullskala målingene viste at det var liten sammenheng mellom hovedretningen for vinkelresponsen i forhold til værretningen. Derimot viste simuleringene stor sammenheng. Det vil si at hovedretningen for responsen hadde samme retning som innkommende bølgeretning.

Så ble noen simuleringer gjort med strøm og noen der riggen var forskjøvet for å finne påvirkningen disse hendelsene har på standardavviket. Strøm sørget for å dempe vinkelresponsen, mens standardavviket økte når riggen ble forskjøvet. Påvirkningen av det ikke-lineære leddet forklarer deler av denne oppførselen.

Når vi sammenligner utmattingen så vil beregnet akkumulert utmattelsesskade komme nærmere og nærmere den målte verdien etterhvert som vi fjernet de konservative antagelsene. Men etter nærmere etterforskning så vi at vinkelbreddespekteret som blir brukt i Miner-Palmgren-summeringen var ganske forskjellige. Der vinkelbreddespekteret for de målte dataene i fullskala gav en nesten lineær sammenheng (i lin-log skala) fikk vi langt ifra dette for simuleringene. I form av formparameteren i en Weibullfordeling som ble funnet gjennom tilpasning fant vi formfaktorer for henholdsvis fullskalamålinger og RIFLEX-simularinger på 1.05 og 1.9.

Det er denne forskjellen i form som gjør at det trengs flere undersøkelser of simuleringsmodellene. Det faktum at utmattelsesskaden nærmet seg den *sanne* verdien så bra bør ses på som en tilfeldighet og ikke som et resultat av gode modeller.

Det ble også funnet at måleseriene fra fullskaladataene inneholdt mye lavfrekvente bevegelser. Det vil si at en stor andel av den totale bevegelsesenergien finnes i frekvensområdet utenfor frekvensområdet for bølgene. Enkelte av topperiodene var på flere minutter. Dette er en effekt som det ikke ble tatt hensyn til da modellene ble laget for denne oppgaven.

Contents

1 Introduction **1**
- 1.1 Motivation . . . 1
- 1.2 Background . . . 2
- 1.3 Approach . . . 3
- 1.4 Report Organisation . . . 4

2 Marine Riser Setup **5**
- 2.1 Overview . . . 5
  - 2.1.1 Rig and Weather Directions . . . 5
  - 2.1.2 Marine Riser Setup . . . 5
- 2.2 Sensor Setup . . . 11
- 2.3 Riflex Model Structure . . . 13
  - 2.3.1 Wellhead . . . 13
  - 2.3.2 BOP . . . 13
  - 2.3.3 Marine Riser . . . 13
  - 2.3.4 Heave Compensator . . . 14
  - 2.3.5 Model Data . . . 14
- 2.4 Acting Forces . . . 14

3 Stochastic Theory **17**
- 3.1 Stochastic Process . . . 17
  - 3.1.1 Definition . . . 17
  - 3.1.2 Multivariate Normal Distribution . . . 18
- 3.2 Spectral Density . . . 20
  - 3.2.1 Definition . . . 20
  - 3.2.2 Spectral Moments . . . 21
- 3.3 Short-Term Statistics . . . 22
- 3.4 Assumptions . . . 23
  - 3.4.1 Linear Assumptions . . . 23
  - 3.4.2 Non-Linear Assumptions . . . 24

4 Fatigue Theory **25**
- 4.1 Cycles to Failure . . . 25
  - 4.1.1 Constant Amplitude Loading . . . 25
  - 4.1.2 Variable Amplitude Loading . . . 25
- 4.2 θ-N Curve . . . 26

4.2.1 Determination of Constants in Two-Slope θ-N Curve 27
4.2.2 Closed Form Fatigue Life Equations 28
4.2.3 Wide Banded Stress History 29
4.3 Cycle Counting and Fatigue 30
4.3.1 Weibull Stress Range Distribution 31
4.3.2 Rainflow Counting 31

5 Full Scale Data Analyses **35**
5.1 Environmental Parameters 35
5.2 Sampled Data 37
5.2.1 Data Files 37
5.2.2 Techniques 37
5.2.3 Normal Distribution Probability Paper 37
5.3 Multi-Directional Fatigue 39
5.3.1 Control Planes 39
5.3.2 Governing Response Angle 40
5.4 Results 42
5.4.1 Selecting Representative Data 42
5.4.2 Standard Deviation and Ratio 44
5.4.3 Power Spectra 48
5.4.4 Bandwidth of Response Spectra 50
5.4.5 Angle Range and Fatigue 52
5.4.6 Short-term Angle Range 54

6 Simulation Models **59**
6.1 Literature Review 59
6.2 Wave Spectra 61
6.2.1 Unidirectional Spactra (Long-Crested Waves) 61
6.2.2 Multi-Directional Spectra (Short-Crested Waves) 64
6.3 Sea States 65
6.4 Simulation Time 66
6.5 Eigenfrequencies 67
6.6 Non-Linear Effects 68
6.6.1 Bernoulli's Velocity Term 68
6.6.2 Boundary Conditions 71
6.7 Support Vessel Offset 72

7 Simulation Results **73**
7.1 Unidirectional Single-Peaked Waves 74
7.1.1 Standard Deviation 74
7.1.2 Spectrum and Broadness 75
7.1.3 Fatigue 76
7.1.4 Short-Term Angle Spectra 77
7.2 Unidirectional Torsethaugen Waves 78
7.2.1 Standard Deviation 78
7.2.2 Spectrum and Broadness 79

7.2.3 Fatigue . . . 80
7.2.4 Short-Term Angle Spectra . . . 81
7.3 Unidirectional Torsethaugen Waves with Non-Linear Boundary Conditions 81
7.3.1 Standard Deviation . . . 81
7.3.2 Spectrum and Broadness . . . 82
7.3.3 Fatigue . . . 85
7.3.4 Short-Term Angle Spectra . . . 85
7.4 Torsethaugen Waves with Wave Spreading . . . 86
7.4.1 Standard Deviation . . . 86
7.4.2 Spectrum and Broadness . . . 88
7.4.3 Fatigue . . . 89
7.4.4 Short-Term Angle Spectra . . . 90
7.5 Torsethaugen Waves with Non-Linear Boundary Conditions and Wave Spreading . . . 90
7.5.1 Standard Deviation . . . 90
7.5.2 Spectrum and Broadness . . . 92
7.5.3 Fatigue . . . 93
7.5.4 Short-Term Angle Spectra . . . 94
7.6 Unidirectional Torsethaugen Waves with Current . . . 94
7.6.1 Standard Deviation . . . 94
7.6.2 Spectrum and Broadness . . . 95
7.6.3 Short-Term Angle Spectra . . . 98
7.7 Unidirectional Torsethaugen Waves with Non-Linear Boundary Conditions and Rig Offset . . . 98
7.7.1 Standard Deviation . . . 98
7.7.2 Spectrum and Broadness . . . 100
7.7.3 Short-Term Angle Spectra . . . 101

8 Result Comparison and Discussion 103
8.1 Response Comparison . . . 103
8.1.1 Standard Deviation Comparison . . . 103
8.1.2 Miner-Palmgren Summation Comparison . . . 106
8.1.3 Weibull Fit Damage Comparison . . . 109
8.1.4 Short-term Angle Spectrum Comparison . . . 110
8.1.5 Spectrum and Spectrum Broadness . . . 112
8.2 Result Assessment . . . 112
8.2.1 Modification of the Model . . . 112
8.2.2 Long-Term Angle Range Spectrum Differences . . . 112
8.2.3 Short-term Angle Range Spectrum Differences . . . 113
8.2.4 Support Vessel Motion . . . 113
8.2.5 True Non-Linear Flex Joint . . . 114
8.2.6 Wave Spreading . . . 114
8.2.7 Current . . . 114
8.2.8 Heave Compensator behaviour . . . 115

Conclusion 117

Recommendations for Further Work **119**

References **122**

A Marine Riser Static Displacement **I**

B Tabulated θ-N Curve Values **V**

Nomenclature

Abbreviations

BOP Blowout Preventer

DFT Discrete Fourier Transform

FFT Fast Fourier Transform

JONSWAP Joint North Sea Wave Project

LFJ Lower Flex Joint

LMRP Lower Marine Riser Package

MRU Motion Reference Unit

MSL Mean Sea Level

NORA10 Norwegian Reanalysis, 10x10 km grid

P&A Plug and Abandon

REX 4Subsea Riser Expert System

RFC Rainflow Counting

UFJ Upper Flex Joint

XT Christmas Tree

Greek

α Scale parameter in Weibull distribution

β Shape parameter in Weibull distribution

ϵ Broadness parameter

ϵ_{mc} Broadness parameter determined from negative maxima counting

ϵ_s Broadness parameter determined from spectral analysis

η Standard deviation normalised maxima

γ Peakedness parameter in JONSWAP spectra

$\mathbf{\Sigma}$ Covariance matrix

μ Mean value in a Gaussian process

ϕ Angle shift between control plane and xz-plane

σ Standard deviation in a Gaussian process

θ Lower Flex Joint Angle

θ_ϕ Transformed angles about the z-axis

θ_{ij} Riser angle in the ij-plane

ζ Ratio between maximum and minimum standard deviation

Roman

ΔS Stress range

a_i Fluid acceleration in the i-th direction

C_D Drag coefficient

C_M Added mass corrected coefficient

D Diameter

H_S Significant wave height

I_{ii} Rotational inertia about i axis

m Inverse negative slope in the (log-log) S-N curve

m_i i-th spectral moment

n Number of stress cycles equal to or exceeding S_r

n_0 Total number of stress cycles

r Ratio between negative maxima and all maxima

$R(\tau)$ Autocorrelation function

$S(w)$	Spectral density function
$S_{r,0}$	Stress range which is exceeded once out of n_0 stress cycles
T_m	Mean period
T_P	Peak period
T_z	Mean zero crossing period
u	Relative fluid velocity
k	Wave number

List of Figures

2.1 RIFLEX' definition of co-ordinate system and corresponding angles (Marintek, 2010) . . . 6
2.2 Marine riser model structure . . . 9
2.3 Marine riser overview (Framnes and Gleditsch, 1994) . . . 10
2.4 Schematic overview of the connection between the well and the marine riser. The wellhead is connected to the Blowout Preventer and is then connected to the marine drilling riser through the lower marine riser package. . . . 10
2.5 Blowout Preventer diagram showing different types of rams. (a) blind ram (b) pipe ram and (c) shear ram. (Wikipedia, 2012) . . . 10
2.6 REX system for the marine riser (4Subsea, 2012). . . . 12
2.7 Sensor placement above and below the Lower Flex Joint. . . . 12
2.8 A simplified schematic model of the forces acting on the marine riser, BOP and the wellhead. . . . 15
2.9 The tensile and shear forces at the end of the marine riser can be decomposed into horizontal of vertical forces. . . . 15

3.1 Bivariate normal distribution (Wikimedia Commons) Equidensity contour lines would be shaped as ellipses. Principal axes and variances are here marked by the arrows. . . . 19
3.2 Example of statistical description of angle response . . . 20
3.3 Example of a Gaussian process (Myrhaug, 2005). The irregular realisation of the motion is the superposition of an infinite number of regular sine curves with varying amplitudes and random uniformly distributed phase angles. . . . 22
3.4 Distribution of maxima for different broadnesses . . . 23

4.1 Cycles to failure. The curve is bi-linear when it is plotted in a log-log scale. 26
4.2 Correction factor for broad banded fatigue assessment . . . 30
4.3 Example load history . . . 30
4.4 Normalised stress spectrum represented by the Weibull distribution with different shape parameters. . . . 31
4.5 Stress-strain cycles. The signal is plotted vertically with time. The variation in strain amplitude makes the rainflow counting method suitable for broad banded processes. . . . 32
4.6 Creation and release of raindrop. . . . 33

4.7 An example of rainflow for one side only. A raindrop is created inside each valley and is released on the succeeding peak. 34

5.1 Sea state directions at Haltenbanken 36
5.2 Normal distribution probability paper example. For a perfectly normal distribution the data would form a straight line. The coefficient of determination yield the "goodness of fit" of the line. 38
5.3 Example of angle path and projecting planes 39
5.4 Spread and distribution of the relative angle between the weather and riser response 41
5.5 Illustration of response angle relations seen from above 41
5.6 Standard deviations for $T_P = 12\,\text{m}$. The blue square indicated the mean of all sampled standard deviations and the error bars indicates the natural variances between all the standard deviation from the same sea state. . . 42
5.7 Occurences of directions for different sea states within measured period . 44
5.8 Standard deviation and ratio, H_S: 2, T_P: 9 45
5.9 Standard deviation and ratio, H_S: 2, T_P: 10 45
5.10 Standard deviation and ratio, H_S: 4, T_P: 10 46
5.11 Standard deviation and ratio, H_S: 2, T_P: 12 46
5.12 Standard deviation and ratio, H_S: 4, T_P: 12 47
5.13 Standard deviation and ratio, H_S: 6, T_P: 12 47
5.14 Standard deviation for the selected sea states. This illustrates that we expect the angle response to increase for higher significant wave heights. 48
5.15 Two and two sample hours within same 3-hour window, H_S: 4 m, T_P: 10 s. The overall shape is different, but the standard deviation is still the same. 49
5.16 Spread of broadness parameter for all measurements. The majority of the measured broadnesses are very high. 50
5.17 Examples of fitted Rice distributions for different ϵ. The plots show a good consistency between the two methods of determining the broadness. 51
5.18 Angle spectrum from fullscale analysis where all 1180 time series are used. The Weibull fit follows the blocks very well. The figure represent the control plane with the highest accumulated fatigue damage. 52
5.19 Angle spectrum from fullscale analysis, θ, selected sea states. The figure represent the control plane with the highest accumulated fatigue damage. 53
5.20 Cumulative damage for each block in Miner-Palmgren summation 55
5.21 The share of damage for all cycles when all cycles above $\Delta\theta_i$ are neglected 56
5.22 Power spectra for the xz angle for three succeeding hours. All three spectra have most of the energy focused in the wave frequency domain and low energy for low frequencies. H_S: 4, T_P:10. 56
5.23 Full scale angle range spectrum for 3-hour time series. The time series are the same as for the angle spectra shown in figure 5.22 57
5.24 Power spectra for the xz angle for three succeeding hours. All three spectra have most of the energy focused in low frequency domain and low energy in the wave frequency range. H_S: 4, T_P:10. 57

5.25 Full scale angle range spectrum for 3-hour time series. The time series are the same as for the angle spectra shown in figure 5.24 58

6.1 Steep wave riser configuration 61
6.2 Riser response for two different heading directions 62
6.3 Illustration of directional spectra (Myrhaug, 2007) 64
6.4 Stability of standard deviation and convergence 67
6.5 The fourth eigenmode from static RIFLEX calculations. As for most slender one-dimensional structures it nearly follows a perfect sine curve. . 68
6.6 The average drag force and relative component contribution. The mean force from the wave alone is always zero, and for the current alone should give a 1-to-1 relation. The combined effect increases the average drag force. 70
6.7 Characteristics between the linear and non-linear spring. This shows the static stiffness relation. The true stiffness in a dynamic context is different than this figure. 71
6.8 Support vessel offset 72

7.1 The effect of Tp and Hs on the standard deviation 75
7.2 Spectra for global xz- and yz-planes. The spectra is from a simulation with $H_S = 4$ m and $T_P = 10$ s. A peak near $\omega = 0.8$ is clearly visible, which is close to the eigenfrequency in the 4^{th} mode. 75
7.3 The scattering of ϵ for unidirectional single-peaked waves 76
7.4 Angle spectra for unidirectional single-peaked waves with different heading 77
7.5 Short-term angle range spectrum for unidirectional JONSWAP waves . . 77
7.6 The effect of Tp and Hs on the standard deviation (Torsethaugen spectrum) 78
7.7 Spectra for global xz- and yz-planes for unidirectional Torsethaugen waves. The spectra is from a simulation with $H_S = 4$ m and $T_P = 10$ s. Two peaks near $\omega = 0.6$ and $\omega = 0.8$ are clearly visible, which is close to the eigenfrequency in the 3^{rd} and 4^{th} mode. 79
7.8 The scattering of ϵ for unidirectional Torsethaugen waves 80
7.9 Angle spectra for unidirectional Torsethaugen waves with different heading 80
7.10 Short-term angle range spectrum for unidirectional Torsethaugen waves . 81
7.11 The effect of Tp and Hs on the standard deviation (Torsethaugen spectrum, non-linear boundary condition) 82
7.12 Spectra for global xz- and yz-planes for Torsethaugen waves with non-linear boundary conditions. The spectra is from a simulation with $H_S = 4$ m and $T_P = 10$ s. Two peaks near $\omega = 0.6$ and $\omega = 0.8$ are clearly visible, which is close to the eigenfrequency in the 3^{rd} and 4^{th} mode. 83
7.13 The scattering of ϵ for unidirectional Torsethaugen waves and non-linear boundary condition 84
7.14 Angle spectra for unidirectional Torsethaugen waves with different heading and non-linear boundary conditions 85
7.15 Short-term angle range spectrum for unidirectional Torsethaugen waves with non-linear flex joint 86
7.16 The effect of Tp and Hs on the standard deviation (Torsethaugen spectrum with wave spreading) 87

7.17 Spectra for global xz- and yz-planes for Torsethaugen waves with directional spreading. The spectra is from a simulation with $H_S = 4$ m and $T_P = 10$ s. Two peaks near $\omega = 0.6$ and $\omega = 0.8$ are clearly visible, which is close to the eigenfrequency in the 3rd and 4th mode. 88
7.18 The scattering of ϵ for unidirectional Torsethaugen waves with wave spreading 89
7.19 Angle spectra for unidirectional Torsethaugen waves with different heading and wave spreading 89
7.20 Short-term angle range spectrum for Torsethaugen waves with wave spreading 90
7.21 The effect of Tp and Hs on the standard deviation (Torsethaugen spectrum with wave spreading and non-linear boundary condition) 91
7.22 Spectra for global xz- and yz-planes for Torsethaugen waves with directional spreading and non-linear flex joint. The spectra is from a simulation with $H_S = 4$ m and $T_P = 10$ s. Two peaks near $\omega = 0.6$ and $\omega = 0.8$ are clearly visible, which is close to the eigenfrequency in the 3rd and 4th mode. 92
7.23 The scattering of ϵ for Torsethaugen waves and non-linear boundary condition 93
7.24 Angle spectra for unidirectional Torsethaugen waves with different heading, wave spreading and non-linear boundary conditions 93
7.25 Short-term angle range spectrum for Torsethaugen waves with non-linear flex joint and wave spreading 94
7.26 Effect of current on standard deviation. The current heading is relative to the rig's local x axis. A current from the side of the rig yields less damping of the angle response. 96
7.27 Static configuration of marine riser in current velocity of 0.56 m/s. The current is headed in the rig's local x direction, and the plot is plotted with respect to global xz and yz planes. 96
7.28 Spectra for global xz- and yz-planes for unidirectional Torsethaugen waves with non-linear boundary conditions. The spectra is from a simulation with $H_S = 4$ m and $T_P = 10$ s. 97
7.29 The scattering of ϵ for unidirectional Torsethaugen waves with current . . 97
7.30 Current effect on the short-term angle range spectra. For increasing currents the spectrum becomes more similar to the shape of the full scale angle spectrum. 98
7.31 Angles for LFJ for vessel offset. The blue line is the average angle position of the riser. The red point is the static angle found from the calculations from the Excel sheet (See appendix A). 99
7.32 Standard deviation for support vessel offset. The local x axis is in the same heading direction as the rig. 100
7.33 Spectra for global xz- and yz-planes for unidirectional Torsethaugen waves with support vessel offset. The spectra is from a simulation with $H_S = 4$ m, $T_P = 10$ s and an offset of 18 m in the vessel local x axis. . . 100
7.34 The scattering of ϵ for unidirectional Torsethaugen waves with offset . . . 101
7.35 Support vessel offset effect on the angle range spectrum. 102

8.1 Comparison of standard deviation from RIFLEX and full scale data. The horizontal solid black line is the averaged standard deviations from the full scale data and the dashed black lines are the statistical spreading of the standard deviation. 105
8.2 Comparison between the Miner-Palmgren summation blocks from RIFLEX and full scale analyses 108
8.3 Comparison between short-term angle range spectra between full scale and computer simulations. The simulation time is 3 hours and all time series have the same sea state parameters. $H_S = 4$ m, $T_P = 10$ s. 111

List of Tables

2.1 Dimension values for the marine riser. 14

5.1 Long term sea states observations 36
5.2 Sea states with measured data in period 43
5.3 Selected sea states 43
5.4 Standard deviations and ratios for the selected sea states. 44
5.5 Cumulative damage for each control plane 53
5.6 Cumulative damage for each control plane for selected sea states 54

6.1 Calculated eigenfrequencies from RIFLEX 67

7.1 Overview over the effects that are used in the simulation for each category. 74
7.2 Standard deviation and ratios for unidirectional single-peaked waves with different heading. σ is the standard deviation of the angle motion and ζ is the ratio between the minimum and maximum standard deviation (see section 5.3.2). 74
7.3 Average broadness for unidirectional single-peaked spectra 76
7.4 Cumulative damage and values for both block method and closed form solution in unidirectional single-peaked waves. 77
7.5 Standard deviation and ratios for unidirectional Torsethaugen waves with different heading. σ is the standard deviation of the angle motion and ζ is the ratio between the minimum and maximum standard deviation (see section 5.3.2). 78
7.6 Average broadness for unidirectional Torsethaugen spectra 79
7.7 Cumulative damage and values for both block method and closed form solution in unidirectional Torsethaugen waves. 81
7.8 Standard deviation and ratios for unidirectional Torsethaugen waves with different heading and implemented non-linear boundary condition. σ is the standard deviation of the angle motion and ζ is the ratio between the minimum and maximum standard deviation (see section 5.3.2). 82
7.9 Average broadness for unidirectional Torsethaugen spectra and non-linear boundary condition 83
7.10 Cumulative damage and values for both block method and closed form solution in unidirectional Torsethaugen waves and non-linear boundary conditions. 85

7.11 Standard deviation and ratios for Torsethaugen waves with spreading. σ is the standard deviation of the angle motion and ζ is the ratio between the minimum and maximum standard deviation (see section 5.3.2). . . . 86
7.12 Average broadness for unidirectional Torsethaugen spectra with wave spreading 88
7.13 Cumulative damage and values for both block method and closed form solution in unidirectional Torsethaugen waves and wave spreading. 90
7.14 Standard deviation and ratios for unidirectional Torsethaugen waves with wave spreading and implemented non-linear boundary condition. σ is the standard deviation of the angle motion and ζ is the ratio between the minimum and maximum standard deviation (see section 5.3.2). 91
7.15 Average broadness for Torsethaugen spectra with wave spreading and non-linear boundary condition 92
7.16 Cumulative damage and values for both block method and closed form solution in unidirectional Torsethaugen waves, wave spreading and non-linear boundary conditions. 94
7.17 Standard deviation and ratios for unidirectional Torsethaugen waves with current, Hs 4 m Tp 10 s. σ is the standard deviation of the angle motion and ζ is the ratio between the minimum and maximum standard deviation (see section 5.3.2). 95
7.18 Average broadness for unidirectional Torsethaugen spectra with current . 96
7.19 Standard deviation for unidirectional Torsethaugen waves and non-linear boundary condition and support vessel offset, $H_S = 4$ and $T_P = 10$. σ is the standard deviation of the angle motion. 99
7.20 Average broadness for unidirectional Torsethaugen spectra with offset . . 101

8.1 Cumulative damage for each simulation model compared to full scale damage using Miner-Palmgren summation 106
8.2 Cumulative damage for each simulation model compared to full scale damage using closed form Weibull solution 109
8.3 Comparison of Miner-Palmgren sum damage and Weibull fit closed form solution damage. 109

Chapter 1

Introduction

1.1 Motivation

This report is the result of a Master's Thesis in Marine Technology at the Norwegian University of Science and Technology in the spring of 2012. The work of this thesis was initiated by 4Subsea after the need for a discussion around the problem of comparing full scale data with computer simulations.

In the process of creating a computer model the user will always be confronted with the time spent on the model with respect to the accuracy of the model. When presented to an unknown factor, the user will assume a conservative value to be on the safe side. This thesis will target the issue between physics in the real world and the conservative assumptions made in the model. Narrowing the gap between a theoretical model and a real-world application is of huge interest.

This thesis will specifically take a closer look at the fatigue problem on wellheads during wellhead intervention operations. The consumed fatigue life during these operations can be responsible for the majority of its total fatigue life. Being able to document the remaining life with as accurate assumptions as possible gives a great advantage.

The investments in each and every well are massive. The wellhead is the interface between the well and the drilling pipe in the sea. When closing a well the operator must provide the documentation that the wellhead has sufficient life remaining to perform Plug and Abandon (P&A) operation without failing. To make the most out of each well the operators seek to utilize more and more of the wellhead. Having the best knowledge to determine the spent fatigue life on the wellhead is therefore of great importance. This means that one need to know the complete system setup, how all structural parts interacts with each other, and how they are excited by the environmental actions.

The important structure parts which this thesis will look closer at are the wellhead, BOP and its drilling riser. Even though the drilling riser is considered a *vertical* riser it isn't perfectly so. A moving surface vessel such as a drilling rig will be set in motion by wind, waves and currents. In turn, this will yield a moment at the top of the BOP and

the wellhead will be exposed to fatigue damage. The wellhead will take more fatigue damage during the drilling process than it will during the rest of its total lifetime.

For the Norwegian continental shelf the question about wellhead fatigue is drastically more interesting compared to other oil rich areas, e.g. the Mexico Gulf. The most obvious reason is that the Mexico Gulf is far more benign than the seas outside Norway. But the less obvious one is the composition of the sea floor and the sediments. From the very top the seabed on the Norwegian continental shelf is very stiff yielding very high stress concentrations near the sea-to-seabed transition. While in other areas the transition is more smooth, having soft sediments at the top with a gradually increasing stiffness as you go deeper underground. Because of this, the fatigue life in e.g. the Mexico Gulf is almost not of interest at all for the drilling operation, or for the oil extraction process at all.

The increasing demand of increased oil recover increases the wellhead intervention. Each well increases in complexity and new technology allows for longer horizontal drilling lengths. All this will give more days of intervention on the wellhead. In the 90's and the beginning of the new millennium the average height could be 10 m – 12 m and weighing around 250 Te, they can now be up to 16 m – 18 m and weighing 400 Te or even more. This increase in mass will also affect the fatigue life time of the wellhead. The oil companies also increase their demands of how many drilling days one hole should endure regardless of the weather.

1.2 Background

Petroleum has been exploited by mankind for thousands of years. One of the earliest documented uses of petroleum by mankind is more than 4,000 years old. It was used to make asphalt employed in the construction of walls and towers of Babylon. Oil wells were first drilled in China in 347 AD. They were up to 240 m deep and were drilled using bits attached to bamboo poles. The oil was then burned to evaporate brine to produce salt.

The real jump in oil production came with the industrial revolution when it became an important fuel for combustion engines and for heating. After decades of extracting oil from below the sea the demand is still increasing. The demand for oil will also be present in decades to come. An important part of the oil industry is to locate new sources of hydrocarbons. Drilling rigs are all over the world drilling around the clock in the search for these valuable substances.

Naturally, the easiest accessible oil field has already been depleted, i.e. within the acceptable utilization ratio with respect to cost. New field are developed at greater water depths and in harsher environments such as Arctic areas. In turn, this means that every well is even more complex and more expensive to develop. To extract more oil and increase the margin per drill hole is therefore desirable.

1.3 Approach

Using full scale measurements as a reference blueprint for the motion response we can compare different simulation models with the data in order to determine any errors implied by the model assumptions. The riser is equipped with Motion Reference Units (MRU) in order to measure the translational and rotational accelerations of the riser response. The accelerations are then integrated to find the displacements. An overview of the system setup is given in section 2.1. The fatigue life is calculated using the angle of the riser at the Lower Flex Joint (LFJ) which is positioned directly above the Lower Marine Riser Package (LMRP).

The models are simulated in RIFLEX which is a computer program developed by Marintek, a sub-division of the research organisation SINTEF. RIFLEX was developed as a tool for analysis of flexible marine riser systems, but is as well suited for any type of slender structure, such as mooring lines, umbilicals, and also for steel pipelines and conventional risers (Marintek, 2010).

The original model will be tested against the full scale measurements. Each model will then be adjusted with a change in the simulation one by one. This way we can determine the effect each of them have on the total response and how this affects the total spent lifetime of the wellhead.

Both statistical methods and direct cycle counting will be explained and utilised to compare the response and fatigue life calculations.

1.4 Report Organisation

1. Introduction
Gives an introduction to the problem in this report, the motivation and approach.

2. Marine Riser Setup
An overview over the system that will be analysed in this report. The marine riser is schematically presented together with the relevant sensors and modelling.

3. Stochastic Theory
A basic introduction to the stochastic theory and concepts that are used to do the statistical calculations.

4. Fatigue Theory
A short introduction to the fatigue theory. Miner-Palmgren sum and closed form fatigue equations are presented here.

5. Full Scale Data Analyses
All the analyses and calculations of data from the full scale measurements are collected in this chapter. This includes analyses of the angle motion of the LFJ, fatigue calculations, power spectra and angle range spectra.

6. Simulation Models
This chapter gives an explanation to the theoretical approach of the simulation model. It explains the simplification in the conservatism in the different simulation models, etc.

7. Simulation Results
All the analyses and calculations of data from the simulation calculations are collected in this chapter. This includes analyses of the angle motion of the LFJ, fatigue calculations, power spectra and angle range spectra.

8. Result Comparison and Discussion
An assessment of the full scale and simulation model calculation.

Conclusion
The conclusions of the work in this report.

Recommendations for Further Work
Work and results that demands further investigation. Proposals of better ways to approach the problem presented in the introduction.

Chapter 2

Marine Riser Setup

2.1 Overview

2.1.1 Rig and Weather Directions

The rig is an Aker H-3 rig built in 1977. Its heading direction relative to north is 250° where positive direction is clockwise. The rig is using anchor lines for station keeping. The water depth is 325 m.

The weather data is provided by the Norwegian Reanalysis (NORA10), which is a series of wave hindcast developed by the Norwegian Meteorological Institute. It produces three hourly wave fields at 10 km grid spacing (Øyvind Breivik et al., 2011).

The simulation tool used in this thesis, RIFLEX, uses another definition of positive angles. As shown in figure 2.1 the counter-clockwise direction is regarded as positive. The angle in the xy plane, i.e. angles the horizontal plane is relative to the global x axis.

2.1.2 Marine Riser Setup

System

The marine riser structure overview is shown in figure 2.2.

During the drilling operation the wellhead is connected to the Blowout Preventer (BOP) which again is connected to the riser through the Lower Marine Riser Package (LMRP) (see figure 2.4). The wellhead provides the interface for the BOP to connect to during drilling and for the Christmas tree (XT) during production. The LMRP acts as the interface between the riser and the BOP. It also consists of a flex joint to remove most of the concentrated moment stresses.

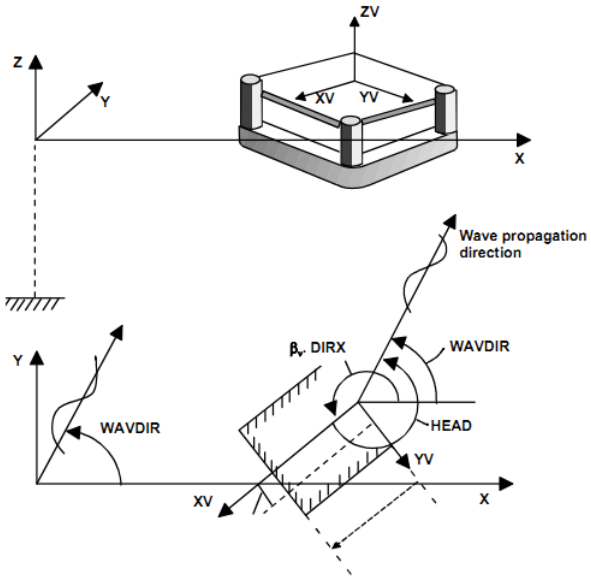

Figure 2.1: RIFLEX' definition of co-ordinate system and corresponding angles (Marintek, 2010)

The direction of the seabed template is arbitrary. The direction of the BOP is restricted to align with the template and the BOP may have one of 4 different directions relative to the template. The acceleration sensor is located at the port side of the BOP. The orientation of the wellhead and BOP is unknown. The further calculations of the riser's angle response will be relative to the direction giving the *highest* response.

The top end of the riser is connected to a heave compensator on the rig. To avoid the possibility of buckling and in case the rig need to disconnect from the BOP for any reason the riser is always tensioned. The neutral axis is usually located somewhere on the BOP, but never above. If part of the LMRP was in compression it would be difficult to disconnect it in the event of an emergency.

Joints

One can divide the variety of joints into separate categories; flex joints, buoyancy joints, slick joints, pup joints and the inner/outer barrel (Framnes and Gleditsch, 1994) and (Wikipedia, 2012).

The *flex joints* are typically $1 - 2\,\mathrm{m}$. The flex joint is much more elastic than the rest of the riser. It allows the riser to rotate more freely so that moments aren't transferred completely. A stiffer flex joint will transfer more moment and may yield a higher concentration of stresses nearby.

Buoyancy joints makes the riser less heavy. The riser is heavier than sea water and all the compression forces will gather near the bottom and all the tension near the top of the marine riser. The buoyancy joints will spread the forces along the riser so that the effective tension is positive and as smoothly distributed as possible along the whole

length.

The *slick joints* are sections with exactly the same dimensions as the buoyancy elements, but there are no buoyancy tanks or elements attached to it.

Pup joints are steel sections of variable lengths to adjust the total riser length so it is in accordance with the water depth.

The *inner and outer barrel*, a.k.a. *telescope joints* allows the vertical motion of the rig. The inner barrel has the same dimensions as the rest of the riser. It can then stroke on the inside of the outer barrel which is connected to the heave compensating system. The fluid inside is prevented from escaping by pressure seals between the pipes.

Blowout Preventer (BOP)

It is required that the hydrostatic pressure of the mud is greater than the inside pressure to avoid oil and gas into the well. During the drilling operation the drill crown may encounter gas pockets in the ground of extreme pressures. If this pressure reaches a critical pressure it will be higher than the mud pressure it may enter the well at a very high speed. This phenomenon is called a kick. If this kick runs out of control we may have a blowout (Framnes and Gleditsch, 1994).

The BOP shall control the pressure and flow of the fluid and will act in case of emergency. The BOP can interact and prevent a blowout different ways. The BOP can be equipped with a number of different rams to prevent blowouts. A BOP equipped with a variety of rams is then prepared to cut a variety of drilling pipes and strings and one may not need to heave the BOP to the surface to re-equip it every time to save downtime. This makes the BOP larger and heavier. The different BOP ram types are (Wikipedia, 2012):

- *Blind ram* (a.k.a. sealing ram) - Have no openings for the piping. It can close the well when there are no drill strings or other tubing present. It will seal off completely.
- *Pipe ram* - Will close around the pipe to restrict the flow in annulus between the drill pipe and well bore. It does not, however, obstruct the flow inside the drill pipe.
- *Shear ram* - The hardened steel shears will cut the drill string and casing.
- *Blind shear ram* - Will shear the bore even when a drill string is present and seal the well.

Lower Marine Riser Package (LMRP)

The LMRP was developed to make an easy connection between the marine riser and the BOP. It is equipped with remotely controlled valves which makes it easy to connect. The LMRP also has a safety purpose. When the rig motion becomes larger than the

drilling operation is designed for it can disconnect rapidly. It is therefore essential that the lower end of the LMRP has a net positive tension.

Tensioner System

A ring of cylinders are connected between the rig deck and the marine riser's outer barrel. The cylinder is connected to a depressurised accumulator tank keeping the tension fairly constant as the cylinder strokes to compensate for the motion. This allows for the marine riser to maintain a constant heave position without following the rig.

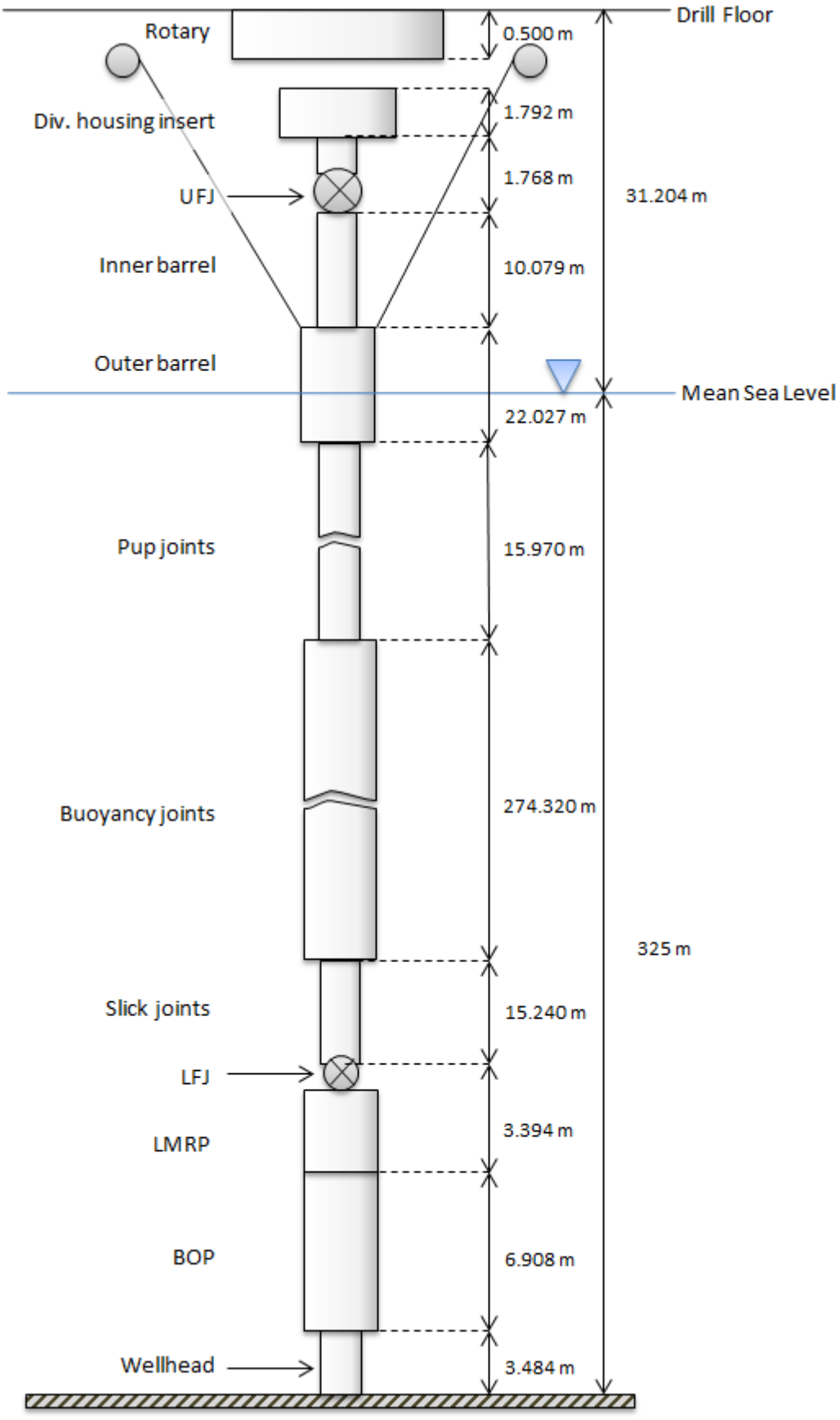

Figure 2.2: Marine riser model structure

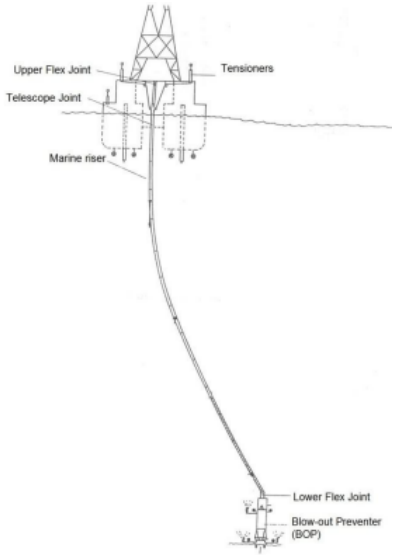

Figure 2.3: Marine riser overview (Framnes and Gleditsch, 1994)

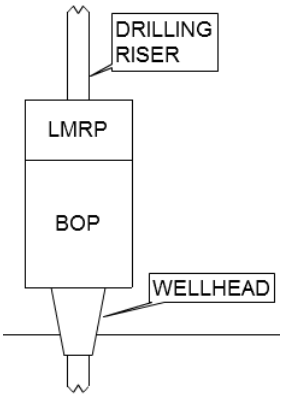

Figure 2.4: Schematic overview of the connection between the well and the marine riser. The wellhead is connected to the Blowout Preventer and is then connected to the marine drilling riser through the lower marine riser package.

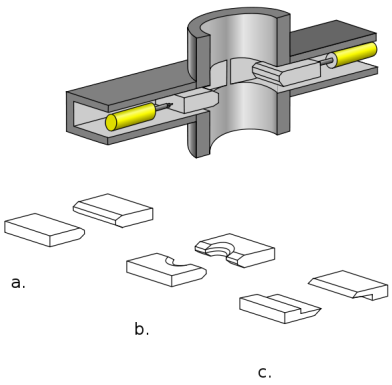

Figure 2.5: Blowout Preventer diagram showing different types of rams. (a) blind ram (b) pipe ram and (c) shear ram. (Wikipedia, 2012)

2.2 Sensor Setup

There are several Motion Reference Units (MRU) installed on the riser system to constantly measure the motions of the rig, riser and BOP. 4Subsea have developed the Riser Expert (REX) system. The system was originally meant as a tool for the operator to monitor the relative motion between the rig and the riser. This allows the operator to have continuous control over the rig's alignment with the wellhead, and control over the angles in positions as the Upper Flex Joint (UFJ) and the Lower Flex Joint (LFJ). Sometimes the operator needs to send objects through the marine riser. The object needs to pass the UFJ and if the relative angle of the riser above and below the UFJ, the object might get stuck or broken.

The following sensors are connected to the rig's REX system (4Subsea, 2012):

1. MRU in the cabinet, measuring the rig motion.
2. MRU below the UFJ.
3. MRU above the LFJ.
4. MRU on the LMRP.
5. MRU above the LFJ.
6. MRU on the LMRP.

The MRUs 1–4 measures all 3 translational accelerations and the rotation rate about 2 axes. The last two sensors only measures the translational accelerations.

The system is shown schematically on figure 2.6. The sensors 1–4 are connected directly to the topside cabinet through cables. The last two sensors are battery powered autonomous and are used as backup sensors. The placement of the sensors below and above the Lower Flex Joint is shown in figure 2.7.

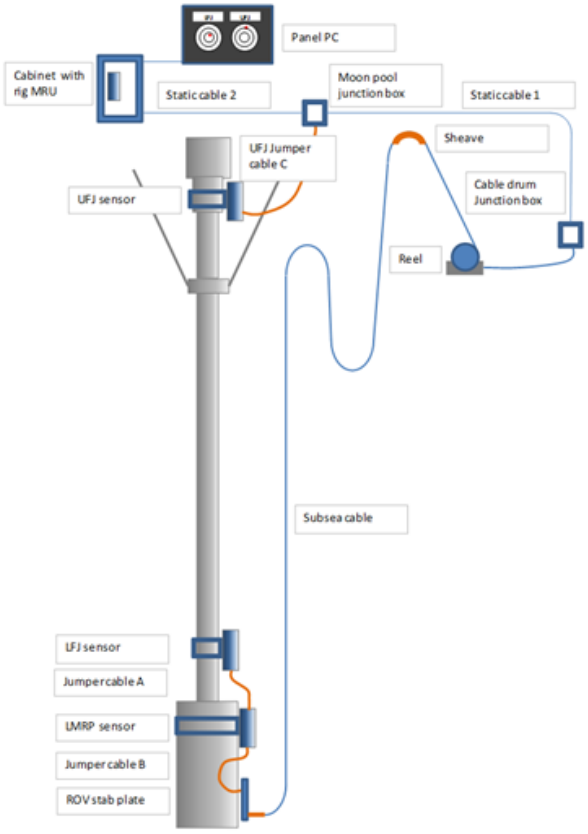

Figure 2.6: REX system for the marine riser (4Subsea, 2012).

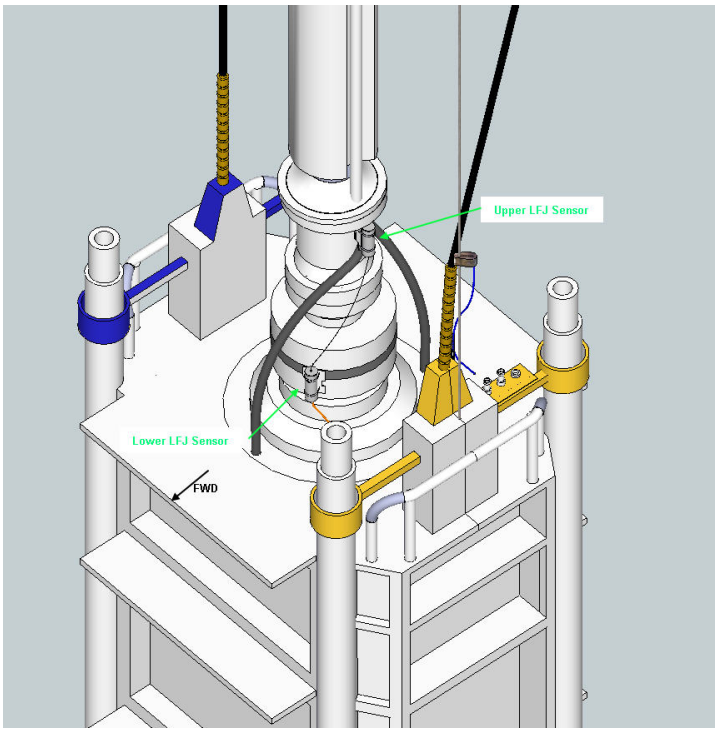

Figure 2.7: Sensor placement above and below the Lower Flex Joint.

2.3 Riflex Model Structure

This section will describe the model structure of the marine riser in RIFLEX as used for the *original* model. The original model contains simplifications of the true marine riser. The modifications of the RIFLEX model will be discussed under simulation models in chapter 6.

2.3.1 Wellhead

The wellhead is the first part. It is modelled as two lines. The sections given are identical, but are of different lengths. The reason for the division is because of a global spring placed at the supernode dividing them. This spring acts only in the horizontal plane and shall represent the stiffness and damping from the seabed. The first node is at $z = -325\,\text{m}$. The lengths of the wellhead lines are 1.860 m and 1.624 m, respectively.

2.3.2 BOP

The BOP is 6.908 m tall and lies above the wellhead. The mass of the BOP is 158.65 Te. Since the top is in tension there will be a point within the BOP which is neutrally tensioned.

2.3.3 Marine Riser

The marine riser itself is naturally divided into separate parts. In the RIFLEX model, the LMRP is a part of the riser. The LMRP are divided into two segments. The two segments are separated by a flex joint element providing stiffness to the Lower Flex Joint (LFJ). This stiffness is lower than the intrinsic stiffness of the LMRP. This will eliminate much of the concentrated moment forces from the marine riser. In the original model the stiffness for this flex joint is $37.9 \times 10^4\,\text{kNm/deg}$. The true stiffness is not linear. The effect of implementing a non-linear spring will be discussed later. The total length of the LMRP is 3.394 m and the mass of the LMRP is 70.9 Te.

The next section is a slick part containing no buoyancy elements. The segment length is 15.240 m. The buoyancy joints are modelled as three different sections. The total length of the three sections is 274.320 m. Then follows another three sections of pup joints with a total length of 13.716 m. The pup joints have the same cross-section as the slick joints below the buoyancy part.

Placed in the mean surface level (MSL) is the outer barrel. The length of the outer barrel is 22.027 m. The length of the inner barrel is 10.079 m. At the top of the inner barrel we have the Upper Flex Joint (UFJ). The UFJ is modelled with a linear rotational stiffness of 5 kN/deg.

On top of the marine riser we have the diverter and rotary with lengths of 1.792 m and 0.500 m, respectively. The rotary is connected to dummy beams that shall model the drill floor's intrinsic stiffness.

2.3.4 Heave Compensator

The outer barrel is connected to the heave compensator lines modelled as elements with a constant tension force regardless of the elongation. In RIFLEX this is modelled using two lines symmetric about the marine riser. Each of the tension legs has a tension force of 5.316×10^5 N

2.3.5 Model Data

The complexity of the complete riser model is too much to include in this text, but in table 2.1 is a summary that will give an overview of the marine riser composition along the length.

Component	Length [m]	Mass$_{air}$ [kg/m]	D_{ext} [m]	D_{int} [m]	EA [GPa]	EI [GNm^2]	GI [GPa]
Wellhead	3.484		0.476	0.476	39.206	1.7083	1.3140
BOP	6.908	23018.3	1.990	0.476	42.375	1.8984	1.4603
LMRP	3.394	10898.5	1.434	0.476	42.375	1.8984	1.4603
Lower flex joint					10.000	3.798×10^{-5}	
Slick joints	15.240	363.3	N/A	0.520	5.2911	0.1773	0.1364
Buoyancy joints	274.320	606.9	0.993	0.520	5.2911	0.1773	0.1364
Pup joints	12.192	363.3	N/A	0.520	5.2911	0.1773	0.1364
Pup joint	3.778	539.2	0.597	0.520	5.2911	0.1773	0.1364
Outer barrel	20.826	761.5	0.690	0.594	544.25	137.70	105.92
Tension ring	1.200	12426.8	1.533	0.578	544.25	137.70	105.92
Inner barrel	10.079	399.5	0.563	0.502	10^{-9}	0.27634	0.2126
Diverter flex joint	1.768	2319.0	0.847	0.584	6.1351	0.2763	0.2126
Upper flex joint					10.000	5.0×10^{-6}	
Rotary	0.500				324.77	50.398	38.767

Table 2.1: Dimension values for the marine riser.

2.4 Acting Forces

The static forces acting on the wellhead are the mass forces from the BOP and LMRP below the flex joint. Above the flex joint the forces from the marine riser are the tension forces, shear forces and a moment.

When the riser has a non-zero angle the tension force T will have a horizontal component T_H. The shear force Q will also have a horizontal component Q_H (See figure 2.8 and 2.9).

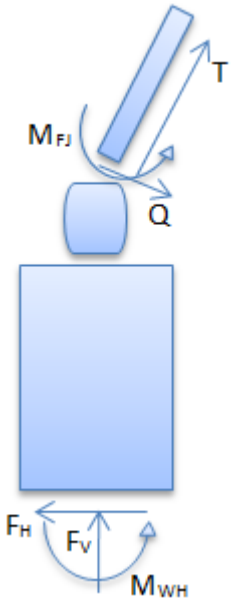

Figure 2.8: A simplified schematic model of the forces acting on the marine riser, BOP and the wellhead.

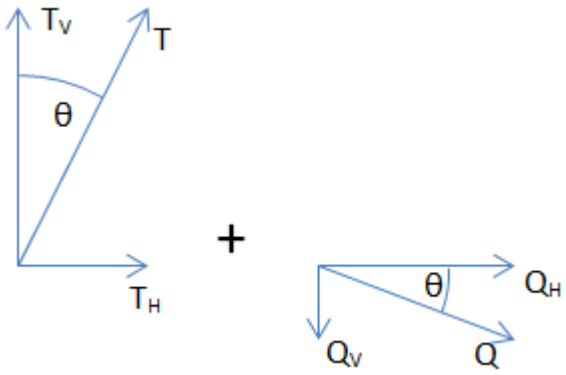

Figure 2.9: The tensile and shear forces at the end of the marine riser can be decomposed into horizontal of vertical forces.

The horizontal components of the tension force and the shear force can be written as

$$T_H = T \sin\theta \tag{2.1}$$

and

$$Q_H = Q \cos\theta \tag{2.2}$$

The total horizontal force at the flex joint from the riser is then

$$F_H = T_H + Q_H \tag{2.3}$$

The flex joint element has a non-linear rotational stiffness. The relative angle between below the lower flex joint and above the lower flex joint will give a concentrated moment here, M_{FJ}. A closer description of the non-linear stiffness is given in section 6.6.2. The stiffness of the spring is changing as the angle changes, i.e. $k_{FJ} = k_{FJ}(\theta)$.

$$M_{FJ} = k_{FJ}(\theta)\theta \tag{2.4}$$

Chapter 3

Stochastic Theory

3.1 Stochastic Process

3.1.1 Definition

A stochastic process or a random process is the opposite of a deterministic process. A random process has built-in uncertainties and is, in principle, described by an infinite number of uncertain variables. Even if the initial values of the process is known, e.g. position, velocity and acceleration the uncertainties of the system motion increases with time. In a probability analysis one can only determine the statistical or averaged characteristics of the process (Newland, 1993). An ergodic process, i.e. a stationary process, will have the same statistical characteristic for *all* samples. This means that the same characteristics may yield two different realisations of the process.

Wave elevation is a typical example of such process. One can measure the elevation at a certain time. Intuitively, we realise that if we want to determine the elevation right after that measurement we can expect it to not change too much. But as this time difference increases, the uncertainty increases. One way to describe this is the autocorrelation function. The autocorrelation function gives the averaged product of the elevation at time t and $t + \tau$. This is expressed by

$$R_X(\tau) = E\left[x(t)x(t+\tau)\right]. \tag{3.1}$$

The autocorrelation function is a function in the time domain. In order to simulate a time series on a computer it is desirable to choose frequencies with different amplitudes and phases that will represent the same characteristics. To transform the autocorrelation function into the frequency domain we need to perform a Fourier transform of the function. This is discussed in closer detail in section 3.4.

3.1.2 Multivariate Normal Distribution

If we assume a narrow band Gaussian process for the angle response it is quite straightforward to calculate the fatigue. The standard deviation and frequency are the only response dependent variables. For a cross-section that is excited to forces from all directions we need to transform the response onto a control plane of which we find the fatigue damage on (see section 5.3.1). Instead of actually transform the response plane for every direction we want to calculate the standard deviation we can use the statistical properties of a bivariate normal distribution.

In a bivariate normal distribution the distance from the mean to the equidensity contour lines at the standard deviation can in general be described as an ellipse, which is proven below. By finding the covariance matrix (equation 3.6) once, we can deduce the standard deviations for all direction using a simple formula.

For a pure multivariate normal distribution of stochastic variables we can describe the process with a expected mean value μ_i and a standard deviation σ_i for each of the variables. In the case of a bi-planar angle we only have two stochastic variables. In general, the bivariate normal probability distribution is defined as

$$f_{XY}(x,y) = \frac{1}{2\pi\sigma_X\sigma_Y\sqrt{(1-\rho_{XY}^2)}} \exp\left[-\frac{1}{2(1-\rho_{XY}^2)}\left(\frac{(x-\mu_X)^2}{\sigma_X^2} + \cdots \right.\right. \\ \left.\left. \frac{(y-\mu_Y)^2}{\sigma_Y^2} - \frac{2\rho_{XY}(x-\mu_X)(y-\mu_Y)}{\sigma_X\sigma_Y}\right)\right], \tag{3.2}$$

where ρ_{XY} is the correlation coefficient defined as

$$\rho_{XY} = \frac{E\left[(x-\mu_X)(y-\mu_Y)\right]}{\sigma_X\sigma_Y}. \tag{3.3}$$

If we set equation 3.2 to a constant C and divide both sides of the equation with the factor before the exponential factor on the left hand side, which also is a constant we get

$$\exp\left[-\frac{1}{2(1-\rho_{XY}^2)}\left(\frac{(x-\mu_X)^2}{\sigma_X^2} + \frac{(y-\mu_Y)^2}{\sigma_Y^2} - \frac{2\rho_{XY}(x-\mu_X)(y-\mu_Y)}{\sigma_X\sigma_Y}\right)\right] = C'. \tag{3.4}$$

We can now take the natural logarithm on both sides and the divide both sides with the factor outside the parentheses. All the right hand side constants are collected in the constant C''. The equation now has the form

$$\frac{(x-\mu_X)^2}{\sigma_X^2} + \frac{(y-\mu_Y)^2}{\sigma_Y^2} - \frac{2\rho_{XY}(x-\mu_X)(y-\mu_Y)}{\sigma_X\sigma_Y} = C'', \tag{3.5}$$

which is a rotated ellipse with its centre located at (μ_X, μ_Y). This means that the equidensity contours of a bivariate normal distribution is shaped as an ellipse regardless of mean values, standard deviations and correlation factors.

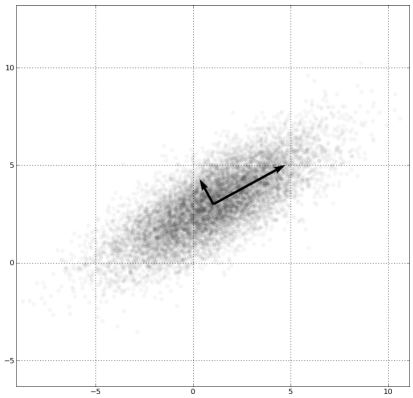

Figure 3.1: Bivariate normal distribution (Wikimedia Commons) Equidensity contour lines would be shaped as ellipses. Principal axes and variances are here marked by the arrows.

The covariance matrix for a data sample is defined as

$$\boldsymbol{\Sigma} = \begin{bmatrix} \mathrm{E}[(X_1 - \mu_1)(X_1 - \mu_1)] & \mathrm{E}[(X_1 - \mu_1)(X_2 - \mu_2)] \\ \\ \mathrm{E}[(X_2 - \mu_2)(X_1 - \mu_1)] & \mathrm{E}[(X_2 - \mu_2)(X_2 - \mu_2)] \end{bmatrix}, \tag{3.6}$$

We can use this matrix to find the principal directions and its corresponding variance for the sampled data in that direction. The eigenvectors yield the directions and the eigenvalues yield the variances. We can then utilize the fact that the equidensity contour lines are ellipses. When this is transformed on a rotated coordinate system the "new" variances will perfectly follow a sine curve which always is positive (see figure 3.2(c)). The mean values will not affect the principal directions nor the variances.

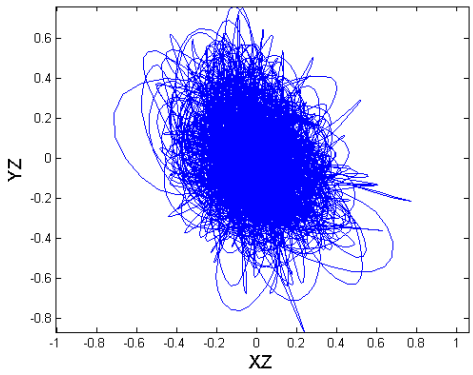

(a) Plot of the angle response

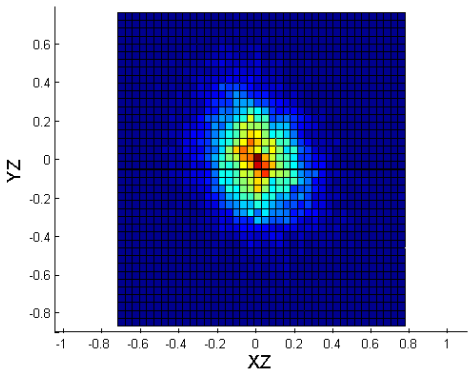

(b) Checkerboard plot of the angle response

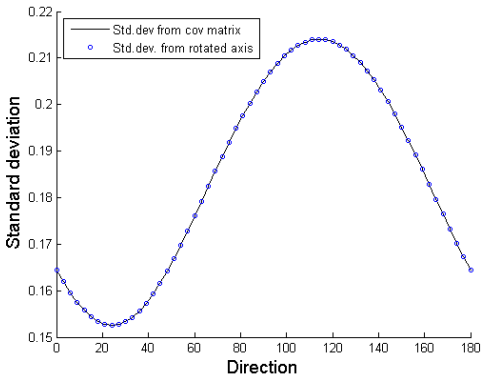

(c) Standard deviation for each direction

Figure 3.2: Example of statistical description of angle response

3.2 Spectral Density

3.2.1 Definition

The spectral density for a Gaussian distributed process is defined as

$$S_x(\omega) = \frac{1}{2\pi} \int_{-\infty}^{\infty} R_x(\tau) e^{-i\omega t} \mathrm{d}\tau \tag{3.7}$$

where $R_x(\tau)$ is the autocorrelation function defined in equation 3.1.

Equation 3.7 describes a Fourier transform of the autocorrelation function. We can also find the autocorrelation function by taking the inverse Fourier transform of the power spectrum

$$R_x(\tau) = \int_{-\infty}^{\infty} S_x(\omega) e^{i\omega t} \mathrm{d}\omega. \tag{3.8}$$

It follows that $\lim_{\tau\to\infty} R_x(\tau) = \mu_x$, where μ_x is the mean value for the Gaussian process. The conditions to perform a Fourier transform is

$$\int_{-\infty}^{\infty} |R_x(\tau)|\,\mathrm{d}\tau < \infty. \tag{3.9}$$

Having the condition in equation 3.9 combined with equation 3.1 we must modify our data in order to properly find the spectral density. All the data must be subtracted with the mean value of the data set.

3.2.2 Spectral Moments

The spectral moments of $S(\omega)$ are defined as

$$m_n = \int_0^{\infty} \omega^n S(\omega)\mathrm{d}\omega, \quad n = 0, 1, 2, \ldots \tag{3.10}$$

We can then find the standard deviation by setting $\tau = 0$ in equation 3.1. We now have that

$$\sigma_X^2 = R_X(0) = \int_{-\infty}^{\infty} S_x(\omega)\mathrm{d}\omega = m_0. \tag{3.11}$$

Hence,

$$\sigma_X = \sqrt{m_0}. \tag{3.12}$$

From the spectral moments we also have that the mean period of the motion is given by (Myrhaug, 2007)

$$T_m = \frac{m_1}{m_0}, \tag{3.13}$$

and the mean zero crossing period is given by

$$T_z = \sqrt{\frac{m_2}{m_0}}. \tag{3.14}$$

The peak period of the motion is

$$T_P = \sqrt{\frac{m_4}{m_2}}. \tag{3.15}$$

3.3 Short-Term Statistics

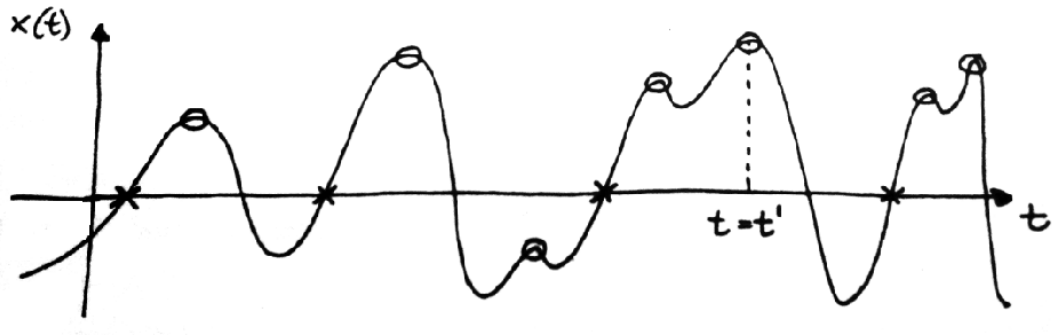

Figure 3.3: Example of a Gaussian process (Myrhaug, 2005). The irregular realisation of the motion is the superposition of an infinite number of regular sine curves with varying amplitudes and random uniformly distributed phase angles.

Figure 3.3 shows an example of a stochastic process. The crosses indicated a positive zero-crossing of the mean position and the circles shows all the local maxima. The distribution of the local maxima can tell us a lot about the process. A generic broad-banded process will have both positive and negative local maxima. An infinitely broad-banded process will in theory have equal amount of negative maxima as positive with a symmetric distribution. In fact, the distribution will become a Gaussian distribution and the process is often referred to as Gaussian *white noise*. The other extreme is a so-called narrow-banded process. The result is a recognisable signal which is very close to a sinusoidal signal. All frequencies with significant energy are then concentrated around one frequency. All maxima are positive for narrow band processes. The distribution of local maxima can be approximated by the Rayleigh distribution.

For a stationary Gaussian process with a finite broadness the general expression for the local maxima can be expressed by the Rice distribution (Myrhaug, 2005)

$$f_\eta^{\text{Rice}}(\eta) = \frac{1}{\sqrt{2\pi}}\epsilon \exp\left(-\frac{1}{2}\left(\frac{\eta}{\epsilon}\right)^2\right) + \sqrt{1-\epsilon^2}\eta \exp\left(-\frac{\eta^2}{2}\right)\phi\left(\frac{\eta}{\epsilon}\sqrt{1-\epsilon^2}\right), \tag{3.16}$$

where $\eta = \zeta/\sigma_X$, ϵ is the bandwidth parameter given by

$$\epsilon^2 = 1 - \frac{m_2^2}{m_0 m_4} \tag{3.17}$$

and ϕ is the cumulative Gaussian distribution. Figure 3.4 shows how the Rice distribution interpolates the Gauss and Rayleigh distributions for different values of the broadness parameter ϵ. The area under each curve is always equal to 1.0.

There is another way to determine the broadness. One can look directly at the ratio between the negative maxima and all maxima. We can then directly count the number

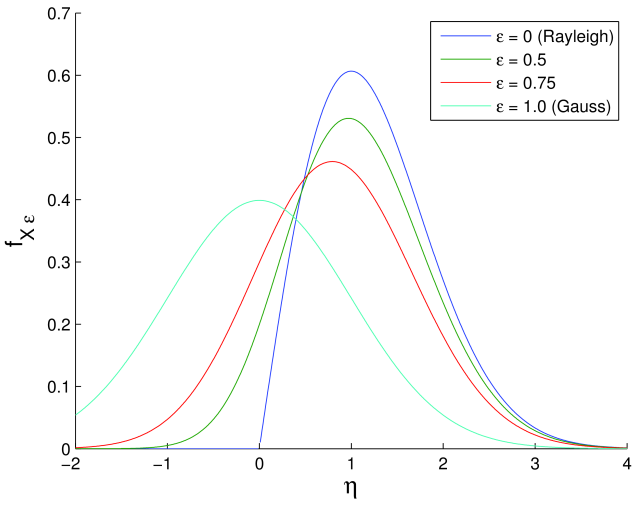

Figure 3.4: Distribution of maxima for different broadnesses

of negative maxima in the data set. From (Cartwright and Longuet-Higgins, 1956) we have:

$$r = \frac{1}{2}\left[1 - \frac{m_2}{\sqrt{m_0 m_4}}\right] = \frac{1}{2}\left[1 - \sqrt{1-\epsilon^2}\right]. \tag{3.18}$$

Conversely, we have

$$\epsilon = 1 - (1-2r)^2. \tag{3.19}$$

The ratio, r, can be understood as the area under the Rice distribution for $-\infty < \eta \leq 0$

$$r = \int_{-\infty}^{0} f_\eta^{\text{Rice}}(\eta)\mathrm{d}\eta. \tag{3.20}$$

3.4 Assumptions

3.4.1 Linear Assumptions

In order to perform a proper stochastic analysis of the sampled data we first need to make some assumptions. To be able to perform any spectral analysis we assume a linear system, i.e. we can describe the motion of the angle as sum of 1$^{\text{st}}$ order forces:

$$I\ddot{\theta} + c\dot{\theta} + k\theta = \sum_{i=1}^{n} y_i. \tag{3.21}$$

All higher order terms such as non-linear drag force, which is proportional to the velocity squared (u^2), are neglected. We also assume that the wave elevation and wave forces are Gaussian processes. Since waves are the main driving forces for both the rig and the marine riser itself, denoted as y_i in equation 3.21, then the probability distribution for the excited motion will also be a Gaussian distribution (Newland, 1993).

When we have a narrow band Gaussian process with a Rayleigh distribution of the local maxima it is quite straightforward to calculate the cumulative damage. The only needed parameters are the mean number of cycles per unit time and the standard deviation of the response (DNV, 2010). The Rayleigh distribution is given as

$$f_X(x) = \left(\frac{x}{\sigma^2}\right) \exp\left(\frac{-x^2}{2\sigma^2}\right), \tag{3.22}$$

where x is local maximum and, σ is the standard deviation of the response.

3.4.2 Non-Linear Assumptions

For a more generic case where we do not have linear forces and reaction forces we cannot use the Rayleigh distribution for local maxima. For a non-linear response the maxima distribution can often be better described with the Weibull distribution given by

$$f_X(x) = \alpha^{-\beta}\beta x^{\beta-1} \exp\left[-\left(\frac{x}{\alpha}\right)^{\beta}\right], \tag{3.23}$$

where α is the scale parameter and β is the shape parameter. The Rayleigh distribution is in fact a special case of the Weibull distribution, i.e. when $\alpha = \sqrt{2}\sigma$ and $\beta = 2$.

Chapter 4

Fatigue Theory

4.1 Cycles to Failure

4.1.1 Constant Amplitude Loading

For various amplitudes the material in question is tested with an oscillating load with constant amplitude. The loading is then set to be between a minimum stress, S_{min}, and a maximum stress, S_{max}. After an average of N cycles the material fails to maintain its structural integrity. When the material is tested for many different stress ranges, i.e. $\Delta S = S_{max} - S_{min}$ we can construct an S-N curve.

4.1.2 Variable Amplitude Loading

A constant amplitude loading may occur in real life, e.g. a machinery part running with a constant load. In a marine environment this is rarely the case. The varying nature of the wind, waves and current will yield a varying amplitude loading on the structure.

The Miner assumption on structural damage is that for every cycle with a stress range ΔS, the structure is damaged as

$$D = \frac{1}{N(\Delta S)}, \tag{4.1}$$

where D is the damage made on the structure. The failure criterion is

$$D_f \geq 1 \tag{4.2}$$

For a stress history, many cycles will fall within the same region of stress range $\Delta S_i \pm \delta S$. For each block number i, we have a number of cycles with the same stress range, n_i. The Miner-Palmgren summation rule can be written as

$$D = \sum_{i=1}^{k} \frac{n_i}{N_i} \tag{4.3}$$

where k is the total number of blocks. The total number of stress cycles, n_0, can be written as

$$n_0 = \sum_{i=1}^{k} n_i \tag{4.4}$$

4.2 θ-N Curve

The term θ-N comes from S-N which is a plot of total number of stress cycles to failure for a constant amplitude scenario. We will use the angle θ directly to compare the cumulative damage.

The relation between the angle and the stress on the wellhead is a complex one. The horizontal component from the tension force is not the only one. There is also a contribution from the flex joint, which is not linear. Also, the damping factor is dependent on the angular velocity. To make things less complicated a "S-N curve" for the angles has been developed so that the angular spectrum can be compared directly for fatigue analyses. The curve should yield an equivalent damage as if the stresses were found. This makes the calculations less cumbersome. Figure 4.1 shows a log-log scaled version of the θ-N-curve. Tabulated values are given in appendix B. This θ-N curve is one of many, but is used throughout in this thesis.

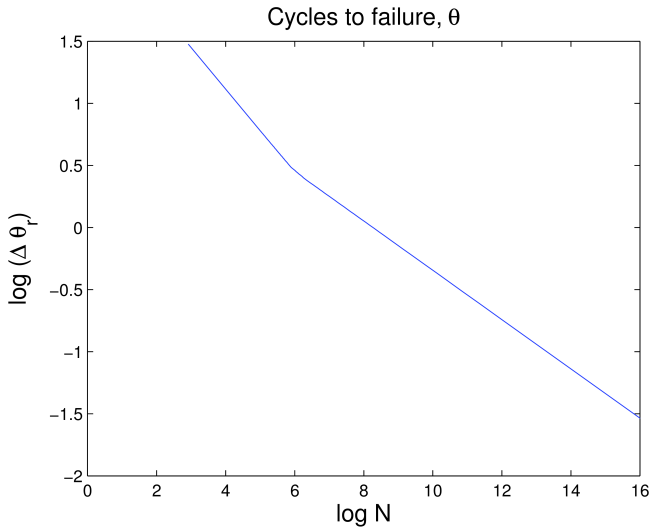

Figure 4.1: Cycles to failure. The curve is bi-linear when it is plotted in a log-log scale.

4.2.1 Determination of Constants in Two-Slope θ-N Curve

A generic θ-N curve which is linear in a log-log scale is given on the form

$$N = \bar{a}(\Delta\theta)^{-m}, \tag{4.5}$$

where N is the number of cycles to failure for a constant stress range, θ, and m is the negative slope of the curve. Equation 4.5 can also be written as

$$\underbrace{\log N}_{x} = \underbrace{\log \bar{a}}_{\hat{a}} - \hat{m}\,\underbrace{\log(\Delta\theta)}_{y}. \tag{4.6}$$

We can then find the values for $\hat{a}$ and $\hat{m}$ by selecting two points for each section in the θ-N curve by solving the equations

$$\begin{bmatrix} x_1 \\ x_2 \end{bmatrix} = \begin{bmatrix} 1 & -y_1 \\ 1 & -y_2 \end{bmatrix} \begin{bmatrix} \hat{a} \\ \hat{m} \end{bmatrix}. \tag{4.7}$$

The constants for the first (steepest) slope are

$$\begin{bmatrix} \hat{a}_1 \\ \hat{m}_1 \end{bmatrix} = \begin{bmatrix} 1 & -1.47712 \\ 1 & -0.63827 \end{bmatrix}^{-1} \begin{bmatrix} 2.91459 \\ 5.42603 \end{bmatrix} = \begin{bmatrix} 7.3369 \\ 2.9939 \end{bmatrix}$$

And for the other slope the values are

$$\begin{bmatrix} \hat{a}_2 \\ \hat{m}_2 \end{bmatrix} = \begin{bmatrix} 1 & -0.39979 \\ 1 & 0.17160 \end{bmatrix}^{-1} \begin{bmatrix} 6.25648 \\ 9.12706 \end{bmatrix} = \begin{bmatrix} 8.2650 \\ 5.0238 \end{bmatrix}$$

To use this in a closed form solution for the damage we need to identify the knee of the of the θ-N curve. We now have expressions on the form $x = \hat{a} - \hat{m}y$. And we want to find the value of y where x is the same. The two equations are

$$x = 7.3369 - 2.9939y \tag{4.8a}$$

$$x = 8.2650 - 5.0238y \tag{4.8b}$$

By subtracting equation 4.8a with 4.8b, we get

$$y = 0.4572$$

I.e. $\Delta\theta_r = 2.865$.

4.2.2 Closed Form Fatigue Life Equations

For a narrow band Gaussian stress response (or angle response in our case) there is a very simple relation between the mean frequency, standard deviation and the cumulative damage. For a simplified case where we have a linear θ-N curve the damage per unit time can be written as

$$D = \frac{f_0}{\bar{a}} \left(2\sqrt{2}\sigma\right)^m \Gamma\left(\frac{m}{2}+1\right) \tag{4.9}$$

where f_0 is the mean frequency, m is the inverse slope of the θ-N curve and $\Gamma(\phi)$ is defined as

$$\Gamma(\phi) = \int_0^\infty \mathrm{e}^{-t} t^{\phi-1} \mathrm{d}t \tag{4.10}$$

For a non Gaussian process the distribution of ranges cannot be described with the Rayleigh distribution, but with the more generic Weibull distribution. The closed form solution for a Weibull distributed range density can be written as (Almar-Næss et al., 1985):

$$D = \frac{n_0}{\bar{a}} \frac{\Delta\sigma_0^m}{(\ln n_0)^{m/h}} \Gamma\left(1+\frac{m}{h}\right), \tag{4.11}$$

The expression is valid for a θ-N curve which follows equation 4.6, i.e. a single linear relation. Most offshore steel material does not follow this curve. A more realistic θ-N curve is a bilinear curve as in figure 4.1. Each line has its own slope and intersection point on the $\log n$ axis. A closed form solution is also found in this situation (DNV, 2010)

$$D = \frac{f_0(2\alpha)^{m_1}}{\bar{a}_1} G_1\left\{\left(1+\frac{m_1}{\beta}\right);\left(\frac{S_{sw}}{2\alpha}\right)^\beta\right\} + \frac{f_0(2\alpha)^{m_2}}{\bar{a}_2} G_2\left\{\left(1+\frac{m_2}{\beta}\right);\left(\frac{S_{sw}}{2\alpha}\right)^\beta\right\}, \tag{4.12}$$

where G_1 and G_2 are the complementary incomplete Gamma function and incomplete Gamma function

$$G_1(\phi, x) = \int_0^x \mathrm{e}^{-t} t^{\phi-1} \mathrm{d}t \tag{4.13a}$$

$$G_2(\phi, x) = \int_x^\infty \mathrm{e}^{-t} t^{\phi-1} \mathrm{d}t \tag{4.13b}$$

The expression implies a two-parameter Weibull distribution of the probability density function of the angle ranges, where β is the shape factor, α is the scaling factor, S_{sw} is

the stress (or angle in our case) describing the knee in the θ-N curve and f_0 is the average number of cycles per time unit. The sum of the two incomplete Gamma functions is the full Gamma function, i.e. we can use that they are just weighing factors for the two slopes. We can then write it on the following form:

$$\begin{aligned} D = &\frac{n_0}{\bar{a}_1}\frac{\Delta\sigma_0^{m_1}}{(\ln n_0)^{m_1/h}}G_1\left\{\left(1+\frac{m_1}{\beta}\right);\left(\frac{S_{sw}}{2\alpha}\right)^{\beta}\right\} \\ &+\frac{n_0}{\bar{a}_2}\frac{\Delta\sigma_0^{m_2}}{(\ln n_0)^{m_2/h}}G_2\left\{\left(1+\frac{m_2}{\beta}\right);\left(\frac{S_{sw}}{2\alpha}\right)^{\beta}\right\}. \end{aligned} \tag{4.14}$$

4.2.3 Wide Banded Stress History

The closed form fatigue life equations are based on a narrow band process. Based on Gaussian narrow band damage, D_{NB} compared with rainflow counting damage, D_{RFC}, which is regarded as the *true* cycle counting approach (DNV, 2010) a correction factor, κ_{RFC}, has been proposed. The corrected damage is expressed as

$$D_{RFC} = D_{NB}\kappa_{RFC}, \tag{4.15}$$

where κ_{RFC} is expressed as

$$\kappa_{RFC}(m) = a + (1-a)(1-\epsilon)^b, \tag{4.16}$$

where

$$a = 0.926 - 0.033m \tag{4.17a}$$

$$b = 1.587m - 2.323 \tag{4.17b}$$

For a completely narrow banded process ($\epsilon = 0$) the correction factor is 1, and for a broadness larger than zero the correction factor will become lower than 1. Figure 4.2 shows the effect of the correction factor for two different S-N curve slopes.

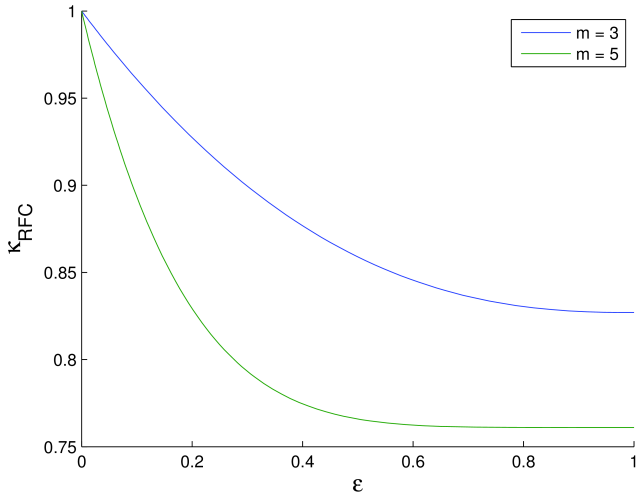

Figure 4.2: Correction factor for broad banded fatigue assessment

4.3 Cycle Counting and Fatigue

The distribution of maxima is a good way to determine the broadness of a spectrum. To use the time series in a fatigue analysis we need the stress ranges. A discrete distribution of the stress cycles, i.e. for stress cycles falling within the region $[S_i, S_i + \Delta S]$, will give us the information needed to perform a fatigue analysis.

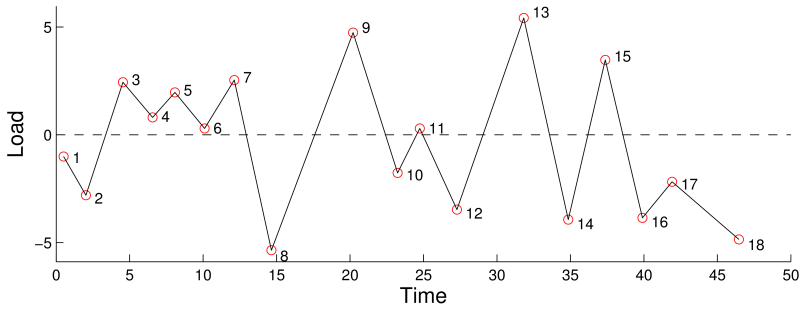

Figure 4.3: Example load history

A description of the terminology as given by (Almar-Næss et al., 1985):

- *Reversal* is the occurrence where the first derivative of the load-time history changes sign.
- *Peak* is the occurrence where the first derivative of the load-time history changes from positive to negative sign.
- *Valley* is the occurrence where the first derivative of the load-time history changes from negative to positive sign.
- *Range* is the algebraic difference between successive valley and peak loads (negative range, e.g. points 3 to 4, 7 to 8, ...) or between successive peak and valley

loads (positive range, e.g. points 2 to 3, 6 to 7, ...).

Counting cycles for a narrow band process is trivial, i.e. all counting methods yield almost the same answer. However, for a broad banded process, the result will depend strongly on the method. A common method of choice for a broad banded process is the *rainflow counting* method, or RFC.

4.3.1 Weibull Stress Range Distribution

Representing an irregular load history for fatigue analysis is most commonly done in an exceedance diagram of stress ranges, often called the stress range spectrum. In most practical cases the stress range spectrum can be approximated by a two-parameter Weibull distribution, which can be written on the following form (Almar-Næss et al., 1985):

$$\theta_r = \theta_{r,0}\left[1 - \frac{\log_{10} n}{\log_{10} n_0}\right]^{\frac{1}{\beta}}, \tag{4.18}$$

where $S_{r,0}$ is the stress range which is exceeded once out of n_0 cycles, n is the number of stress cycles equal to or exceeding S_r and β is the shape parameter as shown in figure 4.4.

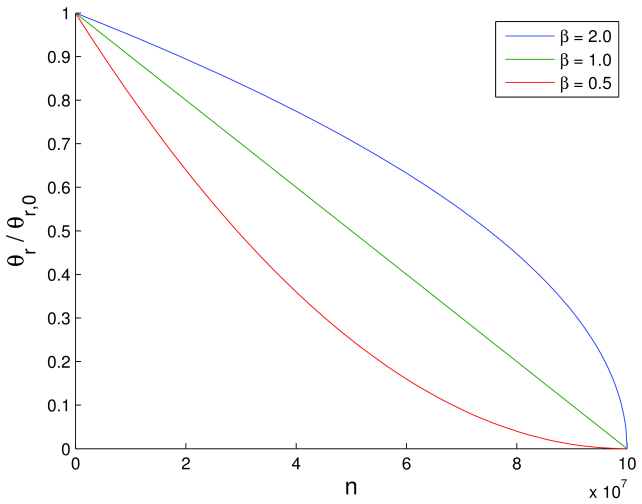

Figure 4.4: Normalised stress spectrum represented by the Weibull distribution with different shape parameters.

4.3.2 Rainflow Counting

The rainflow counting method was originally proposed as a cycle counting method by T. Endo and M. Matsuishi in 1968. A revised method was developed in 1974 (Anzai and

Endo, 1979). A complex time signal can have several reversals between zero-crossings and different counting methods yields very different results. The rainflow counting procedure counts cycles and half-cycles of stress-time signals which, in general, are random finite-banded signals. This makes it difficult to determine the number of cycles absorbed by the structure (Ariduru, 2004). The counting of ranges can be represented in a histogram that displays the distribution of the random ranges. The distribution of stress ranges makes it possible to make the stress spectrum.

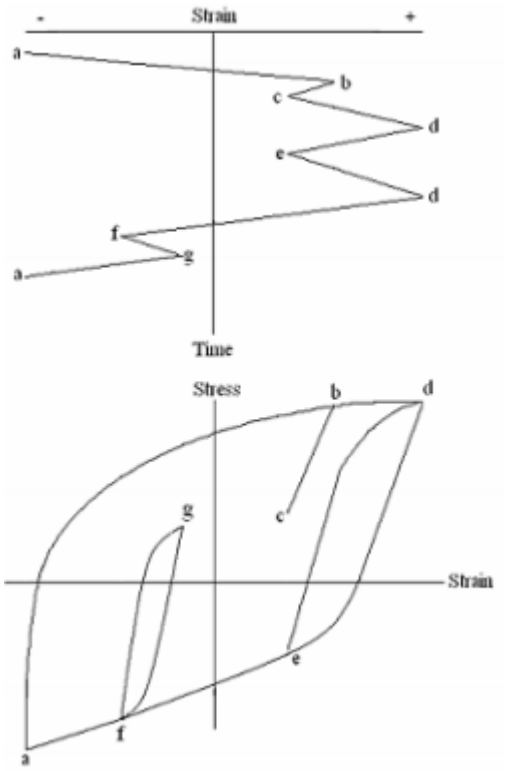

Figure 4.5: Stress-strain cycles. The signal is plotted vertically with time. The variation in strain amplitude makes the rainflow counting method suitable for broad banded processes.

The name *rainflow counting* originates from the analogy of the raindrops dripping from a Japanese *Pagoda Roof*. The time axis of the signal is then rotated vertically. A water drop is created on a peak or valley and is released on the next reversal as shown in figure 4.6.

The rainflow follow the rules as:

1. Raindrops will form on the inside of each peak or valley.
2. The raindrop will drip of the roof when it reaches the successive reversal.
3. When the drop meets a flow from above, the drop stops and a cycle is completed.
4. The drop will also stop is it meets a peak larger than the starting peak, or a valley more negative than the starting valley.

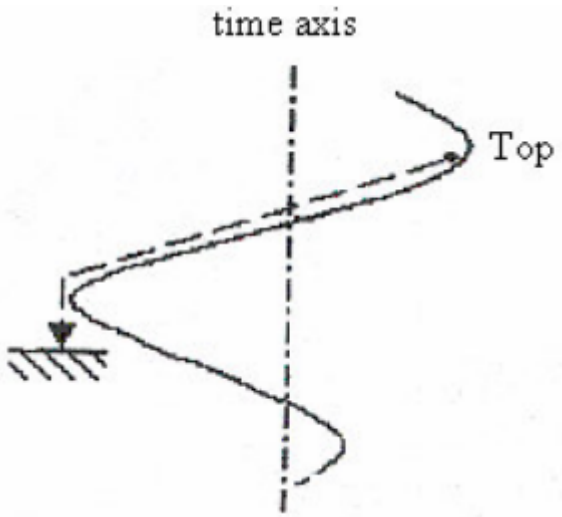

Figure 4.6: Creation and release of raindrop.

5. A flow that is part of stopping another flow to form a full cycle is itself only forming a half-cycle.

Figure 4.7 shows an example where only drops from valleys are shown. It illustrates the rules as explained above. For a sufficiently long record the valley-generated half-cycles will match a peak-generated half-cycle to form a whole cycle (Ariduru, 2004).

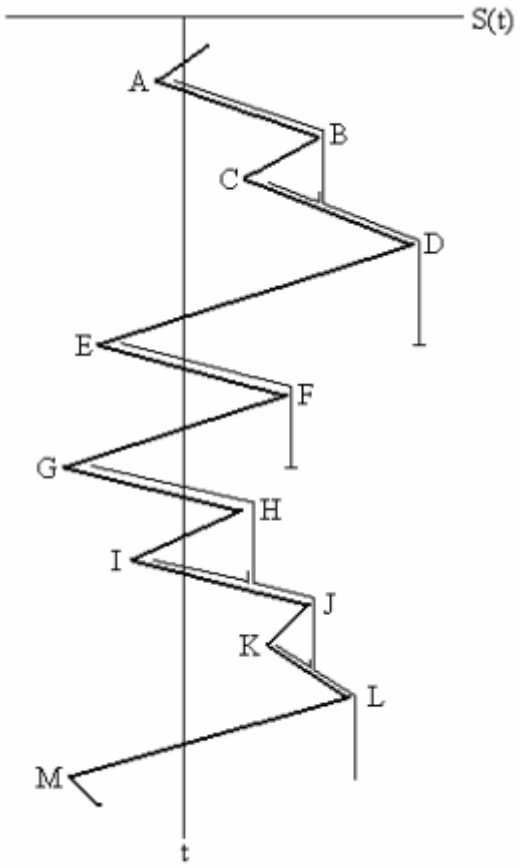

Figure 4.7: An example of rainflow for one side only. A raindrop is created inside each valley and is released on the succeeding peak.

Chapter 5

Full Scale Data Analyses

5.1 Environmental Parameters

In order to simulate the weather conditions as representative as possible we need detailed and reliable data from the offshore field or at least very near it. The weather data collected that will be used here is from NORA10 (NOrwegian ReAnalysis). The grid point is placed 37 km north and 27 km east for this site, a total distance of 46 km. We're going to assume that this is close and representative enough for the entire area, including the position in question.

The given weather data is very detailed and gives values for the total sea state, wind sea and swell. The weather data also provides wind speed and direction at different levels above mean sea level. For the wind sea and swells we can find the significant wave height, H_S, the peak period, T_P, and its mean direction.

Two methods in simulating the sea state in RIFLEX may be relevant. The total sea may be best represented with a Torsethaugen spectrum. The Torsethaugen spectrum is a double peaked spectrum and its only parameters are H_S and T_P from the *total sea* data. The spectrum is developed based on data from Haltenbanken and Statfjord (Torsethaugen and Haver, 2004). With this option we cannot control the direction spreading for wind sea and swells separately. We can, however, use a generic cosine distribution (Marintek, 2010). The Torsethaugen spectrum is based on the JONSWAP spectrum. Since we can input more than one irregular sea state data simultaneously we can use the two datasets for wind sea and swells. We can then control the direction in some more detail. It is even possible to describe directional spreading on each one of them.

The long term sea states observations is presented table 5.1. It shows the relation of the total sea state and does not distinguish between wind and swell sea.

Hs/Tp	1	2	3	4	5	6	7	8	9	10	11	12	13	14	15	16	17	18	19	20	21	Observations
1	0	0	1	1	20	58	18	9	18	9	1	2	0	0	0	0	0	0	0	0	0	137
2	0	0	1	19	46	103	112	131	124	95	76	57	17	5	0	4	0	1	0	0	1	792
3	0	0	0	0	7	59	49	76	97	133	113	79	41	30	0	7	0	1	0	0	1	693
4	0	0	0	0	0	4	19	55	79	96	117	93	50	31	0	22	0	12	3	0	5	586
5	0	0	0	0	0	0	5	17	30	56	62	66	38	36	0	12	0	7	3	0	0	332
6	0	0	0	0	0	0	1	3	7	20	65	60	21	10	0	6	0	1	1	0	0	195
7	0	0	0	0	0	0	0	0	0	1	28	27	23	3	0	7	0	6	1	0	0	96
8	0	0	0	0	0	0	0	0	0	0	2	14	24	1	0	3	0	2	0	0	0	46
9	0	0	0	0	0	0	0	0	0	0	0	3	10	7	0	0	0	0	1	0	0	21
10	0	0	0	0	0	0	0	0	0	0	0	1	3	3	0	0	0	0	0	0	0	7
11	0	0	0	0	0	0	0	0	0	0	0	0	2	0	0	1	0	1	0	0	0	4
12	0	0	0	0	0	0	0	0	0	0	0	0	0	0	0	1	0	1	0	0	0	2
13	0	0	0	0	0	0	0	0	0	0	0	0	0	1	0	2	0	0	0	0	0	3
14	0	0	0	0	0	0	0	0	0	0	0	0	0	0	0	1	0	2	0	0	0	3
15	0	0	0	0	0	0	0	0	0	0	0	0	0	0	0	0	0	0	0	0	0	0
16	0	0	0	0	0	0	0	0	0	0	0	0	0	0	0	0	0	2	0	0	0	2
Observations	0	0	2	20	73	224	204	291	355	410	464	402	229	127	0	66	0	36	9	0	7	2919

Table 5.1: Long term sea states observations

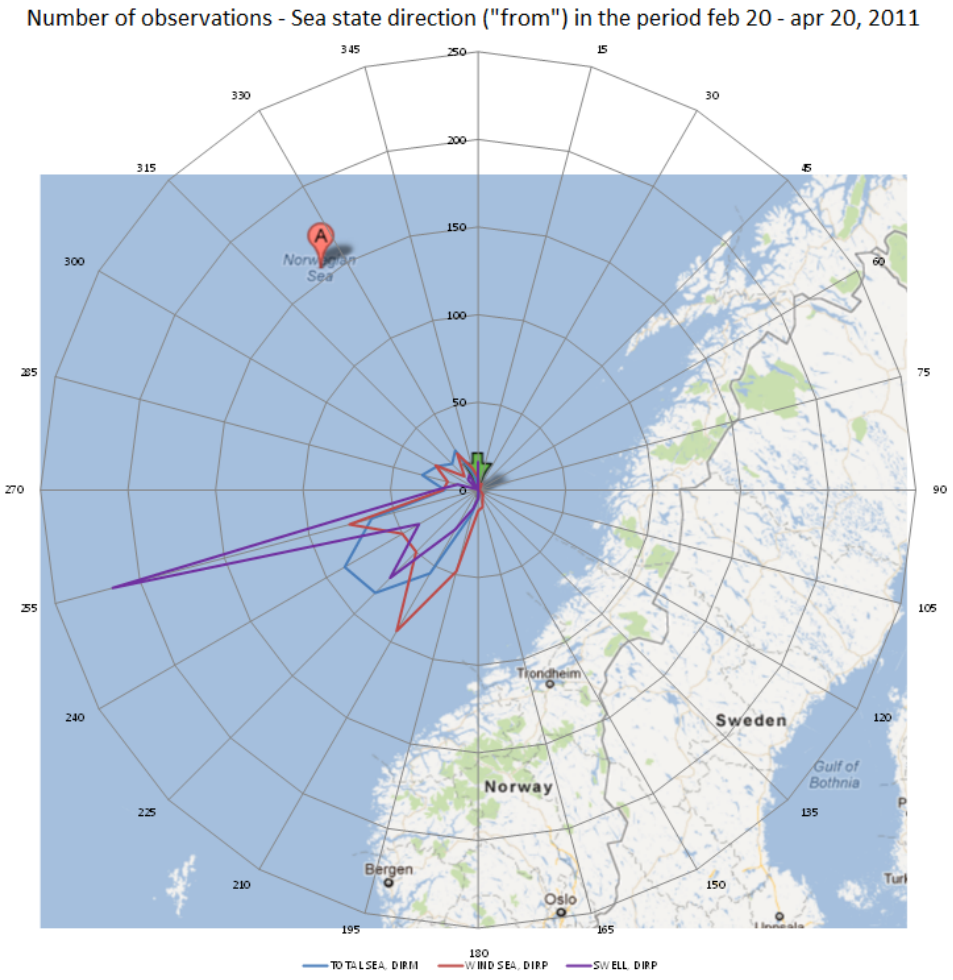

Figure 5.1: Sea state directions at Haltenbanken

5.2 Sampled Data

5.2.1 Data Files

The angle time series are stored in text files. The sampled data are contained in many separate files. Every file contain about 60 min of data with a sampling rate of about 5 Hz. The files are organised into 4 columns, the first one being the time since sampling start. Column two and three are angles in the xz- and yz-planes, respectively. The fourth column is a dummy column.

The calculated angles are based on numerical integration over time of the angular rate time series. Numerical integration will in general introduce numerical errors. Such errors can be drifting and/or false slowly varying effects. The data has been compared in a period where the data from the two different MRU types installed (same location) show consistent data. Unphysical effects has been filtered out from the data and time series with a high probability of error or faulty time series has been removed from the complete data set (Holden, 2012) and (Pytte, 2012). One can never be certain that all non-existing effects has been removed or filtered from the data set, but for all purposes of this thesis we will proceed assuming that the datas represent the correct angle motion of the marine riser.

5.2.2 Techniques

The data can be analysed in various ways. The best way to find any correlations with calculated values is using statistical analyses. One can quickly find similarities from the variance and the covariance.

The program used to perform the actual transformation to find the spectral density is WAFO. With the WAFO toolbox for Matlab it is possible to generate smoothed spectral densities that will remove any noise in the graphical output (WAFO-group, 2000).

For each set of data the data ensemble will be connected to the relevant measured sea state at that time. The relevant connecting parameters are H_S and T_P for the total sea. When the data are collected into groups we can develop a statistical picture of the expected response for the different sea states.

5.2.3 Normal Distribution Probability Paper

In order to verify the assumption of a Gaussian probability distribution of the angles in the xz- and yz-plane we can construct a probability paper for a normal distribution. The cumulative distribution function for a normal distribution is

$$F_X(x) = \frac{1}{2}\left[1 + \operatorname{erf}\left(\frac{x}{\sigma\sqrt{2}}\right)\right]. \tag{5.1}$$

We can manipulate and rewrite this equation into

$$x = \underbrace{\sigma\sqrt{2}}_{a}\underbrace{\text{erf}^{-1}(2F_X(x) - 1)}_{y}, \tag{5.2}$$

where erf^{-1} is the inverse error function. By using the equation for empirical cumulative value F

$$\hat{F} = \frac{\text{data entry number}}{\#\text{ total data entries} + 1} \tag{5.3}$$

we can create a linear set of data point which we can plot according to $x = ay$. The more linear the data point line up, the more perfect normal distributed they are. By using regression analysis we can find the slope, a. From the slope we can also find the standard deviation σ using

$$\sigma = a/\sqrt{2}. \tag{5.4}$$

Figure 5.2 shows an example of how close to a normal distribution the angle distribution is.

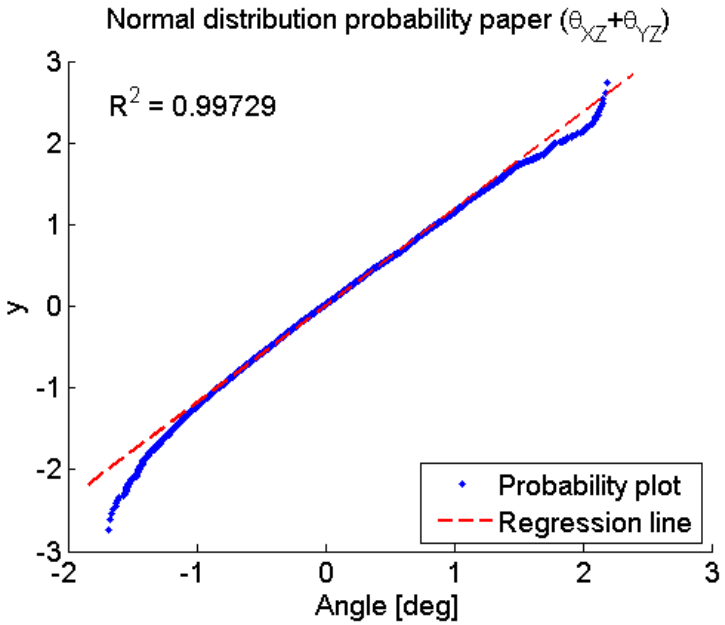

Figure 5.2: Normal distribution probability paper example. For a perfectly normal distribution the data would form a straight line. The coefficient of determination yield the "goodness of fit" of the line.

There may exist probability distribution function $f_{XY}(x, y)$ which are not bivariate normal distributed, but constructed in such a way that the marginal densities are normal. This can also be true for the case where we have a linear combination of the two

variables, e.g. $X + Y$. From (Hamedani and Tata, 1975) we can use that when the linear combination of the variables and the marginal density are normal distributed, the vectors $[X_k, Y_k]$ are bivariate normal distributed.

The coefficient of determination R^2 for the sample hour in figure 5.2 is found to be 0.99729. The closer the value is 1.0, the better, and this seems to be a very good fit.

5.3 Multi-Directional Fatigue

5.3.1 Control Planes

The wellhead is subjected to bending in all directions in the horizontal plane. The riser angle is described only by the angle in the xz- and yz-planes. To assess the loading in each direction we need to take a projected snapshot of all possible planes. To do this for an infinite number of planes require both time and a massive amount of data. We will restrict us to a limited amount of planes around the z-axis. A sub-division of 8 planes should be sufficient. This gives a 22.5° spanning between each plane. Assuming that fatigue damage for any angle ϕ and $\phi + \pi$ accumulates the same damage since their cycle count will be the same but from the opposite signal, only directions between 0° and 180° will be considered. Hence, two sea states of opposite directions will yield fatigue in the same plane.

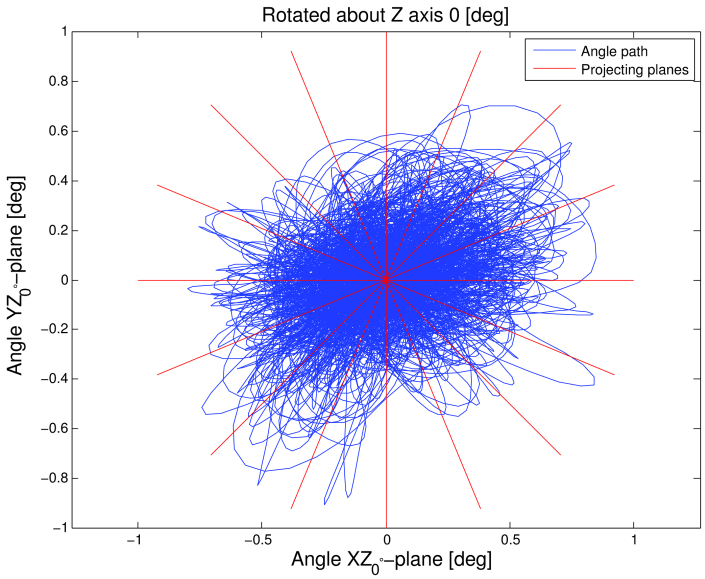

Figure 5.3: Example of angle path and projecting planes

Figure 5.3 illustrates how the planes which will be considered are distributed. Since bending about the in-plane axis will not contribute to any fatigue *on* that plane we can project them to the same plane, neglecting the out-of-plane motion for that particular angled plane. We can then find the distribution of angles about the plane's normal axis. To evaluate the projected plane we need to rotate the signal onto a transformed xy_ϕ

system, where ϕ indicates the rotation angle of the transformed coordinate system in degrees. If any angle vector containing a pair of xz- and yz-angles respectively is

$$\boldsymbol{\theta} = [\theta_{xz}, \theta_{yz}], \tag{5.5}$$

which is a horizontal vector. Then the corresponding transformed vector is

$$\boldsymbol{\theta_\phi} = \boldsymbol{\theta} \begin{bmatrix} \cos\phi & -\sin\phi \\ \sin\phi & \cos\phi \end{bmatrix} \tag{5.6}$$

We are only interested in the spectrum to the transformed xz_ϕ-plane, since the yz_ϕ will always be covered when all planes are evaluated.

Since the out-of-plane motion for all planes are taken away, we need to account all the motion for all planes for all times and not only the largest one. This way we can for each sea state disconnect the main direction of motion and fatigue for each plane. From this we can later construct the distribution of angles with respect to fatigue and not only the distribution of weather and waves themselves.

The in-plane motion is Gaussian distributed with zero mean value, i.e. after correction since this is a static value under the stationary assumption. Standard deviation and the power spectrum are the values of interest here.

5.3.2 Governing Response Angle

The response is elliptic with a certain governing angle in all data series. This angle does not seem to follow the direction of the incoming waves. The relative direction between the angle response and the weather's direction seems random (see figure 5.4). This angle is not restricted since it varies from $-90°$ to $90°$. This gives an important piece of information that we can use. I.e. the response has no preferred angle with respect to weather conditions. Since the weather does have a preferred direction this causes the wellhead to be exposed to less fatigue on each control plane. All the calculated standard deviations and its effect on the fatigue can be distributed for all angles, which gives the most non-conservative fatigue calculations. The opposite is when we assume that all response happens in the same line of direction.

Three cases can now be identified. When the ratio, as described below, is 0 (conservative), 1 (non-conservative) or between 0 and 1, which is the most realistic case. For any given sea state we have an expected maximum and an expected minimum standard deviation. The unknown is the governing direction. We have shown that the ellipse-shaped variance along the angles yields a sine curve on the form

$$\mathrm{Var}[\theta] = A + B\cos[2(\theta - \phi)], \tag{5.7}$$

where A must be larger than or equal to B in order to always have a positive variance and ϕ is the time series' preferred angle. The standard deviation will then become

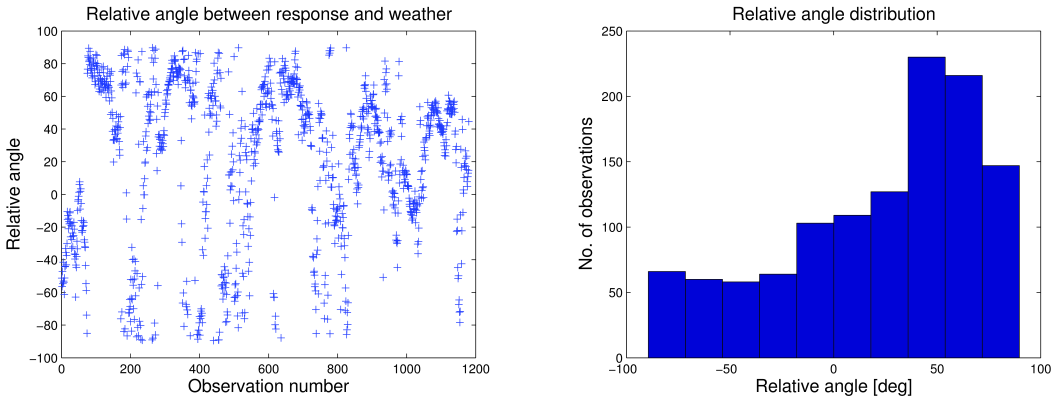

(a) Relative angle between weather and response

(b) Relative angle distribution

Figure 5.4: Spread and distribution of the relative angle between the weather and riser response

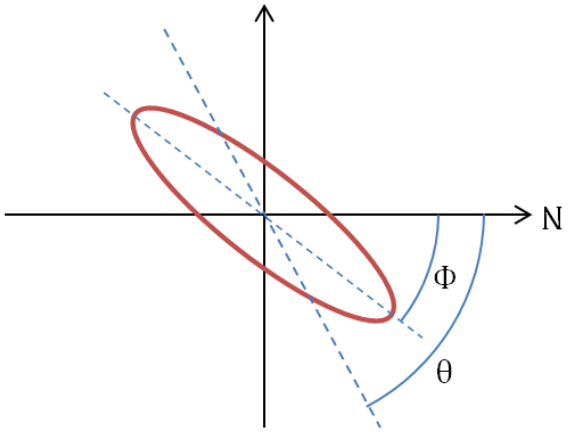

Figure 5.5: Illustration of response angle relations seen from above

$$\sigma(\theta, \phi) = \sqrt{A + B\cos[2(\theta - \phi)]}. \tag{5.8}$$

Where the ratio, denoted ζ will be

$$\zeta = \frac{\sqrt{A-B}}{\sqrt{A+B}} = \sqrt{\frac{A-B}{A+B}} = \frac{\sigma_{min}}{\sigma_{max}}. \tag{5.9}$$

Instead of the 8 control planes described in section 5.3.1 we can now, in theory, divide the planes infinitely. We can do so by combining equation 5.8 and 5.9 and some modification find

$$\sigma(\theta, \phi) = \frac{\sigma_{max}}{\sqrt{2}}\sqrt{1 + \zeta^2 + (1 - \zeta^2)\cos[2(\theta - \phi)]}. \tag{5.10}$$

The users can now select how fine they want to find the accumulated damage for each direction by this simple formula.

5.4 Results

5.4.1 Selecting Representative Data

From figure 5.1 we can see that some sea states occur more often than others. Although data is collected and calculated for most of them only a few of them will be presented. The selected sea states will be the basis for comparison and limit the necessary simulations in RIFLEX.

It is preferable to select multiple sea states that share either H_S or T_P that still have some observations in it. But this is still no guarantee that the data is any "good". We may still have observations that are incorrectly categorised. Another problem is that some results yield unphysical results even though "bad data" have been filtered out after best effort. We expect, for example, that higher H_S for the same T_P should yield a larger response. If we can follow a trend that seems reasonable, but there are observations that diverge from this trend, then we cannot use this data uncritically. An example of this can be found in figure 5.6. Here we can see that we see an increasing trend which is expected, but at the largest H_S it diverges from the expected behaviour. Therefore, all sea states have been selected using engineering judgement where the data are as consistent as possible.

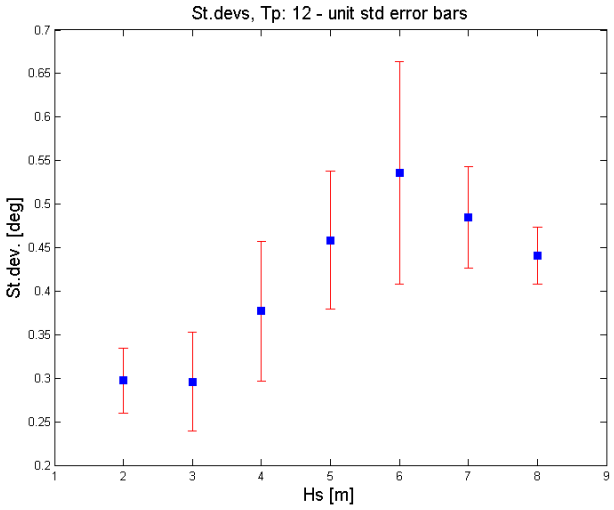

Figure 5.6: Standard deviations for $T_P = 12\,\text{m}$. The blue square indicated the mean of all sampled standard deviations and the error bars indicates the natural variances between all the standard deviation from the same sea state.

In figure 5.7 the directional scattering is shown for the different sea states. Due to symmetry the waves with a heading of $\pm 30°$ should yield the same response for the

Hs\Tp	5	6	7	8	9	10	11	12	13	14	15	16	Total hours
1													0
2		6		21	32	42	9	27		15	6	3	161
3		3	3	39	83	33	57	45		21		3	287
4			3	6	36	42	42	72		74	18	3	296
5				6	3	17	27	84		23	21	15	196
6						6	62	63		15	9		155
7							5	12		29	3		49
8								6		21	3		30
9											6		6
10													0
11													0
12													0
13													0
14													0
Total hours	0	9	6	72	154	140	202	309	0	198	66	24	1180

Table 5.2: Sea states with measured data in period

H_S	2	2	4	2	4	6
T_P	9	10	10	12	12	12

Table 5.3: Selected sea states

rig and marine riser system. The right plot shows the distribution when the symmetry is accounted for. This will help reduce the number of simulations. We will use this distribution to get as close weighing when calculating the long term distribution for the angle spectra later.

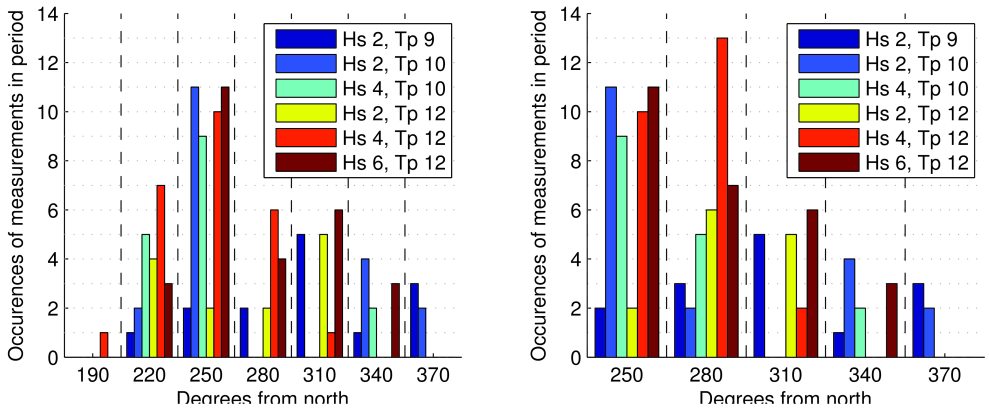

Figure 5.7: Occurences of directions for different sea states within measured period

5.4.2 Standard Deviation and Ratio

Each time series has been compressed to the two variables standard deviation and its ratio between the maximum and minimum standard deviation. Each time series' standard deviation is then plotted. Then the means of the standard deviations are found with its corresponding standard deviation. For the selected sea states the values are listed in table 5.4 and shown in the figures below.

The standard deviation do not change whether the time series data are low frequency dominated or wave-frequency dominated. The mean of the standard deviation is close to the same and so is the spread of them. The ratios are also unaffected by this. If we were to divide the calculated standard deviation into both low/wave frequency categories and mean wave heading direction we would be left with very few data points for each state. All standard deviation are collected into the same category, i.e. for the same H_S and T_P.

H_S	T_P	Obs.	σ_{mean}	σ_{std}	ζ_{mean}	ζ_{std}
2	9	32	0.350	0.081	0.550	0.073
2	10	42	0.308	0.043	0.611	0.112
4	10	42	0.510	0.095	0.619	0.109
2	12	27	0.297	0.037	0.518	0.241
4	12	72	0.377	0.080	0.774	0.134
6	12	63	0.536	0.128	0.770	0.137

Table 5.4: Standard deviations and ratios for the selected sea states.

In the table, σ denotes the standard variation of the measured time series. There are measured many standard deviations for each sea state and the mean and standard deviation of those measurements is meant to just illustrate the scattering of the calculated motion. In the figures below, σ_{mean} is marked with a solid line, and σ_{std}, both above and below the mean are marked with dashed lines. Each data point reflects the standard deviation of one hour. The same goes for the calculated ratio, ζ, for all time series.

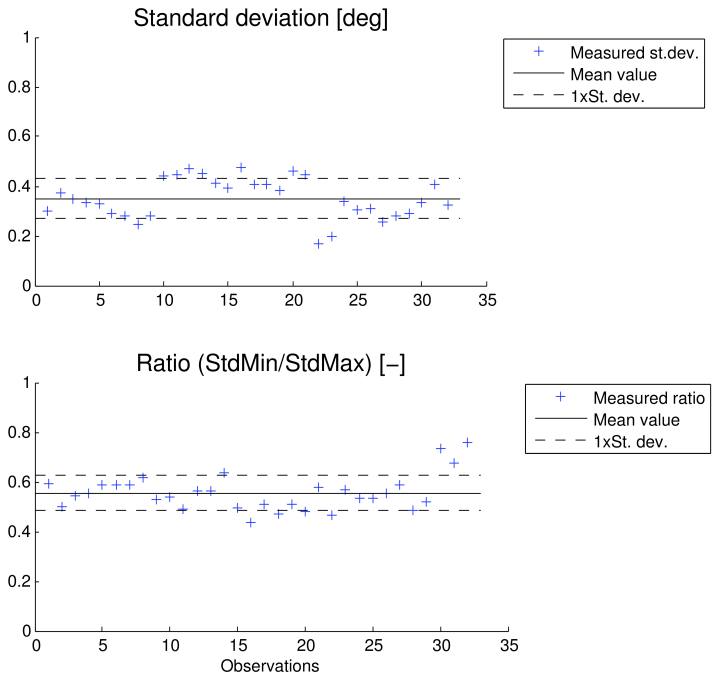

Figure 5.8: Standard deviation and ratio, H_S: 2, T_P: 9

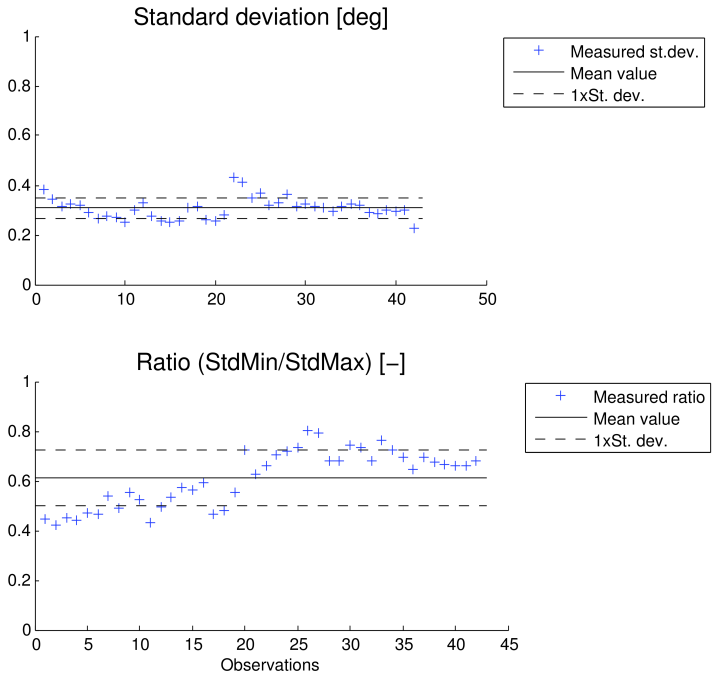

Figure 5.9: Standard deviation and ratio, H_S: 2, T_P: 10

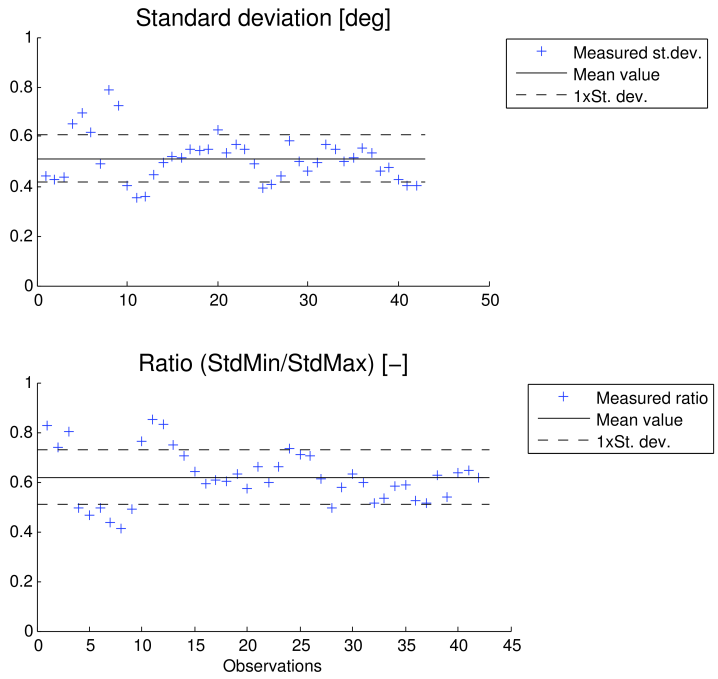

Figure 5.10: Standard deviation and ratio, H_S: 4, T_P: 10

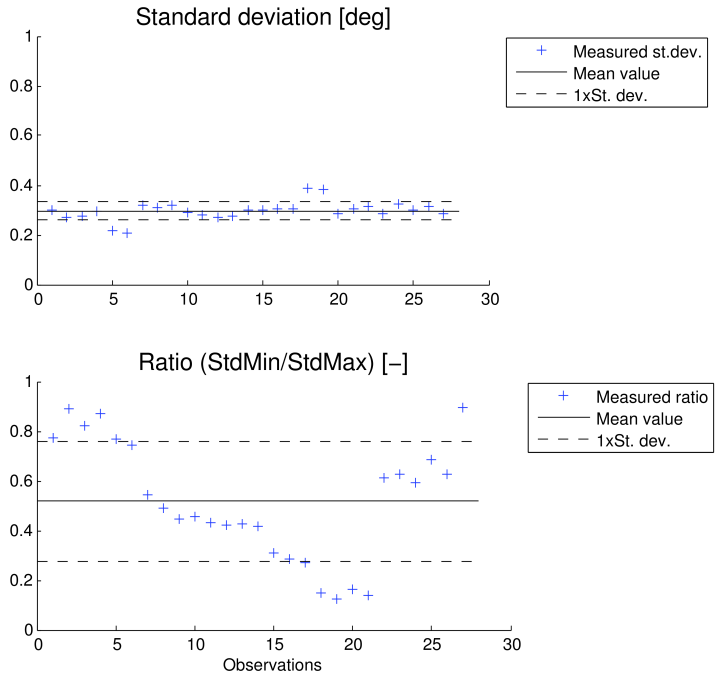

Figure 5.11: Standard deviation and ratio, H_S: 2, T_P: 12

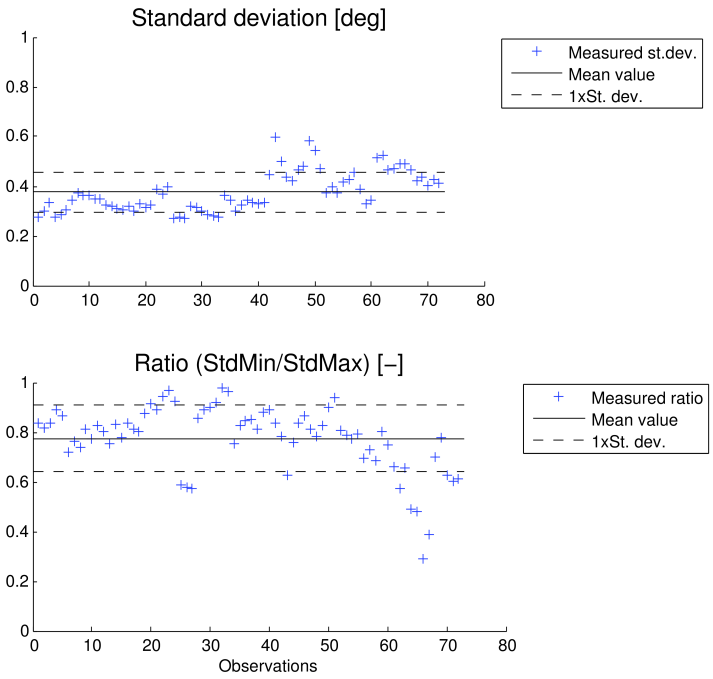

Figure 5.12: Standard deviation and ratio, H_S: 4, T_P: 12

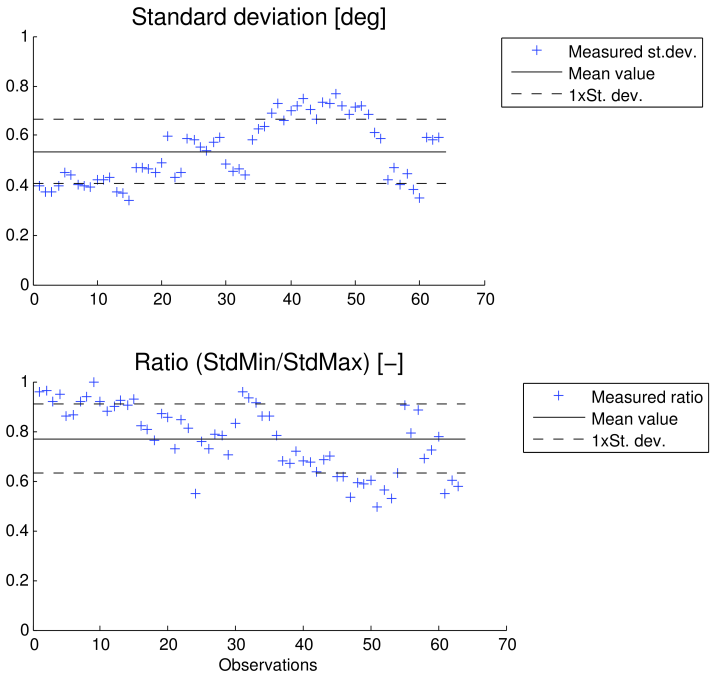

Figure 5.13: Standard deviation and ratio, H_S: 6, T_P: 12

To see any connections we need to plot them on the same graph. In the case of no waves, i.e. $H_S = 0\,\text{m}$, then we expect no motion with no standard deviation. If we were to assume linear theory where the motion is linearly proportional to H_S, we should be able to fit a straight line through the origin along with the measurements. In figure 5.14 we see that this is not the case.

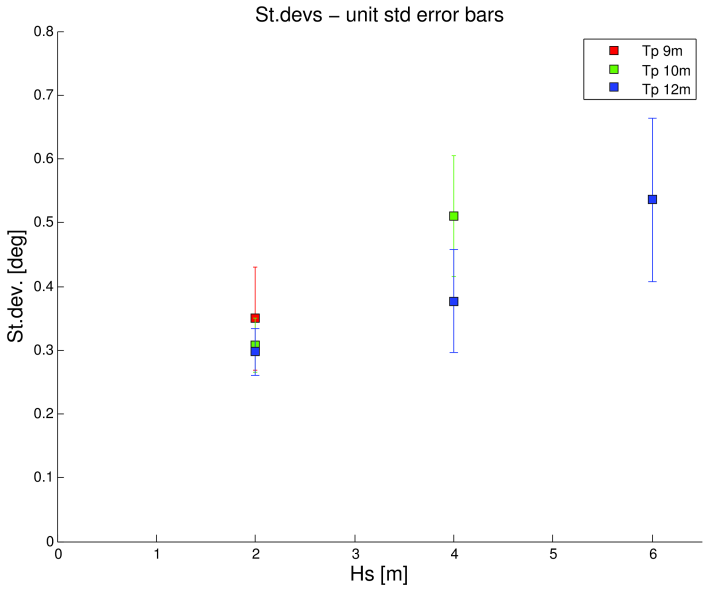

Figure 5.14: Standard deviation for the selected sea states. This illustrates that we expect the angle response to increase for higher significant wave heights.

One way to explain this would be to look at the driving factors of the motion. First of all, the motion is driven by the vessel motion. A vertical top tensioned riser will follow the rig as it is excited by the waves and currents. The second could be motion driven by eigenfrequencies being excited. It may be possible that the ratio between these two driving factors change for different H_S and/or T_P. To investigate this we need to take a closer look at the power spectra that can be found from the measurements at different sea states.

5.4.3 Power Spectra

The power spectra are found from the sampled data from the riser angle and are calculated using an algorithm called *Fast Fourier Transform*, FFT (WAFO-group, 2000) of the autocorrelation function (eq. 3.1) to find the *Discrete Fourier Transform*, DFT. Since the DFT is a non-continuous procedure it may appear very jagged. To make it more smooth the power spectra are smoothed using a smoothing parameter. The smoothing parameter that is used by the WAFO tool is selected by a trial and error approach. All power spectra are cut for all frequencies where $\omega \geq 2.0\,\text{rad/s}$ since there is no or little energy above this region in the calculated spectra and are of little interest.

Figure 5.15 shows the difference between the power spectra for the same sea states. The red dashed lines correspond to eigenfrequencies found in section 6.5. a) and b) are

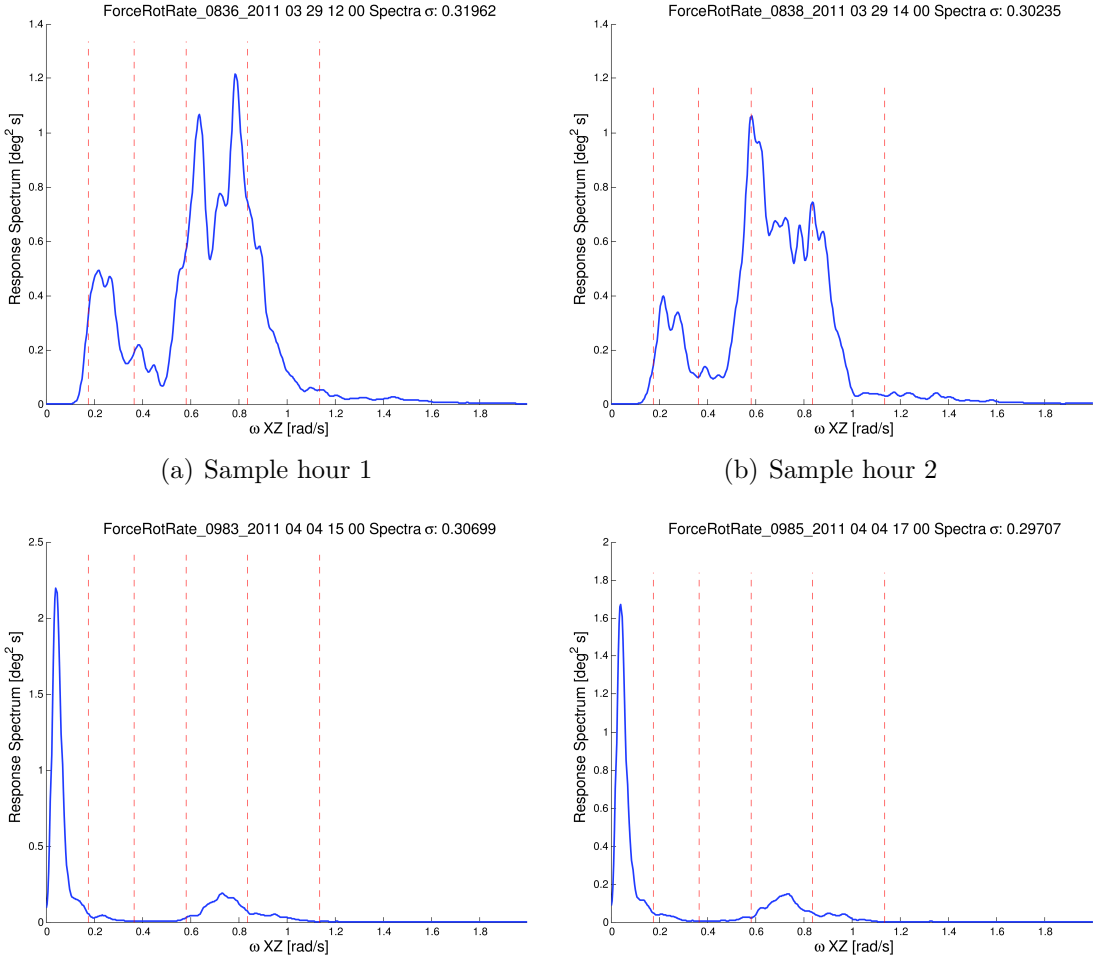

(a) Sample hour 1

(b) Sample hour 2

(c) Sample hour 3

(d) Sample hour 4

Figure 5.15: Two and two sample hours within same 3-hour window, H_S: 4 m, T_P: 10 s. The overall shape is different, but the standard deviation is still the same.

from the same 3-hour period and the same goes for subfigure c) and d). An interesting observation is that two spectra from the same 3-hour window are very similar which indicates stability for this time period for the spectra. However, there is a large difference to the other spectra. The spectra in c) and d) are heavily excited in the low frequencies, i.e. large periods. The periods may vary from 60 s up to 180 s which corresponds to an ω between circa 0.03 rad/s to 0.1 rad/s.

This slowly varying motion can be explained by slow drift of the rig. The eigenfrequencies are also far away from this motion and cannot be the main contributor to this. The eigenfrequencies are in general not very present in any of the spectra. The eigenfrequencies of the rig is an important parameter that isn't considered in the eigenfrequency calculations.

5.4.4 Bandwidth of Response Spectra

As discussed in section 3.3 we may have a broad banded stochastic response of the riser angle. We have seen that the spectra at different times, but for the same sea state, the shape of the spectra can be completely different. They have all varieties of broadness and moments. Interestingly, they all fall within a relatively narrow region of standard deviations. But the fatigue damage must be corrected when the process no longer can be regarded as a narrow-banded process (DNV, 2010).

From each measured hour the power spectrum for the angle has been approximated using the WAFO toolbox. From there the moments have been calculated according to equation 3.10. The broadness parameter ϵ has then been found using equation 3.17. The wide range of the broadness is shown in figure 5.16.

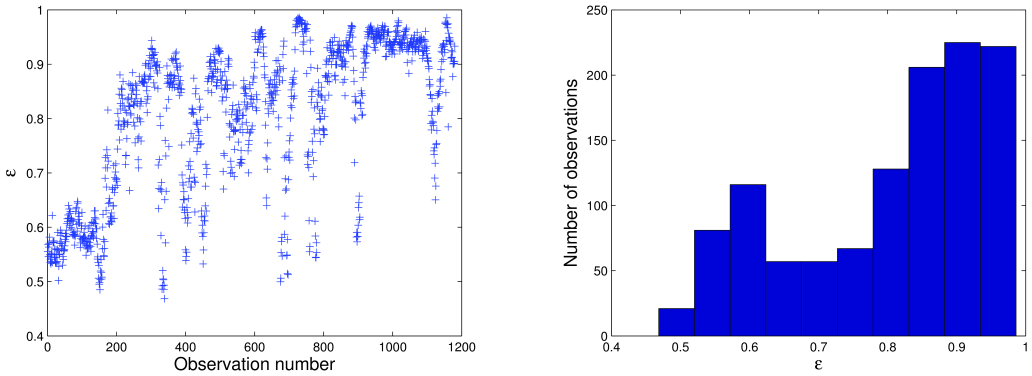

(a) All broadnesses (b) Broadness distribution

Figure 5.16: Spread of broadness parameter for all measurements. The majority of the measured broadnesses are very high.

To show the how the Rice distribution fits the different data collected for the maxima, a selection of random hours are shown in figure 5.17. The maxima from the data are shown in the histogram. The blue and red lines display the Rice distribution with ϵ found from spectral analysis and direct negative maxima counting, respectively.

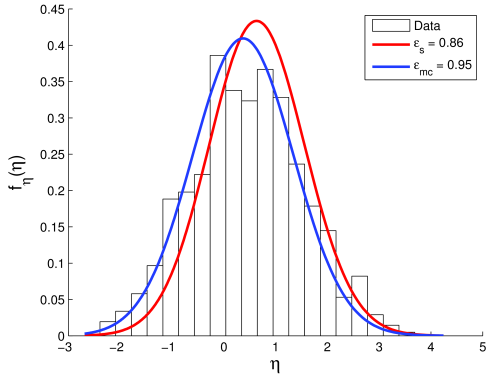

(a) Sample hour 1

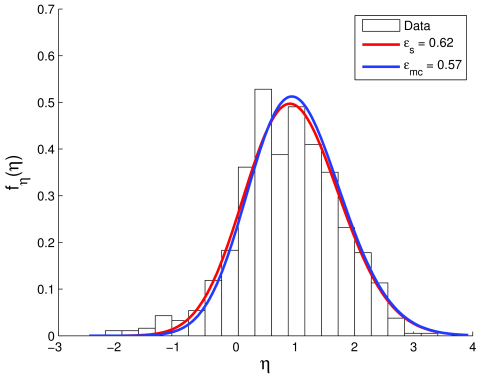

(b) Sample hour 2

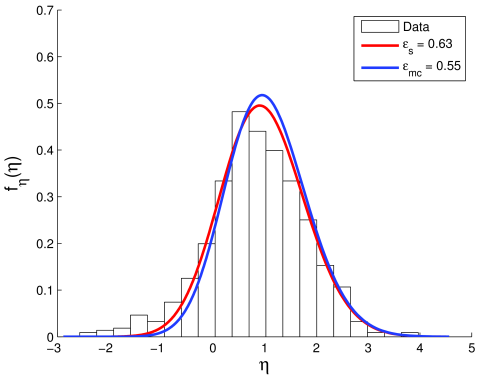

(c) Sample hour 3

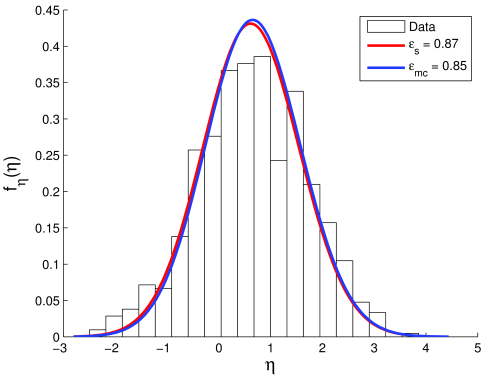

(d) Sample hour 4

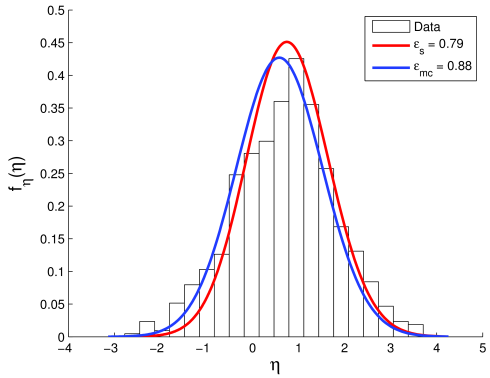

(e) Sample hour 5

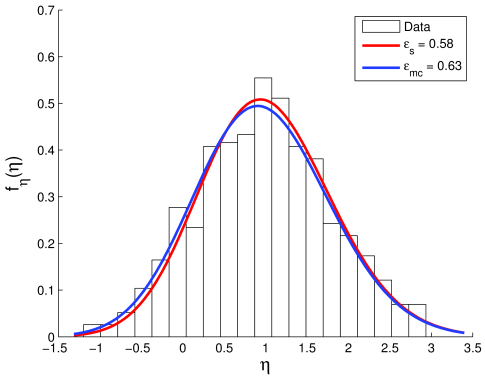

(f) Sample hour 6

Figure 5.17: Examples of fitted Rice distributions for different ϵ. The plots show a good consistency between the two methods of determining the broadness.

5.4.5 Angle Range and Fatigue

The fatigue accumulates differently around the circumference of the wellhead. A rainflow counting has been made for each 22.5° up to 157.5°, a total of 8 directions. The next direction would be 180°, but accumulates the same fatigue damage as 0° as discussed in section 5.3. Table 5.5 shows the damage on each control plane.

The long term distributions of cycles are calculated using the rainflow counting method which is implemented in the WAFO toolbox. The angle range spectrum is shown in figure 5.18. Each block represent a near-constant amplitude block with n_i cycles for block number i. Using the Miner-Palmgren's rule we find the cumulative damage for different control planes as defined in section 5.3.1.

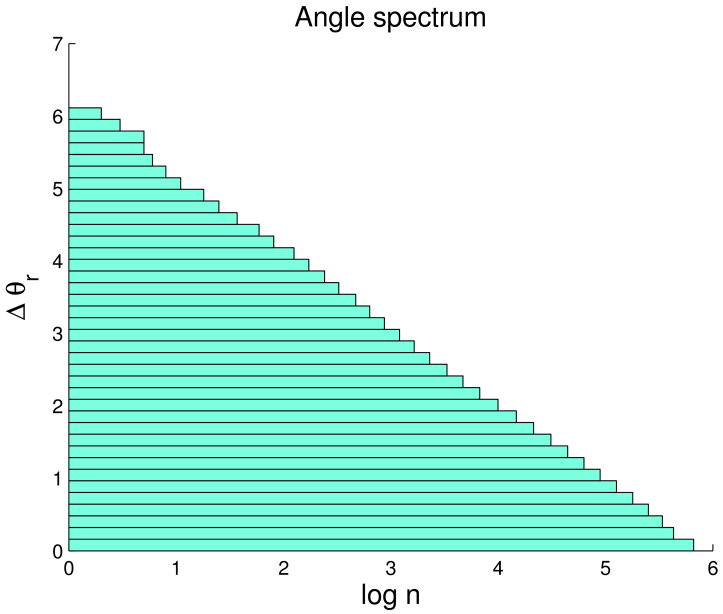

Figure 5.18: Angle spectrum from fullscale analysis where all 1180 time series are used. The Weibull fit follows the blocks very well. The figure represent the control plane with the highest accumulated fatigue damage.

The Weibull fit parameters in figure 5.18 are:

- $\Delta\theta_0 = 5.99°$
- $h = 1.06$
- $n_0 = 723725$

Which will give a cumulative damage using equation 4.14 of 0.009278.

The relative angles in the table are relative to a unknown fixed co-ordinate system, i.e. we don't know how the local XZ- and YZ-axes relates to north. Along the circumference the maximum difference is only 20 % between the most and the least damaged point.

Relative angle	Cumulative damage	n_0	$\Delta\theta_{r,0}$
θ_0	0.007845	662944	6.355
$\theta_{22.5}$	0.007997	723725	5.604
θ_{45}	0.008134	745517	6.545
$\theta_{67.5}$	0.008102	746507	6.758
θ_{90}	0.007564	725564	8.957
$\theta_{112.5}$	0.006754	727274	8.222
θ_{135}	0.006790	736211	6.014
$\theta_{157.5}$	0.007456	710264	6.219

Table 5.5: Cumulative damage for each control plane

However, in order to have a distribution that we can compare with results from RIFLEX we must choose only those time series which correspond to those sea states that actually are simulated in RIFLEX.

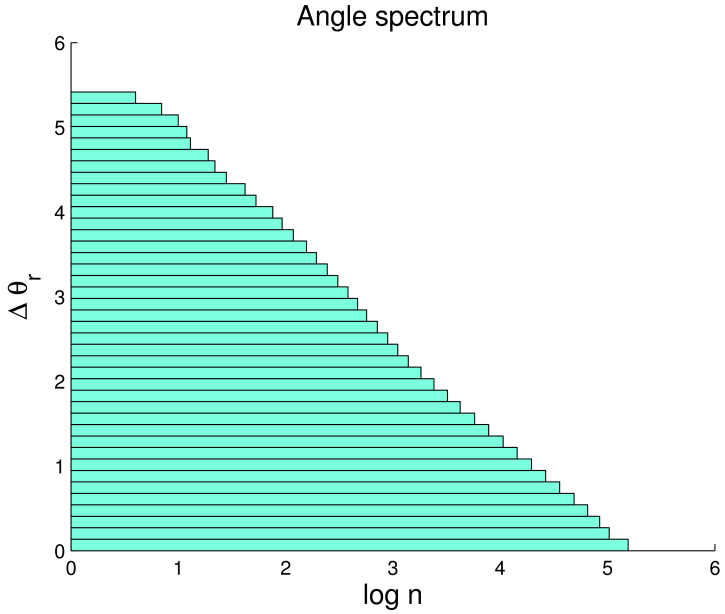

Figure 5.19: Angle spectrum from fullscale analysis, θ, selected sea states. The figure represent the control plane with the highest accumulated fatigue damage.

The Weibull fit parameters in figure 5.19 are:

- $\Delta\theta_0 = 5.67°$
- $h = 1.11$
- $n_0 = 157990$

Which will give a cumulative damage using equation 4.14 of 0.003201.

The complete long-term distribution of cycles are found from 1180 hours of data and the distribution for the selected sea states only have 246 hours of data. Consequently,

we have fewer cycles, and fewer cycles with high amplitudes.

Relative angle	Cumulative damage	n_0	$\Delta\theta_{r,0}$
θ_0	0.002460	143901	5.580
$\theta_{22.5}$	0.002544	157990	5.617
θ_{45}	0.002377	163033	5.581
$\theta_{67.5}$	0.002086	164295	4.764
θ_{90}	0.001707	160803	4.259
$\theta_{112.5}$	0.001395	162139	4.266
θ_{135}	0.001549	164281	4.989
$\theta_{157.5}$	0.002053	155656	5.362

Table 5.6: Cumulative damage for each control plane for selected sea states

If we plot the cumulative damage for each block in the Miner-Palmgren summation we get a picture of the most critical $\Delta\theta$'s. Even though there are some high peaks their contributions to the total damage picture is relatively small since they occur rarely. Figure 5.20 shows this distribution for the full scale data for our selected sea states.

It is interesting to see whether the high peaks should be regarded as important with respect to the total damage picture. If we find the area between the curve in figure 5.20 and the y-axis up to a certain $\Delta\theta$ we can compare the damage done by all cycles. The relative damage is shown in figure 5.21. If we for example neglect all cycles with $\Delta\theta \leq 4.0$ then our damage is only 91 % of the total damage. By neglecting the high peaks we introduce an error of roughly 10 %.

Also, from figure 5.21 we can see that cycles with $\Delta\theta \leq 1$ yield very little contribution to the cumulative damage.

5.4.6 Short-term Angle Range

For some selected time series with $H_S = 4$ and $T_P = 10$ we will compare the short term distribution of the angle range spectra in order to assess the difference between full scale measurement and simulations. This will illustrate the variation of the spectra and how low frequency domination affects them. The samples are now collected in 3 hours long time series.

Wave Frequency Dominated Motion

For the three hours that were analysed the angle range spectrum is shown in figure 5.23. Typical for all wave frequency dominated spectra is the convex shape, i.e. if it were to be fitted on a Weibull distribution, the shape parameter, β, is above 1.

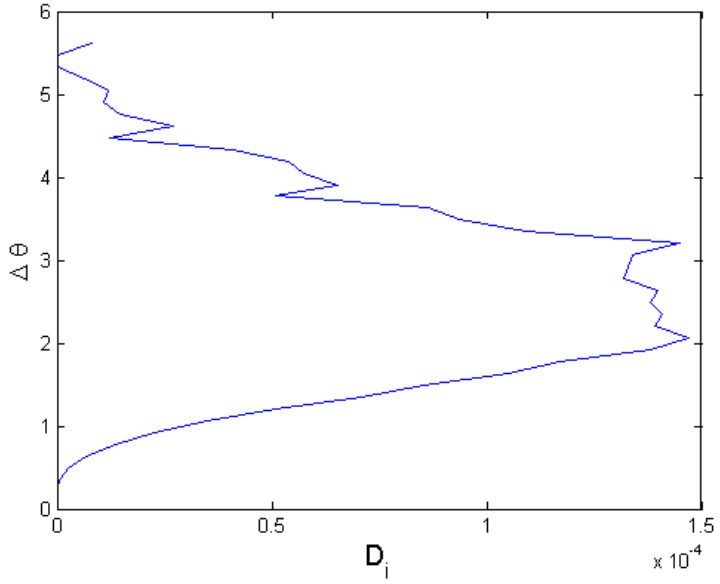

Figure 5.20: Cumulative damage for each block in Miner-Palmgren summation

Low Frequency Dominated Motion

Another time is then selected where the angle response is low frequency dominated. Otherwise, the significant wave height and the wave peak period are the same as for the wave frequency dominated example.

Different in this case relative to the other is the shape of the angle range spectrum. Where the spectrum for wave frequency dominated response had a smooth shape this spectrum is a bit more indeterminate with respect to shape. It is both concave and convex. This shape is actually representative for most time series with a high energy in the low frequency region.

Two points should be remarked; the standard deviation for both examples are very close to each other and the total number of cycles are approximately the same for all sea states with the same H_S and T_P. It is also worth noting that the maximum range for the majority of the spectrum with the same sea state parameters fall within the same region.

Since there are more cycles in the range region between $0.5° - 2.5°$ in the wave frequency dominated angle range spectrum we expect this to yield more cumulative damage.

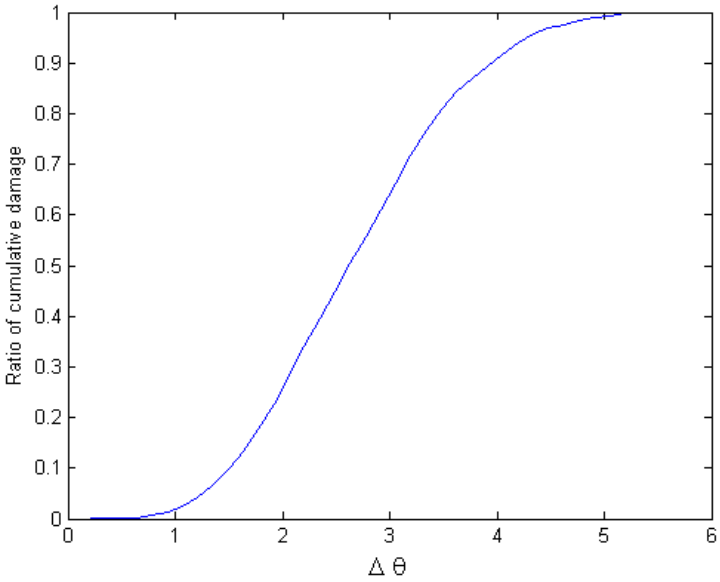

Figure 5.21: The share of damage for all cycles when all cycles above $\Delta\theta_i$ are neglected

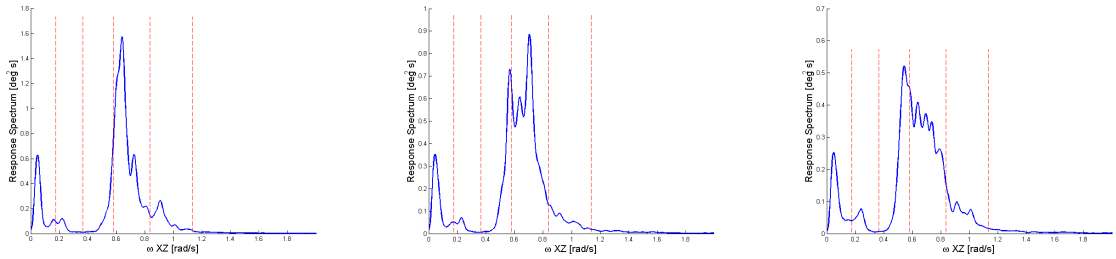

(a) Sample hour 1, $\sigma = 0.38$ (b) Sample hour 2, $\sigma = 0.36$ (c) Sample hour 3, $\sigma = 0.32$

Figure 5.22: Power spectra for the xz angle for three succeeding hours. All three spectra have most of the energy focused in the wave frequency domain and low energy for low frequencies. H_S: 4, T_P:10.

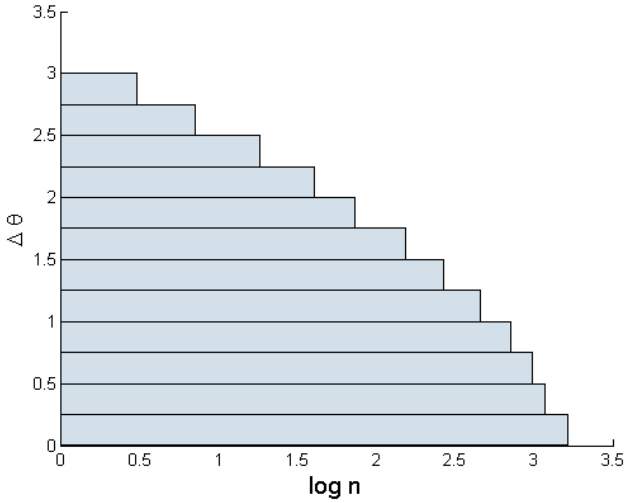

Figure 5.23: Full scale angle range spectrum for 3-hour time series. The time series are the same as for the angle spectra shown in figure 5.22

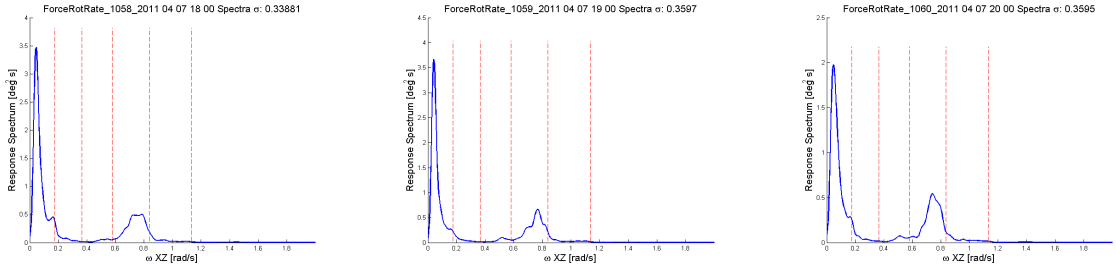

(a) Sample hour 1, $\sigma = 0.34$ (b) Sample hour 2, $\sigma = 0.36$ (c) Sample hour 3, $\sigma = 0.36$

Figure 5.24: Power spectra for the xz angle for three succeeding hours. All three spectra have most of the energy focused in low frequency domain and low energy in the wave frequency range. H_S: 4, T_P:10.

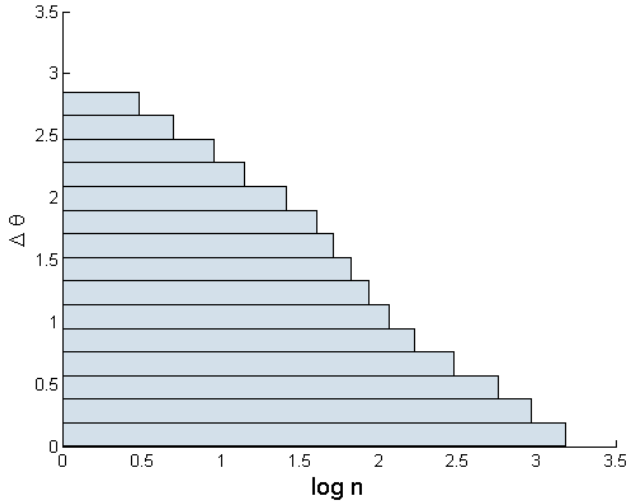

Figure 5.25: Full scale angle range spectrum for 3-hour time series. The time series are the same as for the angle spectra shown in figure 5.24

Chapter 6

Simulation Models

The wave loading can be simulated in many various ways. The base input files for RIFLEX was originally containing unidirectional single-peaked wave spectra. The lack of spreading in the waves yield a worst case scenario since all the cumulative damage from the waves are concentrated at a single point on the wellhead circumference. The situation is only a theoretical one and would never occur in the real world. This chapter will find how different wave models will affect the cumulative damage on the wellhead when directional spreading in the environmental actions are taken into account.

6.1 Literature Review

Several papers has been written regarding the motion of floating offshore structures, e.g. a semi-submersible or tension leg platforms and many studies have been made for marine risers on the problem of vortex-induced vibrations.

A paper describes a full scale riser measurement in the Spanish Mediterranean. The comparison was divided into three basic categories (Connolly and Wybro, 1984):

1. Regular wave time domain analysis.
2. Random wave time domain analysis.
3. Frequency domain analysis.

The study was focus on the calculated errors in the wave-active zone and the values near the bottom of the riser. They concluded that the wave interaction with the rig itself played an important role in the response near the top. They compared the bending stress with and without hull interaction on the fluid kinematics. The difference in the wave-active zone had the most severe differences for all methods, where the transfer function method under-predicted by up to 50 % in some cases, while the regular wave analyses tended to both under-predict and over-predict. The regular wave method did show more correct and consistent results with the full scale analyses with increasing

storm severity. The random wave showed that it tended to over-predict the bending stress.

For the lower part of the production riser they did get consistent results between full scale and the calculations for all three categories. This region is less influenced by the body-wave interaction at the surface.

Another paper that was focused around the bending moment in the wave zone for a drilling riser in the North Sea was presented in 1983. The comparison work was based on the difference in full scale measurements and beam theory assuming that the marine riser could be described using the differential equation for tensioned beams (Verbeek, 1983):

$$\frac{\partial^2}{\partial z^2}\left(EI\frac{\partial^2 x}{\partial z^2}\right) - \frac{\partial}{\partial z}\left(T\frac{\partial x}{\partial z}\right) + m\frac{\partial^2 x}{\partial t^2} = F, \tag{6.1}$$

where E is the Young's modulus, I is the moment of inertia, T is the riser tension, m is the mass per unit length, z is the axial coordinate along the riser, F is the hydrodynamic forces on the riser and x is the horizontal deflection of the riser.

A particular concern in this report was the values of the constants in Morison's equation. From steady and harmonic flow experiments it is known that the coefficients are correlated with Reynolds number and Keulegan-Carpenter number (Verbeek, 1983). The study covered a sensitivity study using the following combinations:

1. $C_D = 0.7$, $C_M = 1.4$, used for small, smooth columns.
2. $C_D = 0.6$, $C_M = 2.0$, as sometimes used for design of offshore structures.

For these sets of values the response was found to vary significantly.

The theory calculations were made by analytic approaches and numerical random time simulations and it was concluded that the theoretical predictions proved to be fairly successful compared to full scale measurements. The comparison was based on the characteristic properties of the riser in the wave-active zone; standard deviations of bending stress were in-line with theoretical predictions and probability distributions are non-Gaussian which was predicted by the theoretical models assuming Morison's equation as description for the hydrodynamic force (Verbeek, 1983).

To investigate the discrepancies between measured and calculated riser response for a flexible riser a paper looked for explanations using non-linear material properties (Sødahl et al., 1992). The riser had a steep wave configuration as shown in figure 6.1.

The investigation was focused on the riser curvature in the hog bend. They used the computer program RIFLEX and the comparison was based on the standard deviation of the curvature as a function of the significant wave height. By running different cases with varying stiffness models and damping models they found that a hysteretic model combined with a rather low Rayleigh damping gave good agreements with the full scale data.

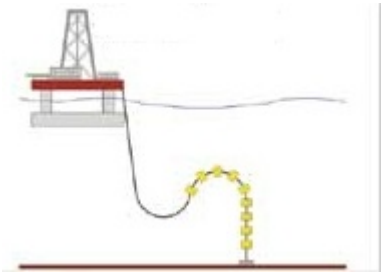

Figure 6.1: Steep wave riser configuration

6.2 Wave Spectra

The definition of the spectral density is described in section 3.2. This chapter will describe how the spectral density is used in practice by computer programs to simulate a realisation of the sea state.

6.2.1 Unidirectional Spactra (Long-Crested Waves)

The unidirectional single-peaked waves or infinitely long-crested waves are described by a three-parameter JONSWAP spectrum. The input parameters are H_S, T_P and γ, where γ is found given by default from (Marintek, 2010):

$$\gamma = \exp\left(5.75 - 1.15\frac{T_P}{\sqrt{H_S}}\right). \tag{6.2}$$

It is tempting to believe that unidirectional incoming waves will induce a response in the same plane as the wave direction. As figure 6.2 shows this is only partly true. When the structure is symmetric from the wave direction there is no coupling between the in line motion and perpendicular motions including rotation d.o.f's, e.g. yaw, at least in a pure mathematical sense. When the waves attack from an angle they will induce motions in many d.o.f's which are coupled. Figure 6.2(a) shows a response when the wave direction is exactly the same as the vessel's local x-axis. The response lies in one plane only. Figure 6.2(b) shows that this is not true for all situations.

As we want to find the standard deviation of the response in all planes, and not only in the xz- and yz-planes, which can be plotted. We can find a sinusoidal pattern for the variance and the resulting standard deviation will be the square root of a sine function. From this we can then find the main direction and the lowest corresponding to the major and minor axes in an ellipse. The ratio between them gives the 'thickness' of the ellipse. A ratio of 1 is a perfect circle and a ratio of 0 corresponds a perfect 1-directional response. In the data representation, use of the term *ratio* will not be used as the ratio between the major and minor axis, but as the ratio between the highest and lowest standard deviation the ellipse yields.

Under the assumption of a bivariate normal distribution we can find the covariance

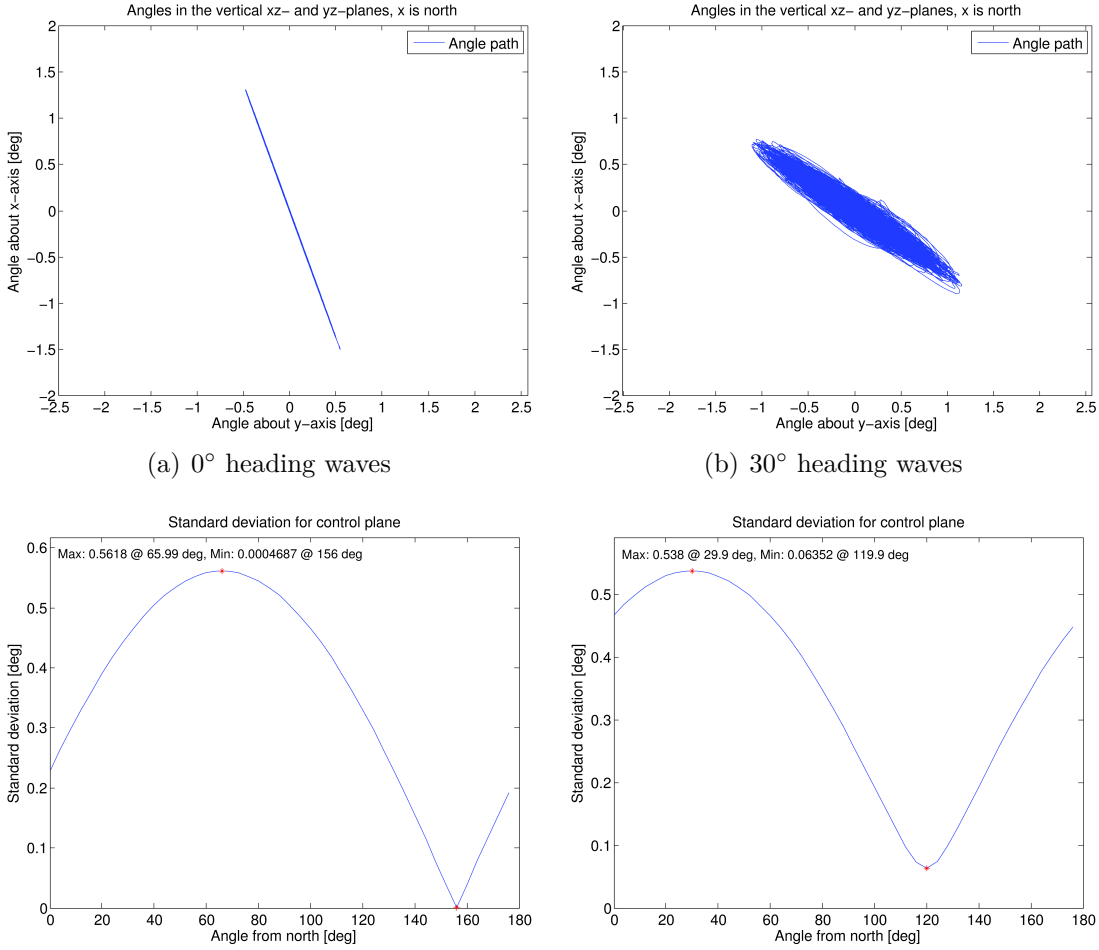

(a) 0° heading waves

(b) 30° heading waves

(c) 0° heading waves

(d) 30° heading waves

Figure 6.2: Riser response for two different heading directions

matrix which is defined in equation 3.6, where X_1 and X_2 are rotation about the x- and y-axes, respectively. The principal axes to the ellipsoid, i.e. equidensity contours of the bivariate normal distribution, can be found from the eigenvectors of the covariance matrix, $\mathbf{\Sigma}$. The corresponding eigenvalues of the matrix yield the variance of those axes.

Torsethaugen Spectrum

The Torsethaugen spectrum model was developed by fitting two JONSWAP spectra. A double peaked spectra representing both wind and swell sea states was established to be used for design purposes on the Norwegian continental shelf (Torsethaugen and Haver, 2004). The Torsethaugen spectrum can be modelled in RIFLEX with only two input parameters, H_S and T_P (Marintek, 2010).

Wave Realisation

The energy per area in a linear wave is given by

$$E_n = \frac{1}{2}\rho g \zeta_{An}^2, \tag{6.3}$$

for wave component n and ζ_{An} is the wave amplitude for the same component (Myrhaug, 2007). We then have that the total energy for all wave components are given by

$$\frac{E}{\rho g} = \sum_{n=1}^{N} \frac{1}{2}\zeta_{An}^2(\omega_n). \tag{6.4}$$

By introducing that the energy for a wave component should equal the energy for all wave component produced by the spectrum within a small region we get

$$\frac{1}{2}\zeta_{An}^2(\omega_n) = S(\omega_n)\Delta\omega. \tag{6.5}$$

When we combine equation 6.4 and 6.5 the total energy is

$$\frac{E}{\rho g} = \sum_{n=1}^{N} S(\omega_n)\Delta\omega. \tag{6.6}$$

If we now let $N \to \infty$ and $\omega \to 0$, we can rewrite the total energy into (Myrhaug, 2007)

$$\frac{E}{\rho g} = \int_0^\infty S(\omega)\mathrm{d}\omega, \tag{6.7}$$

which is equal to the first spectral moment m_0 or σ^2 (equation 3.11). From equation 6.5 we have that

$$\zeta_{An} = \sqrt{2S(\omega_n)\Delta\omega}. \tag{6.8}$$

When a linear wave is assumed with a uniformly random distributed phase angle ϵ_n the total wave elevation is given by

$$\zeta(x,t) = \sum_{n=1}^{N} \sqrt{2S(\omega_n)\Delta\omega}\cos(\omega_n t - kx + \epsilon_n), \tag{6.9}$$

where k is the wave number. The dispersion relation gives the connection between the wave frequency and the wave number for a finite water depth as

$$\frac{\omega^2}{g} = k \tanh(kh). \tag{6.10}$$

For water depths where $h \to \infty$, equation 6.10 can be written as

$$\frac{\omega^2}{g} = k. \tag{6.11}$$

We see that from realisation to realisation, everything is constant. The only parameter that may change is the phase angle ϵ_n. The phase angle is unaffected by the spectrum. This is in accordance with the statement that two different realisation with the *same* characteristics yields the same power spectrum.

6.2.2 Multi-Directional Spectra (Short-Crested Waves)

In real life there will almost always be a presence of waves from different directions. This makes the surface look more chaotic and complex. We may now have different wave component with the *same* frequency, but with different direction. To account for this each wave component are now divided into both frequency and directional dependence.

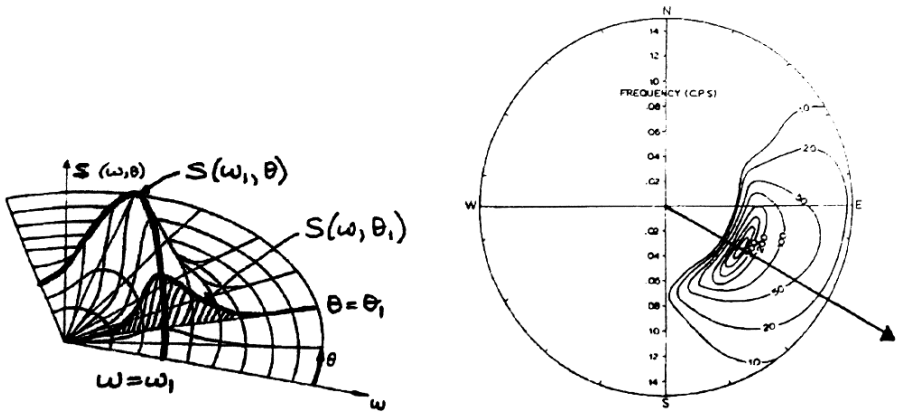

(a) Lines for constant ω or θ

(b) Example of measured directional spectrum - direction according to maximum spectral density

Figure 6.3: Illustration of directional spectra (Myrhaug, 2007)

The amplitude of each wave component are now modified to be

$$\frac{1}{2}\zeta_{Anm}^2 = S(\omega_n, \theta_m)\Delta\omega\Delta\theta. \tag{6.12}$$

By using the same procedure as for the unidirectional spectra we get the wave elevation at any point at any time as

$$\zeta(x,y,t) = \sum_{n=1}^{N}\sum_{m=1}^{M}\sqrt{2S(\omega_n,\theta_m)\Delta\omega\Delta\theta}\cos(\omega_n t - k_n x\cos\theta_m - k_n y\sin\theta_m + \epsilon_{nm}) \quad (6.13)$$

In general, the directional spectrum is given by

$$S(\omega,\theta) = S(\omega)D(\theta,\omega). \quad (6.14)$$

Here, the directional spreading function, $D(\theta,\omega)$, is not necessarily independent of the frequency. To simplify the problem we may make it independent of the frequency so that we may write the complete spectrum as

$$S(\omega,\theta) = S(\omega)D(\theta). \quad (6.15)$$

The most common shape of the directional spreading function is on the form

$$D(\theta) = \begin{cases} K_n\cos^n\theta & \text{for } -\frac{\pi}{2} < \theta < \frac{\pi}{2} \\ 0 & \text{elsewhere} \end{cases}, \quad (6.16)$$

where

$$K_n = \frac{2^{n-1}}{\pi}\frac{\Gamma\left(\frac{n}{2}\right)\Gamma\left(\frac{n}{2}+1\right)}{\Gamma(n)}. \quad (6.17)$$

K_n is defined in order to ensure that (Myrhaug, 2007)

$$\int_0^{2\pi} D(\theta,\omega)\mathrm{d}\theta = 1. \quad (6.18)$$

This is also the only way to define a spreading function in RIFLEX (Marintek, 2010).

Finding a suitable n-value for the spreading parameter is not straightforward. Many measurements have been made to find the one best fitting. It varies from position to position and is also dependent on the significant wave height. A common trend is that the waves become more long-crested for higher waves (Kvitrud, 1996).

According to (NORSOK, 2007), in the absence of documentation, the exponent n is taken to the most unfavourable value between 2 and 10. The values can be used in moderate sea states, i.e. $H_S < \sim$10 m. The chosen significant wave heights are 2 m, 4 m and 6 m. Since the tendency is that the waves are more long-crested in higher seas, we simply approximate; $n = H_S$. For higher n-values the energy is more concentrated along the mean wave direction. This will also reduce the massive amount of simulations to be performed in order to find the *worst case*.

6.3 Sea States

The system will be subjected to different direction of loading from the waves. As figure 5.1 shows, there are some directions more interesting to this particular case. For the directions where few or none observations are made it is not necessary to run any simulations since this will not yield any new information.

The system will be simulated with waves from 4 different directions. The rig's heading direction will always be kept constant. Each direction increment is 30°. For each direction it will be subject to waves from a JONSWAP spectrum where H_S and T_P are changed. γ is changed according to equation 6.2. For each direction there will be a total of 6 sea states according to table 5.3.

For the same mean heading directions and sea states with the same H_S and T_P the other simulations will be run with a Torsethaugen wave spectrum, which use empirical data to account for both wind sea and swell sea waves.

6.4 Simulation Time

As RIFLEX seemingly simulates each sea state randomly there is a certain consistency between two simulations between each run time. This can be avoided with a so-called pseudo-random seed number. A sea state can have infinite different realisations. For a given seed number we will have the same realisation.

We are interested in the standard deviation of a motion. We can compare the standard deviation for a series of test runs with different "randomly" chosen seed numbers to simulate different realisations of the same sea state. For every realisation we take the standard deviation of the motion for different time steps. In theory, the standard deviation should for a continuous and non-discrete sea state should converge toward a certain value as the time goes to infinity.

To find the appropriate time of simulation to run a series of 31 realisations have been simulated in RIFLEX. The standard deviations have been extracted to show the trend over time in figure 6.4. In the first minutes of the simulation the scattering is widely spread, but is fairly converged after 60 minutes. The convergence continues beyond this point but is satisfactory for the purpose of our analyses.

The dotted lines follow the standard deviation for each realisation and the red lines are envelope curves. The red dashed line is the mean value of all standard deviations. Based on this graph we need to run each sea state only one time, i.e. one realisation for 60 minutes to reach an acceptable error.

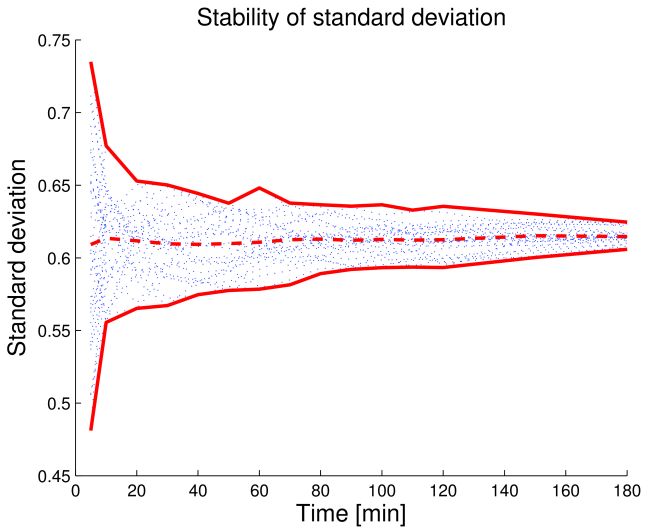

Figure 6.4: Stability of standard deviation and convergence

6.5 Eigenfrequencies

The eigenmodes and eigenfrequencies of the marine riser can be found in RIFLEX. RIFLEX uses the Lanczos' method to find a solution of the eigenvalue problem (Marintek, 2010). The first six modes are listed in table 6.1. We can use these frequencies to identify any secondary peaks in the power spectra. All six eigenmodes' shape follows the classic n-th mode sine shape. Figure 6.5 shows the 4^{th} eigenmode.

Eigenvalue no	Eigenvalue	Circular freq. [rad/s]	Natural period [s]
1	0.0305	0.1747	35.97
2	0.1327	0.3643	17.25
3	0.3385	0.5818	10.80
4	0.7003	0.8368	7.51
5	1.2874	1.135	5.54
6	2.1787	1.476	4.26

Table 6.1: Calculated eigenfrequencies from RIFLEX

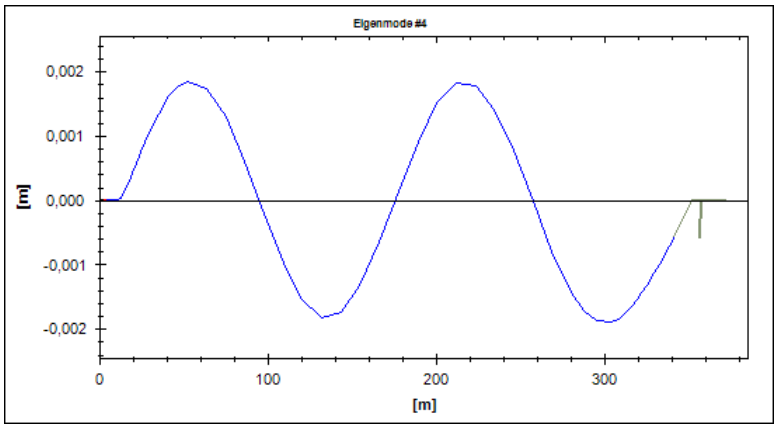

Figure 6.5: The fourth eigenmode from static RIFLEX calculations. As for most slender one-dimensional structures it nearly follows a perfect sine curve.

6.6 Non-Linear Effects

Non-linear forces and perturbation of the system can have a large variety of effects regarding the behaviour of the structure. We can account for the amplitude of the waves and the heave and pitch motion of the vessel affecting the wetted surface of the rig's column and pontoons. It also changes the wetted surface of the marine riser itself. We can also have material non-linearities or non-linearities in boundary conditions such as non-linear stiffness in a spring. Another example is the velocity term in Bernoulli's equation.

6.6.1 Bernoulli's Velocity Term

The pressure in an incompressible, irrotational and inviscid fluid changes with the velocity squared

$$p + \rho\frac{\partial\phi}{\partial t} - \frac{\rho}{2}V^2 + \rho g z = C \tag{6.19}$$

The velocity term isolated is then

$$-\frac{\rho}{2}(V_i^2 + V_j^2 + V_k^2) = -\frac{\rho}{2}|\nabla\phi|^2. \tag{6.20}$$

The second-order velocity term can also be found in the Morison's equation

$$\mathrm{d}F = \rho\pi\frac{D^2}{4}C_M a_1 + \frac{\rho}{2}C_D D|u|u, \tag{6.21}$$

where C_M is the added mass corrected constant, C_D is the drag coefficient, a_1 is the transverse fluid acceleration and u is the relative fluid velocity. Morison's equation yields

the unit hydrodynamic force on a slender structure, e.g. a marine riser, submerged in a fluid. u is is the relative fluid motion meaning that this is the sum of all velocity components and subtracted the structure velocity and is decomposed as

$$u = u_{waves} + u_{current} - u_{structure} \tag{6.22}$$

In an idealised situation where we have a sea state composed of two waves with different frequency and amplitude we can approximate the velocity as

$$V = A_1 \cos(\omega_1 t + \epsilon_1) + A_2 \cos(\omega_2 t + \epsilon_2). \tag{6.23}$$

When equation 6.23 is inserted into equation 6.20 and the terms are expanded we get

$$\begin{aligned} -\frac{\rho}{2}V^2 = -\frac{\rho}{2}\Bigg[& \frac{A_1^2}{2} + \frac{A_2^2}{2} + \frac{A_1^2}{2}\cos(2\omega_1 t + 2\epsilon_1) \\ & + \frac{A_2^2}{2}\cos(2\omega_2 t + 2\epsilon_2) \\ & + A_1 A_2 \cos\left[(\omega_1 - \omega_2)t + \epsilon_1 - \epsilon_2\right] \\ & + A_1 A_2 \cos\left[(\omega_1 + \omega_2)t + \epsilon_1 + \epsilon_2\right]\Bigg] \end{aligned} \tag{6.24}$$

The first thing to notice when the second-order terms are accounted for we have terms oscillating with the frequencies $(\omega_1 - \omega_2)$ and $(\omega_1 + \omega_2)$. Often, the critical term is the difference term. This term can produce slowly varying excitation forces which may cause resonance in the slow d.o.f.'s such as surge, sway and yaw. A moored structure such as a rig may have eigenperiods in these d.o.f.'s because of the relatively low stiffness to mass ratio. Typical resonance periods are 1-2 minutes (Faltinsen, 1990). This can be a possible explanation for the peaks in the low frequency region in figure 5.15. The high frequencies may be connected to the higher eigenmodes of the marine riser itself with natural periods for the 5^{th} and 6^{th} mode at 5.54 s and 4.26 s, respectively.

The transverse external loads on the marine riser are calculated according to Morison's equation in RIFLEX, i.e. the velocity squared terms are not neglected (Marintek, 2011).

Current Interaction on Velocity Term

When a current is present we have an additional constant term in the velocity. The current may still vary along the z axis having a decaying profile from the surface to the sea floor. Assume a regular sea state with a constant current where the velocity at a point is formally written as

$$u = u_c + u_w \cos(\omega t + \epsilon) \tag{6.25}$$

Then the second-order velocity term in Morison's equation becomes

$$u|u| = u_c + u_w \cos(\omega t + \epsilon)|u_c + u_w \cos(\omega t + \epsilon)|. \tag{6.26}$$

It is obvious that the presence of the current will give a constant time-averaged drag force proportional to $\sim u_c^2$. If $u_c = 0$ then the time average becomes 0. Let us express the relative velocity between the current component and the wave component like this

$$u_c = \lambda u_w. \tag{6.27}$$

If we now set u_w to unity we can find how the time averaged force relates for varying λ. We now write the time average of equation 6.26 into

$$\overline{F_d} = \frac{1}{2\pi} \int_0^{2\pi} (\lambda + \cos(\omega t + \epsilon)) \left|\lambda + \cos(\omega t + \epsilon)\right|. \tag{6.28}$$

We can now plot how the two components will affect the total drag force. Subfigure 6.6(a) shows how the total drag increases for increasing current relative to wave velocity. Subfigure 6.6(b) shows the strength of the drag force produced by the wave in relation to the current produced drag force.

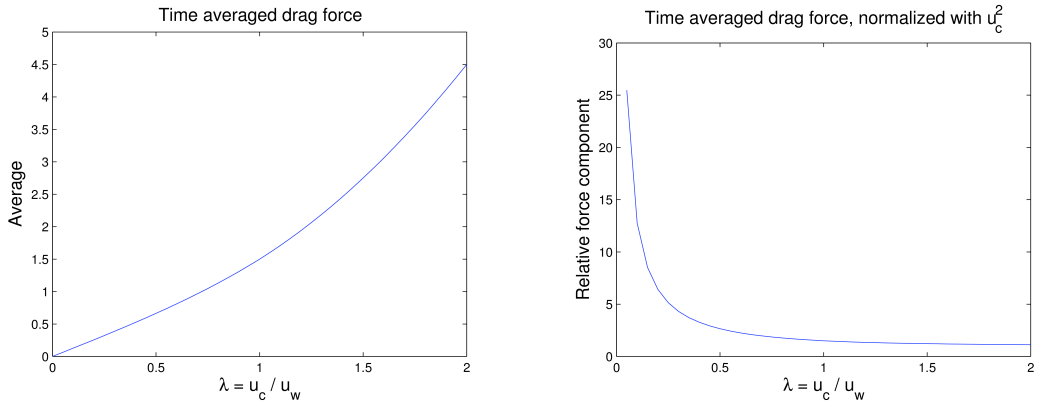

(a) Average drag force

(b) Wave force relative to current force

Figure 6.6: The average drag force and relative component contribution. The mean force from the wave alone is always zero, and for the current alone should give a 1-to-1 relation. The combined effect increases the average drag force.

For small λ the governing force comes from the waves. When this is the case the time average drag force goes to 0. For large values of λ we see that the u_c^2 normalised plot goes to 1, meaning that the current yields the main driving drag force.

6.6.2 Boundary Conditions

At the bottom on the LMRP the flex joint is modelled as a rotational spring. The original model implemented this spring as a linear spring with the rotational spring stiffness 37.98 kNm/°. A linearisation of the spring stiffness can be a good approximation if the choice of the secant point is a good one and that it within the angle domain of interest represent the physical spring with small errors. Another common way to linearise is to use the initial tangent of the non-linear force. Figure 6.7 shows the difference between the two characteristics.

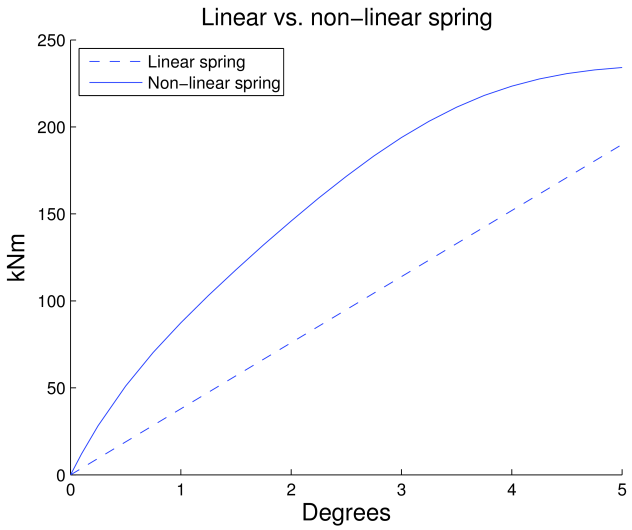

Figure 6.7: Characteristics between the linear and non-linear spring. This shows the static stiffness relation. The true stiffness in a dynamic context is different than this figure.

For the first degrees it is easy to see that the used linear approximation is not a good one. Very large degrees are not of interest in our case. Since the measured angle is very close to the spring it is expected that this correction will yield very measurable results in our analyses.

Many of the measured data shows that the angles are in the region 1° – 2°. If the secant were placed at 1.5 degree, the linearised stiffness should be 78.6 kNm/°.

Figure 6.7 only shows the reaction moment of the flex joint in a static case. The true behaviour is even more complex. The non-linear flex joint also have a damping term that should not be neglected and the true tangential stiffness in a dynamic context is different from the tangential stiffness in a static context. In general, the total stiffness in a dynamic case is stiffer than that of a static case (Holden, 2012).

6.7 Support Vessel Offset

The rig shall be placed, after best effort, as aligned with the wellhead as possible. With a DP system this is easier, but for an anchored system there will always be an offset in calm sea. And we also get an offset when there is a current present. The mooring system is essentially a spring and the current will move the rig into another equilibrium point.

Figure 6.8 shows a sketch of the offset situation. Let x be the offset from the align point and d be the distance from the top of the LMRP and the UFJ. The chord is then the hypotenuse and will consequently be longer than the initial length, d, and must be compensated by the heave compensating system. The figure also shows the LFJ angle in relation to the other lines. This angle is in general not the same as the chord angle. It is also possible that this angle may be lower than the chord angle due to the net positive buoyancy for large lengths of the riser.

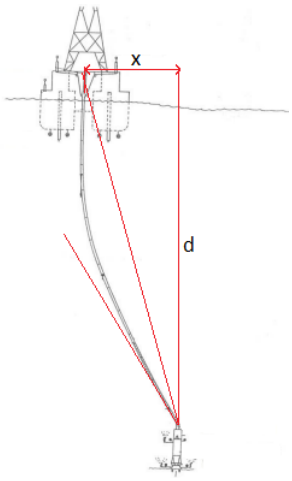

Figure 6.8: Support vessel offset

A typical critical value for stopping the drilling operation (with DP) is 4° for manual shut down and 5° for start of a automated shut down procedure (Framnes and Gleditsch, 1994). In a dynamic situation the largest angle will always be higher than the static angle. For this reason we set the maximum critical value for the static offset to correspond an angle of 3°. To find the actual offset in distance that will yield this angle an Excel sheet provided by (Sparks, 2007) that will calculate the riser's displacement, curvature and angle based on the riser's characteristics (see Appendix A). The rig's offset is found to be 27.4 m to yield a 3° angle at the LFJ. This value is found based on a free rotation of the LFJ which is not true in a real case. The chord angle for this offset is $\tan^{-1}(27.4/335) = 4.68$.

This will impact the result in several ways. First, the offset itself will affect the characteristics of the mooring system. Secondly, it will have an initial angle at the LFJ, in turn having different stiffness due to the non-linear behaviour of the flex joint as described in section 6.6.2. This should affect the response much in the same way as a current. Unfortunately, we cannot do so much about the first effect.

Chapter 7

Simulation Results

This chapter will present all the results from the RIFLEX simulations. There are a total of 7 different simulation models where 5 of them will be compared in chapter 8. The 5 models will be presented in the following order:

- Section 7.1: Unidirectional JONSWAP waves.
- Section 7.2: Unidirectional Torsethaugen waves.
- Section 7.3: Unidirectional Torsethaugen waves with introduction of non-linear modelling of the Lower Flex Joint (LFJ).
- Section 7.4: Torsethaugen waves with cosine distributed wave spreading.
- Section 7.5: Torsethaugen waves with cosine distributed wave spreading and introduction of non-linear modelling of the Lower Flex Joint (LFJ).

For those 5 simulation models the standard deviation of the angle motion and the thickness ratio of the motion ellipse (see section 5.3.2), spectrum and spectrum broadness parameter ϵ, fatigue results using both Miner-Palmgren summation and closed form fatigue using Weibull fitted curves will be compared. There will also be a comparison of the short-term angle spectra which also includes the current and offset simulations. All simulations are collected in table 7.1 to show how the effects are implemented for the different calculations.

The last two simulations are not similar to the first five since they all have the same sea state, i.e. constant H_S and T_P, but with varying parameters of current in section 7.6 and vessel offset in section 7.7. The purpose is to show how the angle motion will be affected by the introduction of these aspects.

Section	Wave spectrum	Wave spreading	Non-linear flex joint	Current	Offset	Varying mean wave direction
7.1	JONSWAP	✗	✗	✗	✗	✓
7.2	Torsethaugen	✗	✗	✗	✗	✓
7.3	Torsethaugen	✗	✓	✗	✗	✓
7.4	Torsethaugen	✓	✗	✗	✗	✓
7.5	Torsethaugen	✓	✓	✗	✗	✓
7.6	Torsethaugen	✗	✗	✓	✗	✗
7.7	Torsethaugen	✗	✓	✗	✓	✗

Table 7.1: Overview over the effects that are used in the simulation for each category.

7.1 Unidirectional Single-Peaked Waves

7.1.1 Standard Deviation

There are a total of 24 sea states to be simulated in RIFLEX. All of which yield massive information about the riser response and behaviour.

Sea state		Mean wave heading							
		0		30		60		90	
H_S	T_P	σ	ζ	σ	ζ	σ	ζ	σ	ζ
2	9	0.365	0.001	0.340	0.120	0.368	0.096	0.438	0.015
2	10	0.356	0.001	0.339	0.115	0.366	0.095	0.423	0.020
4	10	0.561	0.001	0.538	0.118	0.575	0.102	0.656	0.021
2	12	0.324	0.001	0.314	0.119	0.339	0.107	0.384	0.046
4	12	0.515	0.001	0.502	0.117	0.538	0.105	0.599	0.046
6	12	0.661	0.001	0.649	0.115	0.690	0.110	0.757	0.047

Table 7.2: Standard deviation and ratios for unidirectional single-peaked waves with different heading. σ is the standard deviation of the angle motion and ζ is the ratio between the minimum and maximum standard deviation (see section 5.3.2).

The strongest dependence is the wave height dependence. We can also see an increasing trend for the standard deviation as expected. This is not necessarily linear, but otherwise as predicted. We can also see a small dependence on the heading direction. From table 7.2 we can also see that the ratio is small for the headings 0° and 90°. The ratio are, however, never larger than 0.12. This is much lower than ratios found from the full scale measurements.

Another important observation can be found in figure 7.2. The riser angle response dies out for ω less than about 0.5 rad/s. Compared to figure 5.15 this can differ much for very low frequencies. Otherwise, there are similarities for the mid-range in the spectrum.

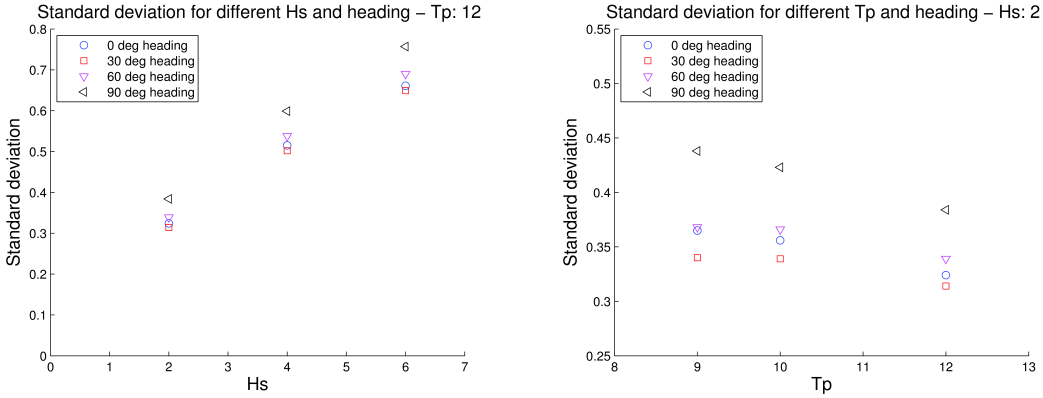

(a) Standard deviation with varying Hs, Tp: 12 s (b) Standard deviation with varying Tp, Hs: 2 m

Figure 7.1: The effect of Tp and Hs on the standard deviation

As the frequency increases above about 1.2 rad/s, both the full scale spectra and the spectrum from the RIFLEX simulations die out.

When we take a closer look at the eigenfrequencies in table 6.1 we can identify the peaks close to 0.58 rad/s and 0.84 rad/s for the 3rd and 4th mode, respectively. The relevant wave peak frequency for the spectra is 0.63 rad/s (10 s). This observation can also be made for all other spectra other than the example shown here.

7.1.2 Spectrum and Broadness

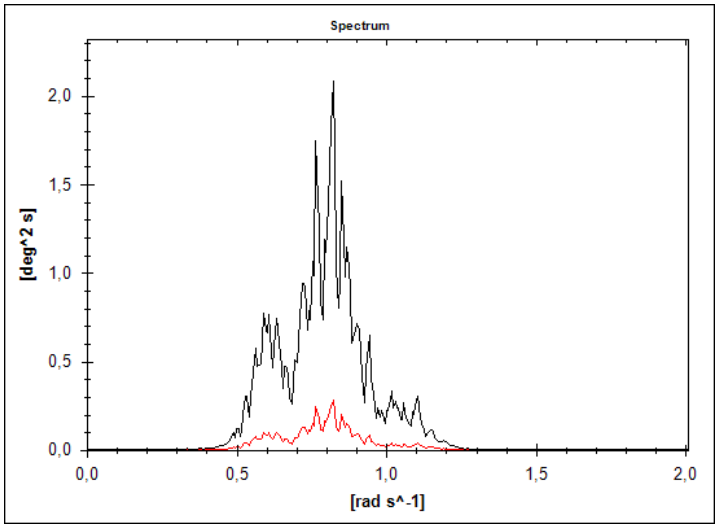

Figure 7.2: Spectra for global xz- and yz-planes. The spectra is from a simulation with $H_S = 4$ m and $T_P = 10$ s. A peak near $\omega = 0.8$ is clearly visible, which is close to the eigenfrequency in the 4th mode.

Figure 7.3 show the distribution of the broadness of the processes with the current spectra. Regardless of incoming direction, H_S or T_P, the broadness does not seem

to follow a trend. Therefore, all ϵ's are collected into one plot. All the broadness parameters are calculated from the spectra.

Sea state		Mean wave heading			
H_S	T_P	0	30	60	90
2	9	0.72	0.86	0.81	0.57
2	10	0.79	0.92	0.88	0.84
4	10	0.83	0.93	0.90	0.87
2	12	0.83	0.87	0.85	0.82
4	12	0.84	0.85	0.83	0.83
6	12	0.81	0.79	0.78	0.80

Table 7.3: Average broadness for unidirectional single-peaked spectra

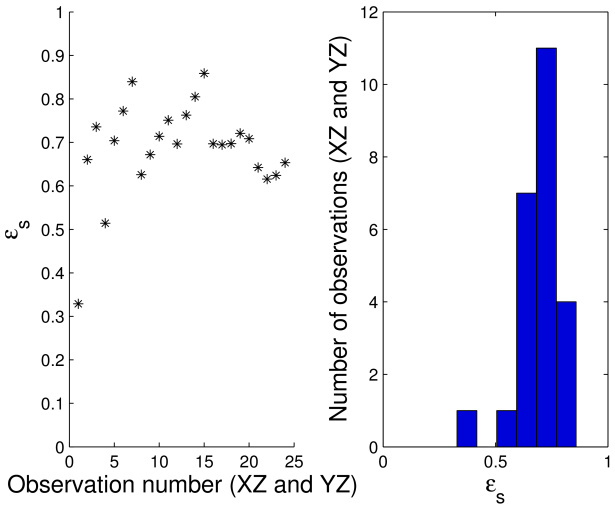

Figure 7.3: The scattering of ϵ for unidirectional single-peaked waves

7.1.3 Fatigue

Figure 7.4(a) and 7.4(b) shows the long term angle spectra for constant heading and varying heading, respectively. A Weibull curve has been fitted to the data computed by RIFLEX. The total fatigue has been found using the block method and the Miner-Palmgren formula.

The mean response direction (see figure 5.5) is very consistent relative to the mean wave direction when calculated in RIFLEX. When taking into account the different mean wave directions and accumulated fatigue, the wellhead will take most damage in the direction that line up with rig's main direction, i.e. 0°.

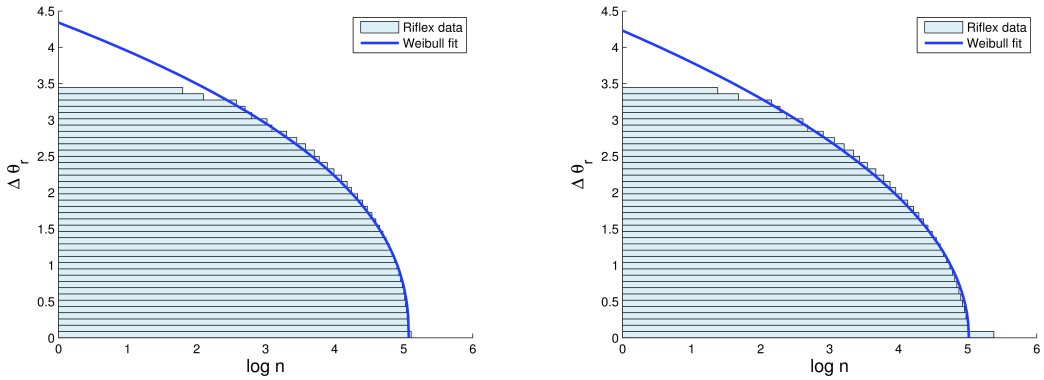

(a) Angle spectrum, constant heading (b) Angle spectrum, varying heading

Figure 7.4: Angle spectra for unidirectional single-peaked waves with different heading

No. of mean wave directions	Miner-Palmgren sum			Weibull fit			
	$\theta_{r,0}$	n_0	D	$\theta_{r,0}$	n_0	β	D
1	3.403	128432	0.011059	4.34	118744	2.33	0.011287
4	3.403	239735	0.005817	4.23	104172	2.32	0.008821

Table 7.4: Cumulative damage and values for both block method and closed form solution in unidirectional single-peaked waves.

7.1.4 Short-Term Angle Spectra

The short-term angle range spectrum in figure 7.5 is from 3 hours of simulation with similar sea state conditions as for the full scale measurements, i.e. $H_S = 4\,\text{m}$ and $T_P = 10\,\text{s}$. The spectrum has the same convex shape as the full scale spectrum for wave frequency dominated angle motion.

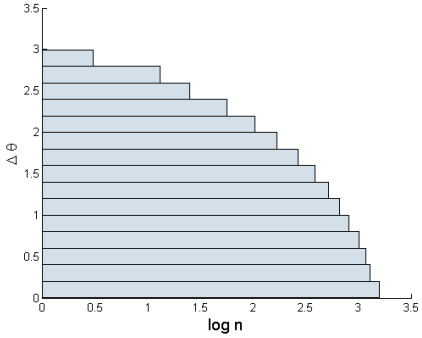

Figure 7.5: Short-term angle range spectrum for unidirectional JONSWAP waves

7.2 Unidirectional Torsethaugen Waves

7.2.1 Standard Deviation

There are a total of 24 sea states to be simulated in RIFLEX. All of which yield massive information about the riser response and behaviour.

Sea state		Mean wave heading							
		0		30		60		90	
H_S	T_P	σ	ζ	σ	ζ	σ	ζ	σ	ζ
2	9	0.356	0.001	0.332	0.116	0.360	0.100	0.426	0.016
2	10	0.347	0.001	0.334	0.110	0.359	0.098	0.409	0.021
4	10	0.561	0.001	0.540	0.116	0.577	0.104	0.652	0.022
2	12	0.320	0.001	0.309	0.127	0.334	0.110	0.381	0.040
4	12	0.510	0.001	0.499	0.122	0.535	0.111	0.592	0.047
6	12	0.667	0.001	0.656	0.118	0.698	0.111	0.762	0.049

Table 7.5: Standard deviation and ratios for unidirectional Torsethaugen waves with different heading. σ is the standard deviation of the angle motion and ζ is the ratio between the minimum and maximum standard deviation (see section 5.3.2).

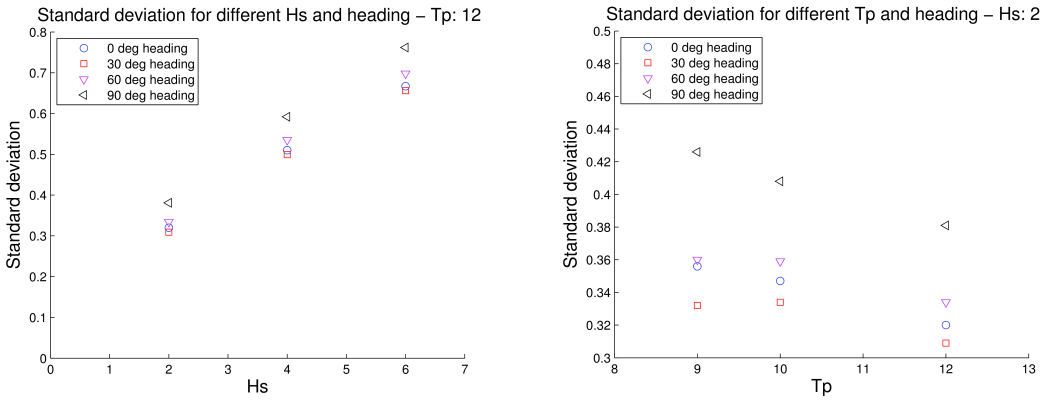

(a) Standard deviation with varying Hs, Tp: 12 s (b) Standard deviation with varying Tp, Hs: 2 m

Figure 7.6: The effect of Tp and Hs on the standard deviation (Torsethaugen spectrum)

The trends are also the same as for the JONSWAP spectra. The ratios are still extremely low, but having a unidirectional wave spectrum this is still expected. The standard deviations have not changed much. The change between the standard deviations between a pure JONSWAP wave spectrum and a Torsethaugen wave spectrum vary from -3 % to +3 % and does not follow any system regarding significant wave height or the peak period. On an average it becomes very small, i.e. below 1 %.

7.2.2 Spectrum and Broadness

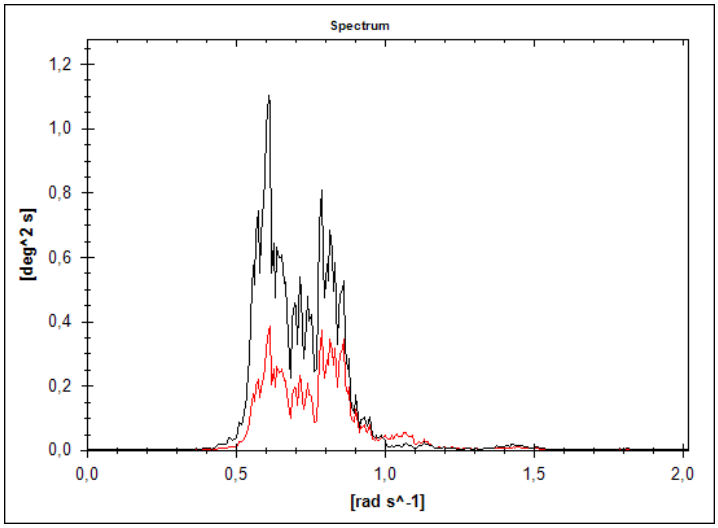

Figure 7.7: Spectra for global xz- and yz-planes for unidirectional Torsethaugen waves. The spectra is from a simulation with $H_S = 4$ m and $T_P = 10$ s. Two peaks near $\omega = 0.6$ and $\omega = 0.8$ are clearly visible, which is close to the eigenfrequency in the 3rd and 4th mode.

The spectrum now has two more distinct peaks. Figure 7.8 show the distribution of the broadness of the processes with the current spectra. From table 7.6 it now seems that we have a small reduction of ϵ at $T_P = 12\,\text{s}$, which is true for all directions and H_S. From the other variables, it still seems random with no clear trend.

Sea state		Mean wave heading			
H_S	T_P	0	30	60	90
2	9	0.92	0.97	0.96	0.88
2	10	0.87	0.86	0.84	0.88
4	10	0.93	0.94	0.92	0.93
2	12	0.67	0.83	0.69	0.70
4	12	0.67	0.63	0.70	0.56
6	12	0.75	0.73	0.83	0.69

Table 7.6: Average broadness for unidirectional Torsethaugen spectra

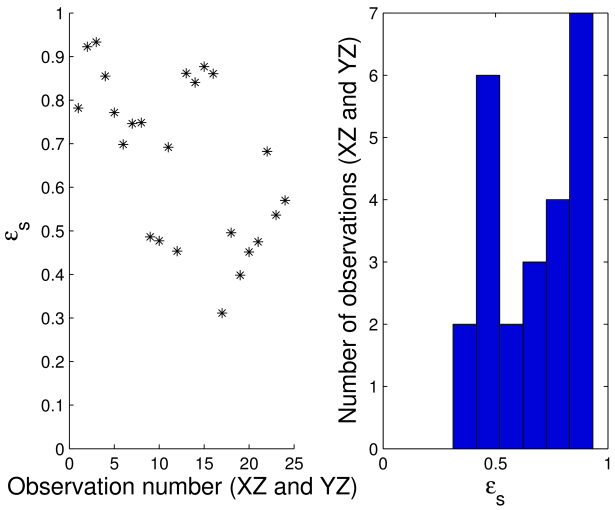

Figure 7.8: The scattering of ϵ for unidirectional Torsethaugen waves

7.2.3 Fatigue

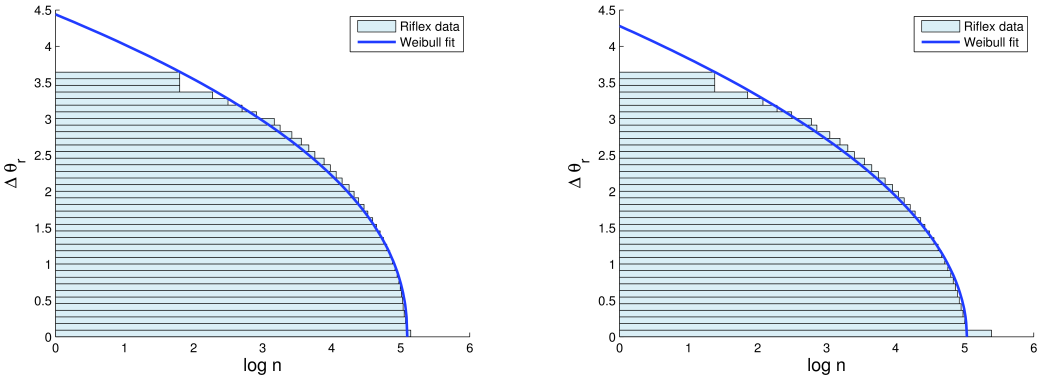

(a) Angle spectrum, constant heading

(b) Angle spectrum, varying heading

Figure 7.9: Angle spectra for unidirectional Torsethaugen waves with different heading

Figure 7.9(a) and 7.9(b) shows the long term angle spectra for constant heading and varying heading, respectively. A Weibull curve has been fitted to the data computed by RIFLEX. The total fatigue has been found using the block method and the Miner-Palmgren formula.

The mean response direction (see figure 5.5) is very consistent relative to the mean wave direction when calculated in RIFLEX. When taking into account the different mean wave directions and accumulated fatigue, the wellhead will take most damage in the direction that line up with rig's main direction, i.e. 0°.

No. of mean wave directions	Miner-Palmgren sum $\theta_{r,0}$	n_0	D	Weibull fit $\theta_{r,0}$	n_0	β	D
1	3.599	140129	0.011518	4.44	124365	2.22	0.011195
4	3.599	244302	0.006047	4.28	107666	2.00	0.005880

Table 7.7: Cumulative damage and values for both block method and closed form solution in unidirectional Torsethaugen waves.

7.2.4 Short-Term Angle Spectra

The short-term angle range spectrum in figure 7.10 is from 3 hours of simulation with similar sea state conditions as for the full scale measurements, i.e. $H_S = 4\,\text{m}$ and $T_P = 10\,\text{s}$. The spectrum has the same convex shape as the full scale spectrum for wave frequency dominated angle motion.

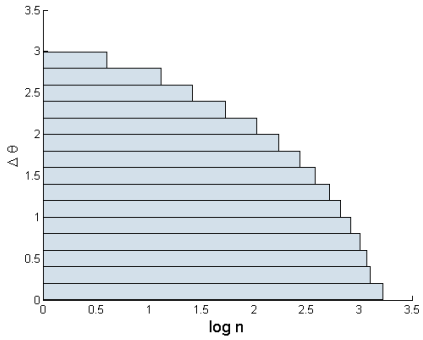

Figure 7.10: Short-term angle range spectrum for unidirectional Torsethaugen waves

7.3 Unidirectional Torsethaugen Waves with Non-Linear Boundary Conditions

7.3.1 Standard Deviation

When there is a change in the boundary conditions this close to the point of interest we would expect some degree of influence on the results. The initial stiffness is much higher and does not reach the same tangential stiffness until ~3°, which is rarely reached (see section 6.6.2.

As for the two other unidirectional simulations the ratios are relatively small. It is still unchanged and behaves in a consistent manner. Now that the non-linear spring is introduced instead of the linear one the standard deviations are reduced. On average they have been reduced with 13.6 %. The reduction is fairly consistent for all cases.

Sea state		Mean wave heading							
		0		30		60		90	
H_S	T_P	σ	ζ	σ	ζ	σ	ζ	σ	ζ
2	9	0.313	0.001	0.291	0.116	0.316	0.102	0.377	0.016
2	10	0.306	0.001	0.293	0.112	0.316	0.102	0.361	0.020
4	10	0.498	0.001	0.477	0.116	0.511	0.105	0.583	0.021
2	12	0.280	0.001	0.267	0.127	0.290	0.113	0.334	0.037
4	12	0.448	0.001	0.436	0.122	0.469	0.111	0.524	0.044
6	12	0.592	0.001	0.579	0.116	0.617	0.110	0.681	0.045

Table 7.8: Standard deviation and ratios for unidirectional Torsethaugen waves with different heading and implemented non-linear boundary condition. σ is the standard deviation of the angle motion and ζ is the ratio between the minimum and maximum standard deviation (see section 5.3.2).

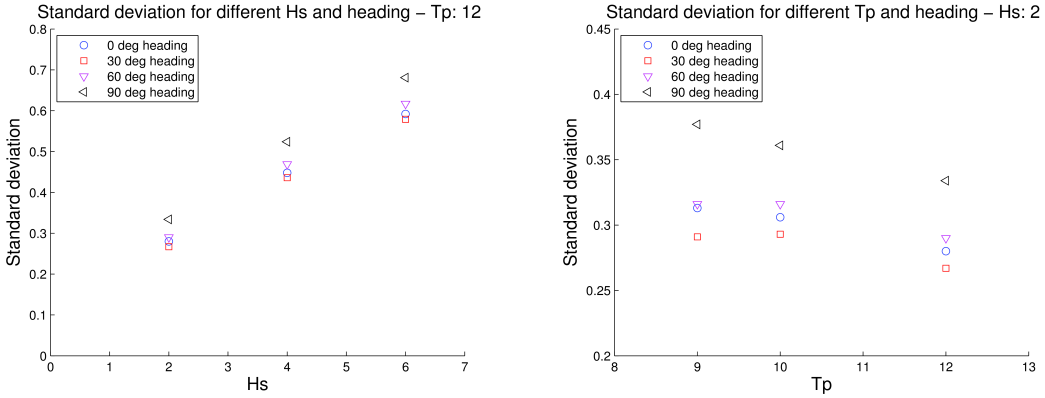

(a) Standard deviation with varying Hs, Tp: 12 s (b) Standard deviation with varying Tp, Hs: 2 m

Figure 7.11: The effect of Tp and Hs on the standard deviation (Torsethaugen spectrum, non-linear boundary condition)

7.3.2 Spectrum and Broadness

With the exact same sea state but with different boundary conditions, the sea states with $T_P = 12\,\text{s}$ yields a lower ϵ of the spectra.

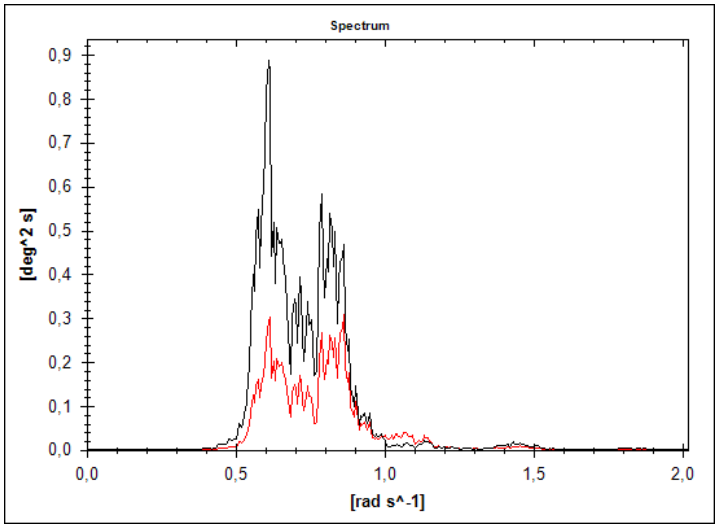

Figure 7.12: Spectra for global xz- and yz-planes for Torsethaugen waves with non-linear boundary conditions. The spectra is from a simulation with $H_S = 4$ m and $T_P = 10$ s. Two peaks near $\omega = 0.6$ and $\omega = 0.8$ are clearly visible, which is close to the eigenfrequency in the 3rd and 4th mode.

Sea state		Mean wave heading			
H_S	T_P	0	30	60	90
2	9	0.90	0.96	0.95	0.83
2	10	0.88	0.91	0.88	0.89
4	10	0.92	0.94	0.92	0.92
2	12	0.66	0.79	0.67	0.60
4	12	0.71	0.67	0.71	0.61
6	12	0.75	0.65	0.78	0.69

Table 7.9: Average broadness for unidirectional Torsethaugen spectra and non-linear boundary condition

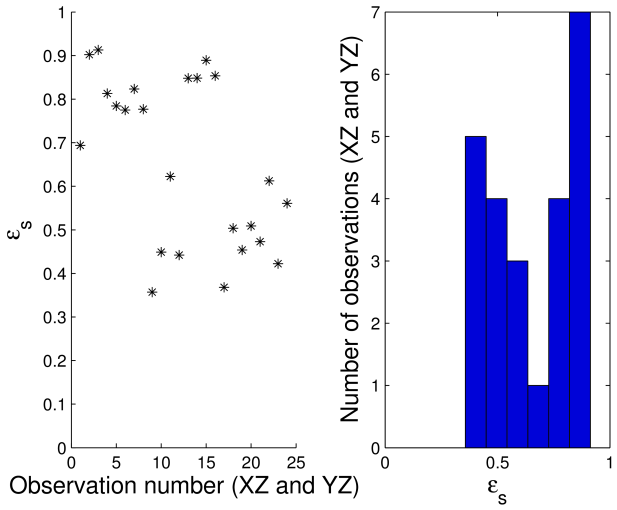

Figure 7.13: The scattering of ϵ for unidirectional Torsethaugen waves and non-linear boundary condition

7.3.3 Fatigue

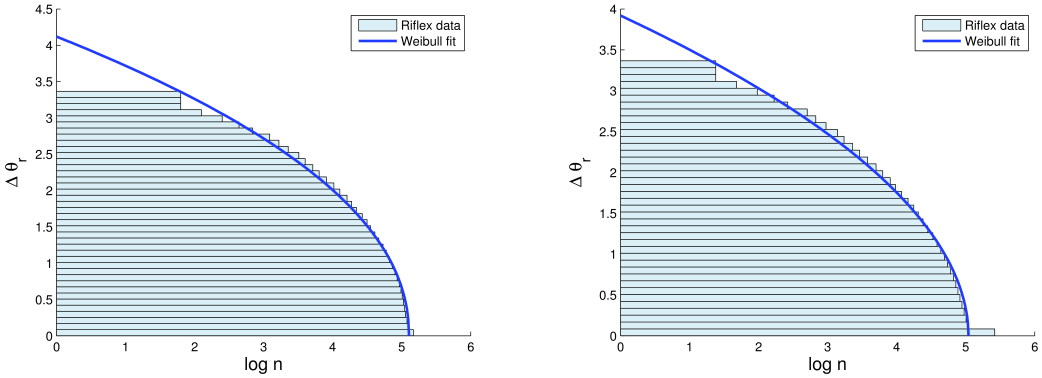

(a) Angle spectrum, constant heading

(b) Angle spectrum, varying heading

Figure 7.14: Angle spectra for unidirectional Torsethaugen waves with different heading and non-linear boundary conditions

Figure 7.14(a) and 7.14(b) shows the long term angle spectra for constant heading and varying heading, respectively. A Weibull curve has been fitted to the data computed by RIFLEX. The total fatigue has been found using the block method and the Miner-Palmgren formula.

The mean response direction (see figure 5.5) is very consistent relative to the mean wave direction when calculated in RIFLEX. When taking into account the different mean wave directions and accumulated fatigue, the wellhead will take most damage in the direction that line up with rig's main direction, i.e. 0°.

No. of mean	Miner-Palmgren sum			Weibull fit			
wave directions	$\theta_{r,0}$	n_0	D	$\theta_{r,0}$	n_0	β	D
1	3.324	148329	0.007131	4.12	127519	2.13	0.006919
4	3.324	263829	0.003713	3.92	109983	1.96	0.003651

Table 7.10: Cumulative damage and values for both block method and closed form solution in unidirectional Torsethaugen waves and non-linear boundary conditions.

7.3.4 Short-Term Angle Spectra

The short-term angle range spectrum in figure 7.15 is from 3 hours of simulation with similar sea state conditions as for the full scale measurements, i.e. $H_S = 4\,\text{m}$ and $T_P = 10\,\text{s}$. The spectrum has the same convex shape as the full scale spectrum for wave frequency dominated angle motion.

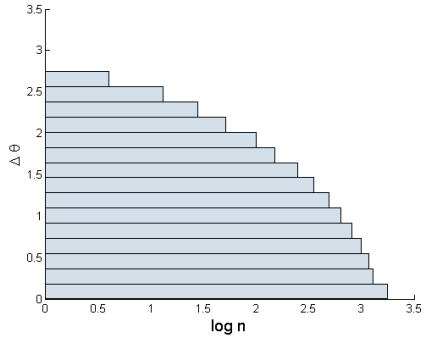

Figure 7.15: Short-term angle range spectrum for unidirectional Torsethaugen waves with non-linear flex joint

7.4 Torsethaugen Waves with Wave Spreading

7.4.1 Standard Deviation

When the wave energy is spread around a mean wave direction some of the energy will consequently be used to excite the other d.o.f.'s of the structure. Though it is not a similar structure it shows that we can expect a reduction.

Sea state		Mean wave heading							
		0		30		60		90	
H_S	T_P	σ	ζ	σ	ζ	σ	ζ	σ	ζ
2	9	0.313	0.566	0.286	0.742	0.317	0.561	0.335	0.447
2	10	0.304	0.594	0.285	0.734	0.313	0.573	0.330	0.471
4	10	0.506	0.502	0.478	0.612	0.525	0.478	0.556	0.379
2	12	0.279	0.619	0.263	0.742	0.291	0.572	0.307	0.472
4	12	0.457	0.529	0.442	0.600	0.484	0.471	0.510	0.392
6	12	0.609	0.471	0.592	0.528	0.642	0.417	0.676	0.348

Table 7.11: Standard deviation and ratios for Torsethaugen waves with spreading. σ is the standard deviation of the angle motion and ζ is the ratio between the minimum and maximum standard deviation (see section 5.3.2).

The standard deviations have become lower and the ratios have reached more realistic values. The biggest reduction can be found for the lowest H_S where the reduction relative to a unidirectional Torsethaugen spectrum on average is about 17 %. For the tallest waves where the waves are more concentrated along the mean direction the reduction is only at about 10 %.

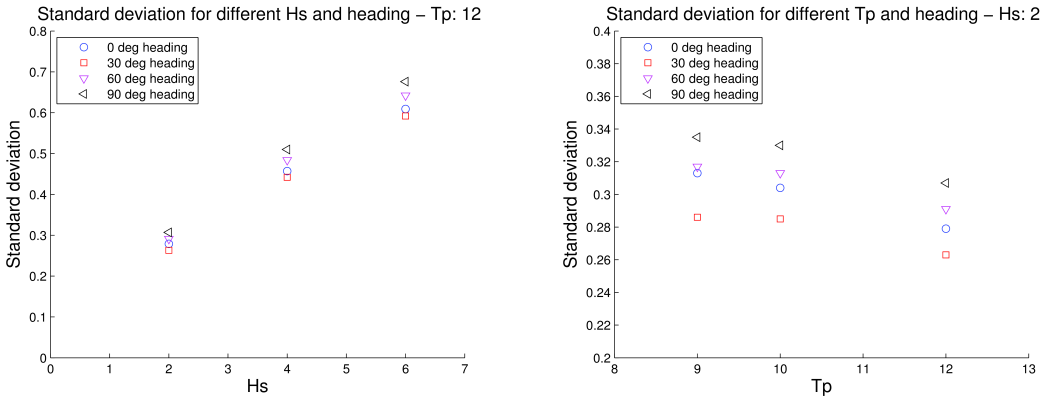

(a) Standard deviation with varying Hs, Tp: 12 s (b) Standard deviation with varying Tp, Hs: 2 m

Figure 7.16: The effect of Tp and Hs on the standard deviation (Torsethaugen spectrum with wave spreading)

7.4.2 Spectrum and Broadness

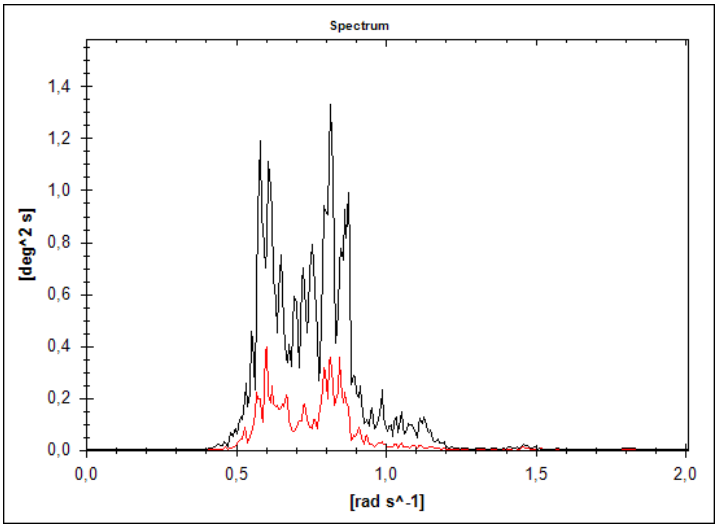

Figure 7.17: Spectra for global xz- and yz-planes for Torsethaugen waves with directional spreading. The spectra is from a simulation with $H_S = 4$ m and $T_P = 10$ s. Two peaks near $\omega = 0.6$ and $\omega = 0.8$ are clearly visible, which is close to the eigenfrequency in the 3rd and 4th mode.

Sea state		Mean wave heading			
H_S	T_P	0	30	60	90
2	9	0.80	0.96	0.98	0.98
2	10	0.96	0.95	0.94	0.75
4	10	0.92	0.94	0.92	0.84
2	12	0.92	0.88	0.83	0.64
4	12	0.93	0.88	0.80	0.64
6	12	0.93	0.89	0.80	0.70

Table 7.12: Average broadness for unidirectional Torsethaugen spectra with wave spreading

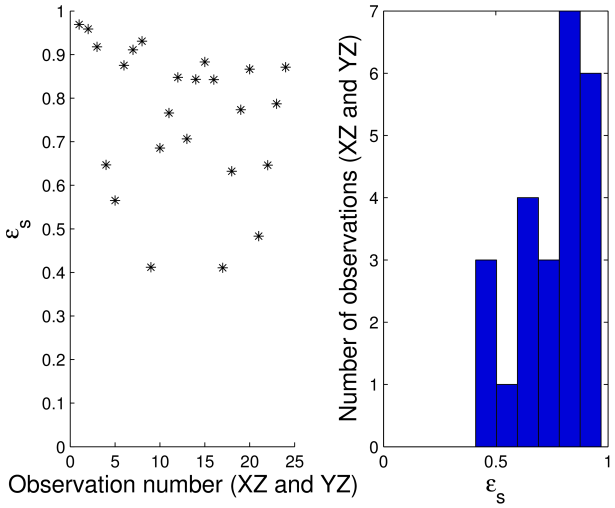

Figure 7.18: The scattering of ϵ for unidirectional Torsethaugen waves with wave spreading

7.4.3 Fatigue

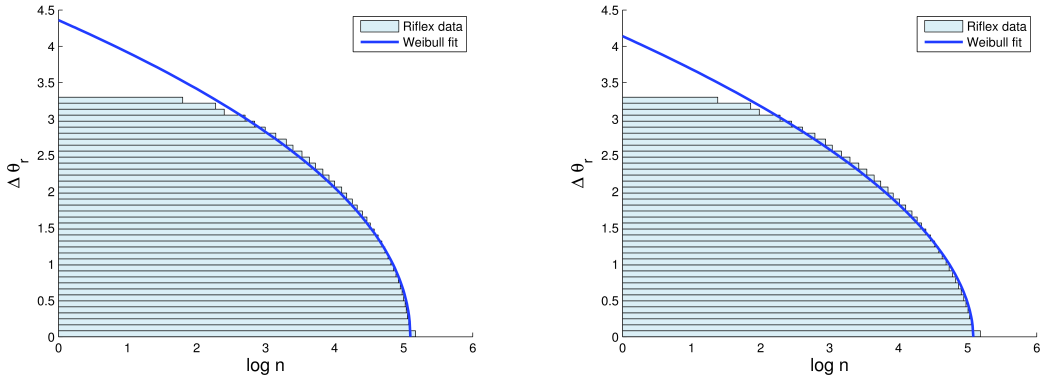

(a) Angle spectrum, constant heading

(b) Angle spectrum, varying heading

Figure 7.19: Angle spectra for unidirectional Torsethaugen waves with different heading and wave spreading

Figure 7.19(a) and 7.19(b) shows the long term angle spectra for constant heading and varying heading, respectively. A Weibull curve has been fitted to the data computed by RIFLEX. The total fatigue has been found using the block method and the Miner-Palmgren formula.

The mean response direction (see figure 5.5) is very consistent relative to the mean wave direction when calculated in RIFLEX. When taking into account the different mean wave directions and accumulated fatigue, the wellhead will take most damage in the direction that line up with rig's main direction, i.e. 0°.

No. of mean	Miner-Palmgren sum			Weibull fit			
wave directions	$\theta_{r,0}$	n_0	D	$\theta_{r,0}$	n_0	β	D
1	3.258	148505	0.007779	4.36	124981	2.04	0.007748
4	3.258	152904	0.004495	4.14	120604	1.89	0.004502

Table 7.13: Cumulative damage and values for both block method and closed form solution in unidirectional Torsethaugen waves and wave spreading.

7.4.4 Short-Term Angle Spectra

The short-term angle range spectrum in figure 7.20 is from 3 hours of simulation with similar sea state conditions as for the full scale measurements, i.e. $H_S = 4\,\text{m}$ and $T_P = 10\,\text{s}$. The spectrum has the same convex shape as the full scale spectrum for wave frequency dominated angle motion.

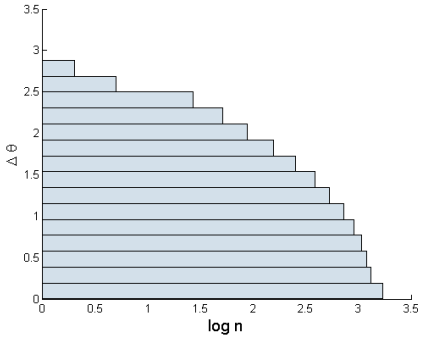

Figure 7.20: Short-term angle range spectrum for Torsethaugen waves with wave spreading

7.5 Torsethaugen Waves with Non-Linear Boundary Conditions and Wave Spreading

7.5.1 Standard Deviation

We now have a situation where we have distributed the energy from different direction through wave spreading and a non-linear spring. We have shown that these factors will both reduce the response of the angle. Combined, they will contribute to an even larger reduction of the standard deviation.

Sea state		Mean wave heading							
		0		30		60		90	
H_S	T_P	σ	ζ	σ	ζ	σ	ζ	σ	ζ
2	9	0.276	0.565	0.251	0.752	0.279	0.567	0.294	0.450
2	10	0.268	0.595	0.250	0.743	0.276	0.578	0.291	0.475
4	10	0.449	0.499	0.423	0.614	0.465	0.477	0.494	0.377
2	12	0.245	0.605	0.228	0.744	0.253	0.571	0.268	0.465
4	12	0.402	0.519	0.386	0.599	0.424	0.468	0.448	0.384
6	12	0.540	0.463	0.522	0.524	0.569	0.413	0.601	0.341

Table 7.14: Standard deviation and ratios for unidirectional Torsethaugen waves with wave spreading and implemented non-linear boundary condition. σ is the standard deviation of the angle motion and ζ is the ratio between the minimum and maximum standard deviation (see section 5.3.2).

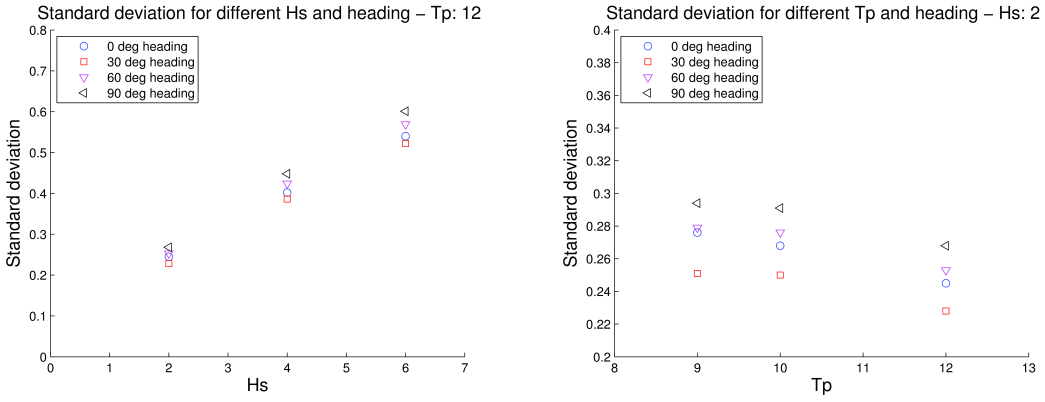

(a) Standard deviation with varying Hs, Tp: 12 s (b) Standard deviation with varying Tp, Hs: 2 m

Figure 7.21: The effect of Tp and Hs on the standard deviation (Torsethaugen spectrum with wave spreading and non-linear boundary condition)

7.5.2 Spectrum and Broadness

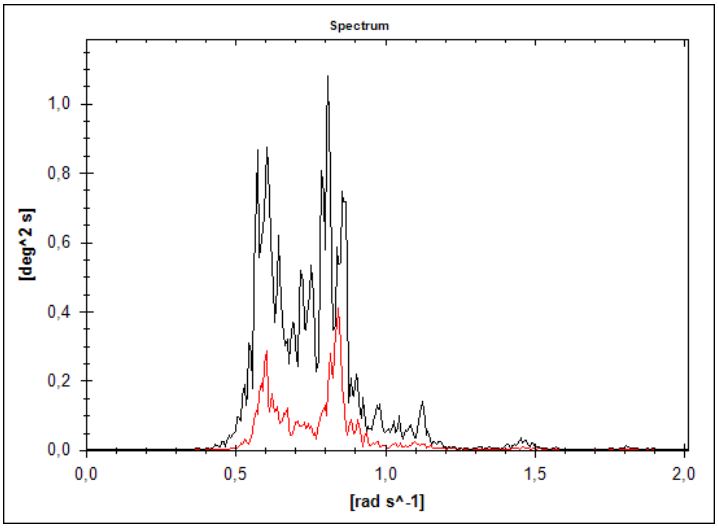

Figure 7.22: Spectra for global xz- and yz-planes for Torsethaugen waves with directional spreading and non-linear flex joint. The spectra is from a simulation with $H_S = 4$ m and $T_P = 10$ s. Two peaks near $\omega = 0.6$ and $\omega = 0.8$ are clearly visible, which is close to the eigenfrequency in the 3rd and 4th mode.

Sea state		Mean wave heading			
H_S	T_P	0	30	60	90
2	9	0.84	0.96	0.98	0.98
2	10	0.96	0.93	0.89	0.67
4	10	0.92	0.93	0.89	0.72
2	12	0.85	0.70	0.69	0.84
4	12	0.85	0.69	0.69	0.77
6	12	0.85	0.67	0.61	0.63

Table 7.15: Average broadness for Torsethaugen spectra with wave spreading and non-linear boundary condition

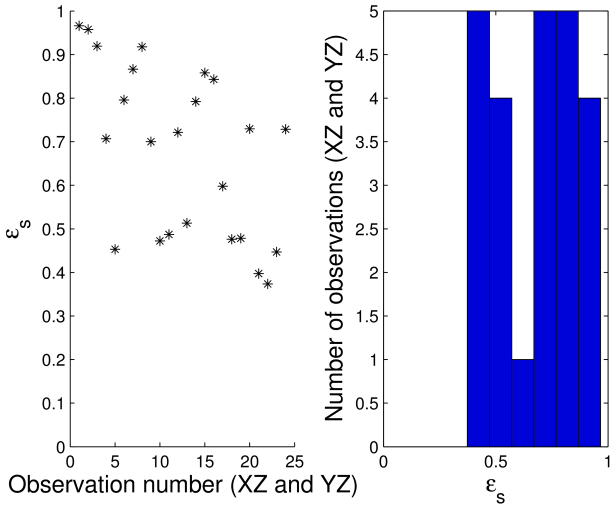

Figure 7.23: The scattering of ϵ for Torsethaugen waves and non-linear boundary condition

7.5.3 Fatigue

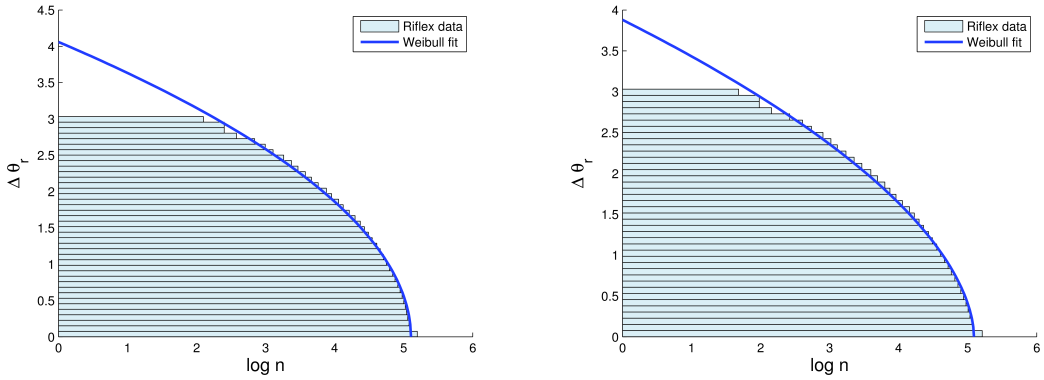

(a) Angle spectrum, constant heading

(b) Angle spectrum, varying heading

Figure 7.24: Angle spectra for unidirectional Torsethaugen waves with different heading, wave spreading and non-linear boundary conditions

Figure 7.24(a) and 7.24(b) shows the long term angle spectra for constant heading and varying heading, respectively. A Weibull curve has been fitted to the data computed by RIFLEX. The total fatigue has been found using the block method and the Miner-Palmgren formula.

The mean response direction (see figure 5.5) is very consistent relative to the mean wave direction when calculated in RIFLEX. When taking into account the different mean wave directions and accumulated fatigue, the wellhead will take most damage in the direction that line up with rig's main direction, i.e. 0°.

No. of mean	Miner-Palmgren sum			Weibull fit			
wave directions	$\theta_{r,0}$	n_0	D	$\theta_{r,0}$	n_0	β	D
1	2.994	157377	0.004778	4.06	127527	1.96	0.004859
4	2.994	162279	0.002719	3.88	123459	1.79	0.002770

Table 7.16: Cumulative damage and values for both block method and closed form solution in unidirectional Torsethaugen waves, wave spreading and non-linear boundary conditions.

7.5.4 Short-Term Angle Spectra

The short-term angle range spectrum in figure 7.25 is from 3 hours of simulation with similar sea state conditions as for the full scale measurements, i.e. $H_S = 4\,\text{m}$ and $T_P = 10\,\text{s}$. The spectrum has the same convex shape as the full scale spectrum for wave frequency dominated angle motion.

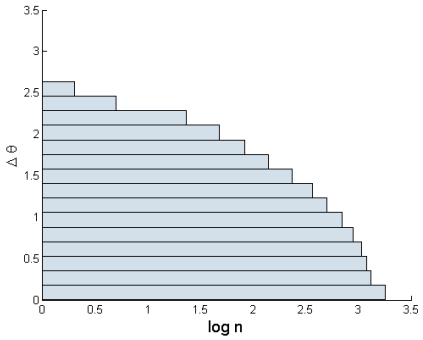

Figure 7.25: Short-term angle range spectrum for Torsethaugen waves with non-linear flex joint and wave spreading

7.6 Unidirectional Torsethaugen Waves with Current

7.6.1 Standard Deviation

This simulation was run to find any influence the presence of a current has on the standard deviation. The results are listed in table 7.17. The current dependency is very strong and is visible also for low current velocities. The mean wave direction in all simulations are 0°.

In a steady current the total structure will have a static configuration if we neglect the effects of vortex shedding. The rig is moored by anchors and will consequently have a static offset position. A support vessel is only described with a linear transfer function in RIFLEX. The amplitude and phase relative to the excitation force is given for all 6

Current	Heading			
	0°		90°	
$V[m/s]$	σ	ζ	σ	ζ
0	0.561	0.001	0.561	0.001
0.14	0.536	0.001	0.546	0.077
0.28	0.461	0.001	0.506	0.106
0.42	0.357	0.001	0.458	0.115
0.56	0.262	0.001	0.406	0.114
0.70	0.194	0.002	0.356	0.109
0.84	0.148	0.002	0.311	0.102

Table 7.17: Standard deviation and ratios for unidirectional Torsethaugen waves with current, Hs 4 m Tp 10 s. σ is the standard deviation of the angle motion and ζ is the ratio between the minimum and maximum standard deviation (see section 5.3.2).

d.o.f.'s for the support vessel. Figure 7.27(a) and 7.27(b) shows the static configuration of the marine riser and how the support vessel is unaffected by it.

Without the values for the drag forces of the support vessel in different directions and the characteristics of the mooring system it is impossible to determine how much the offset would be. However, one could argue that it would affect the static angle of the riser at the bottom even more than the forces acting on the riser alone does. According to figure 6.7 this would yield a lower tangential stiffness on the spring simulating the flex joint which in turn would increase the motion and the standard deviation of the angular motion.

The rig's transfer function are also affected. They are based on the tangential stiffness from the mooring system. An offset of the equilibrium position will increase the mooring system's tangential stiffness. Without the characteristics it is, again, impossible to determine the importance of this effect.

Regardless of the two mentioned issues above the presence of a current will affect the outcome of the standard deviation and should be accounted for.

7.6.2 Spectrum and Broadness

The spectrum is very different from the previous simulation spectra. Instead of two very distinct peaks, the spectrum in figure 7.28 has one wide peak distributed over a wide range of frequencies. It also has some energy in the low frequency range, though it is very low.

For the very first case, where there is no current present, we get the same value for the broadness. Once any current is present it changes a little, but stays at a relatively constant value for all current strengths in both directions.

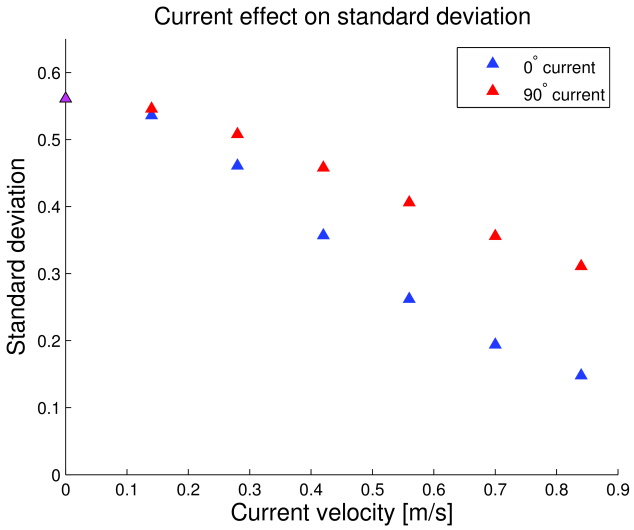

Figure 7.26: Effect of current on standard deviation. The current heading is relative to the rig's local x axis. A current from the side of the rig yields less damping of the angle response.

Current	Heading	
$V[m/s]$	0	90
0	0.93	0.93
0.14	0.88	0.86
0.28	0.87	0.87
0.42	0.88	0.88
0.56	0.88	0.89
0.70	0.87	0.89
0.84	0.86	0.89

Table 7.18: Average broadness for unidirectional Torsethaugen spectra with current

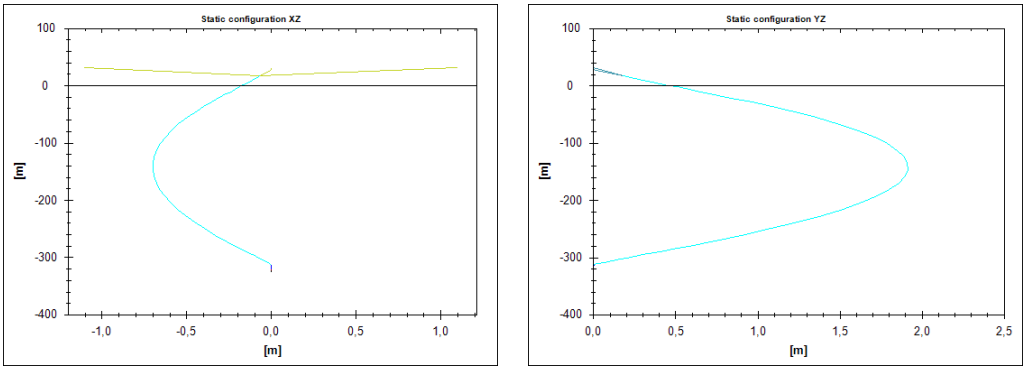

(a) Static global xz configuration (b) Static global yz configuration

Figure 7.27: Static configuration of marine riser in current velocity of 0.56 m/s. The current is headed in the rig's local x direction, and the plot is plotted with respect to global xz and yz planes.

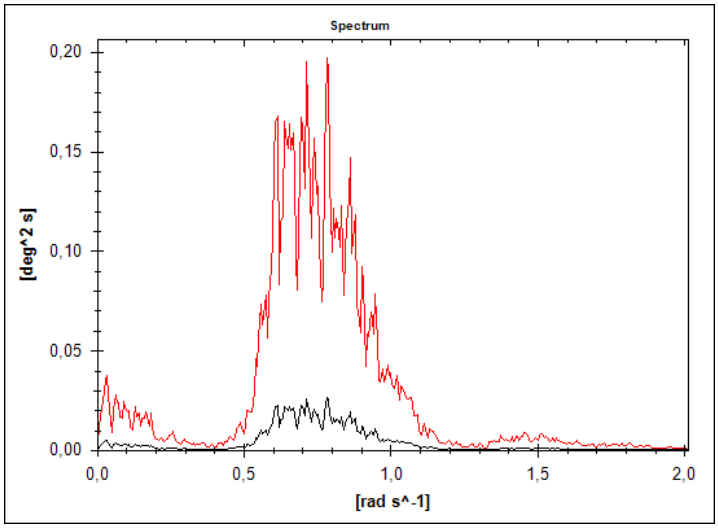

Figure 7.28: Spectra for global xz- and yz-planes for unidirectional Torsethaugen waves with non-linear boundary conditions. The spectra is from a simulation with $H_S = 4$ m and $T_P = 10$ s.

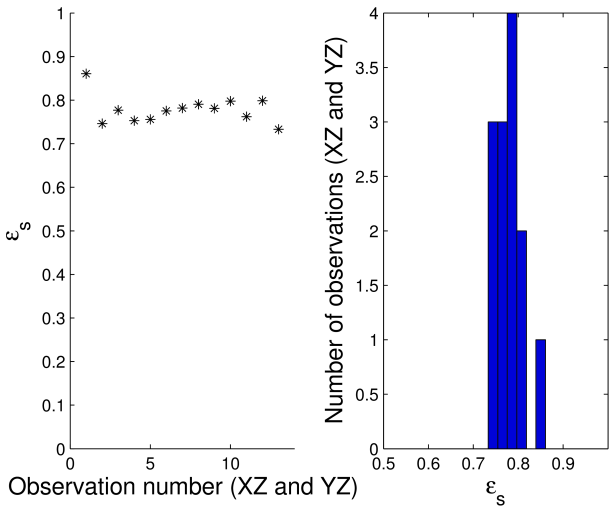

Figure 7.29: The scattering of ϵ for unidirectional Torsethaugen waves with current

7.6.3 Short-Term Angle Spectra

The results in figure 7.30 shows how the current affects the characteristics of the angle range spectrum. For low current velocities the maximum range $\Delta\theta_0$ is higher than for current velocities that are higher. In section 7.6.1 we found that the current will reduce the standard deviation of the angle motion. The effect is also positive when we look at the shape. The shape becomes similar to the full scale measurements which may indicate that the current is a very important parameter. There are practically no change in total number of cycles which means that the higher amplitudes are reduced significantly.

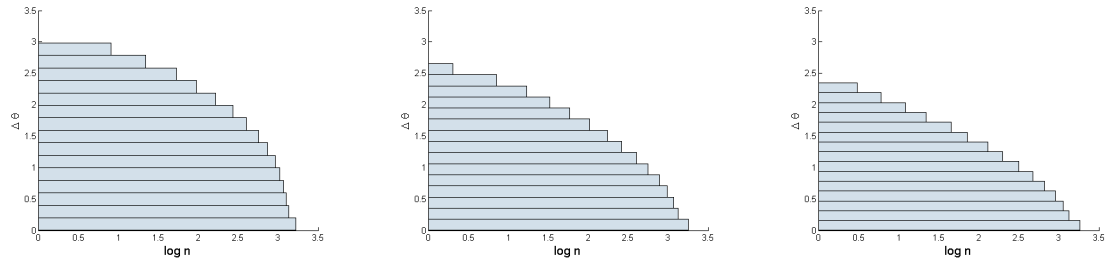

(a) Low current, ~0.2–0.3 m/s (b) Medium current, ~0.4–0.5 m/s (c) High current, ~0.6–0.7 m/s

Figure 7.30: Current effect on the short-term angle range spectra. For increasing currents the spectrum becomes more similar to the shape of the full scale angle spectrum.

7.7 Unidirectional Torsethaugen Waves with Non-Linear Boundary Conditions and Rig Offset

7.7.1 Standard Deviation

Instead of a decrease in the standard deviation of the response there is an increase. Since the mean angle is at an angle which is not zero we get a tangential stiffness that is lower. Figure 7.32 shows how the response is affected for different offset values both when the offset is in-line with the incoming waves and when it is perpendicular.

Figure 7.31 shows the difference between the calculated LFJ angle when it was found with the Excel sheet (Appendix A) and the angles found by RIFLEX. The blue line indicates the LFJ angle for the relevant offset and is unaffected to direction, i.e. x- and y-offset yields the same angle at them bottom. It is close to linear, but has a slight non-linear dependency. A few effects play a role here. The flex joint is non-linear with a smaller tangential stiffness for higher angles. The offset of the rig will give a offset vertical force which in a global free body diagram will give a moment in the opposite direction. This will in counteract the non-linearities of the flex joint.

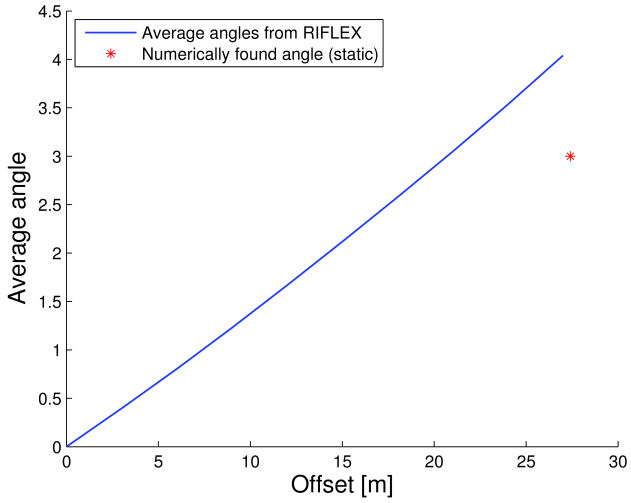

Figure 7.31: Angles for LFJ for vessel offset. The blue line is the average angle position of the riser. The red point is the static angle found from the calculations from the Excel sheet (See appendix A).

All the simulations were made in the same sea state with $H_S = 4\,\text{m}$ and $T_P = 10\,\text{s}$ and the standard deviations are listed in table 7.19. Near the zero offset point the standard deviation decreases a bit faster. This may be a result of shifting eigenfrequencies in the system due to the change in tangential stiffness.

Offset [m]	σ	
	x	y
0	0.498	
3	0.505	0.502
6	0.522	0.510
9	0.537	0.518
12	0.546	0.524
15	0.552	0.529
18	0.559	0.533
21	0.568	0.537
24	0.581	0.542
27	0.596	0.547

Table 7.19: Standard deviation for unidirectional Torsethaugen waves and non-linear boundary condition and support vessel offset, $H_S = 4$ and $T_P = 10$. σ is the standard deviation of the angle motion.

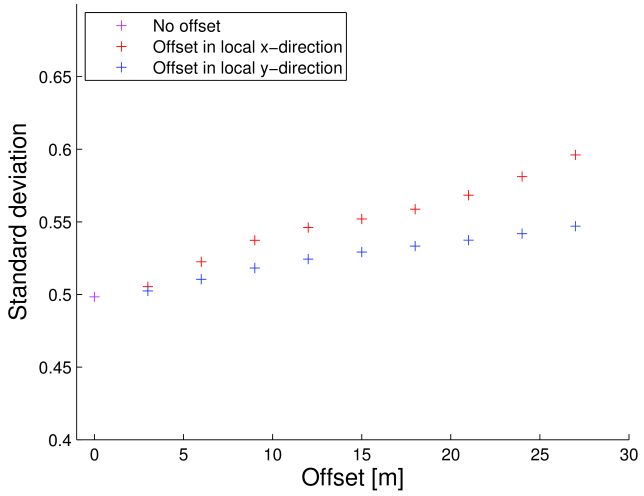

Figure 7.32: Standard deviation for support vessel offset. The local x axis is in the same heading direction as the rig.

7.7.2 Spectrum and Broadness

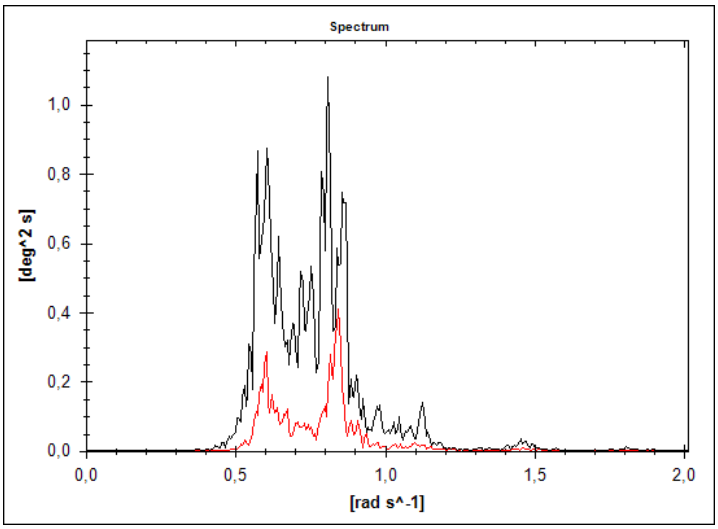

Figure 7.33: Spectra for global xz- and yz-planes for unidirectional Torsethaugen waves with support vessel offset. The spectra is from a simulation with $H_S = 4$ m, $T_P = 10$ s and an offset of 18 m in the vessel local x axis.

Offset [m]	ϵ	
	x	y
0	0.92	
3	0.94	0.92
6	0.93	0.92
9	0.93	0.92
12	0.89	0.93
15	0.77	0.93
18	0.68	0.93
21	0.70	0.93
24	0.60	0.93
27	0.69	0.93

Table 7.20: Average broadness for unidirectional Torsethaugen spectra with offset

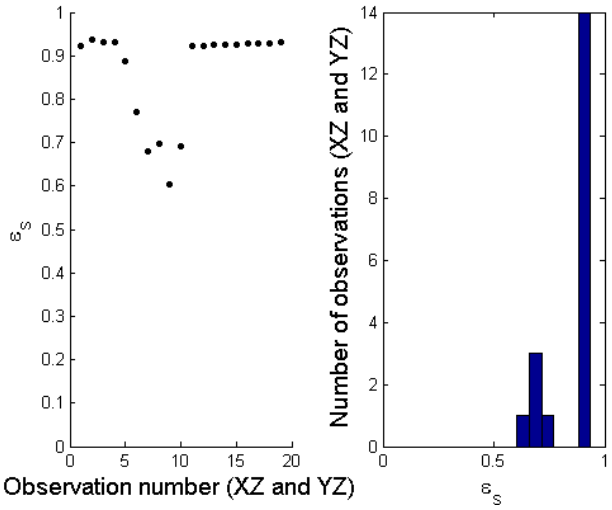

Figure 7.34: The scattering of ϵ for unidirectional Torsethaugen waves with offset

7.7.3 Short-Term Angle Spectra

When the rig is out of the equilibrium position with its mooring system the marine riser will have a mean angle different that 0. The slope of the angle range spectrum in figure 7.35 near $n = n_0$ is very steep. This means that there are very few number of cycles with low ranges.

The maximum range $\Delta\theta_0$ in subfigure 7.35(b) is also higher than in subfigure 7.35(a) which is in accordance with the increasing standard deviation for increasing offset of the rig.

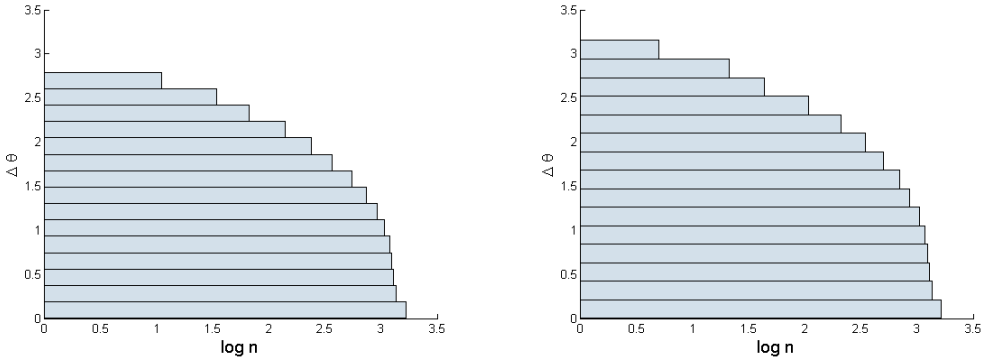

(a) Support vessel offset: ~6–9 m (b) Support vessel offset: ~15–18 m

Figure 7.35: Support vessel offset effect on the angle range spectrum.

Chapter 8

Result Comparison and Discussion

8.1 Response Comparison

As mentioned in section 3.1.2 we can find the cumulative fatigue damage if we assume a narrow band Gaussian process with the standard deviation of the angular motion and its frequency. For a broad band process we must use a correction factor which is based on the broadness parameter ϵ.

In this part of the comparison we will not compare the result with respect to fatigue, but by comparing the standard deviations directly. The full scale calculations have shown that there is little or no correlation between the mean wave direction and the mean (or *principal*) response direction. The results from RIFLEX were more consistent regarding the mean wave direction and response direction and will be presented accordingly.

In the complete data set of the angle response there was a total of 1180 hours of data. After selecting the sea states that should be compared with RIFLEX simulations we were left with only 264 hours of data. The remaining hours of data were selected based on hindcast calculations from the Norwegian Reanalysis project (NORA10) and not based on actual weather readouts on-site.

8.1.1 Standard Deviation Comparison

All the standard deviations were found using the statistical technique described in section 5.3 based on the principal axes found using the covariance method described in section 3.1.2.

The difference in the angle response by changing the wave spectra from JONSWAP to Torsethaugen spectra did not affect the results very much. When we introduced non-linear behaviour in the lower flex joint we see a clear reduction of the response for all cases and the reduction is consistent for all wave heading directions. For the case when the waves were short-crested we also see a clear reduction. The difference is when the

waves have a 90° heading. The reduction compared to the case for a non-linear flex joint is larger.

Since most of the sea states have an heading of ±30° and we should put most effort to narrow the gap in difference in this region. For the sea state in figure 8.1(a) all the simulations yield on average lower response than the full scale measurements show. This sea state is also the one with the highest degree of uncertainty. The spread in standard deviations spans from 0.27 to 0.43 and may be a result of other environmental actions such as current and wind, i.e. the waves become less dominating. For higher H_S the situation is opposite. The simulations show a trend of overestimate the standard deviations a bit.

As shown in figure 5.15 we have some sea states where the dominating frequencies are the low frequencies. This is actually the case for many of the measured hours. But even for this extreme change in shape of the spectra the area below them are still not that different. The spread in standard deviation as shown in section 5.4.2 is relatively low. This will introduce an error if we use the standard deviation in finding the total cumulative damage. The simulations from RIFLEX never show these low frequencies. And the mean frequency will affect the damage in equation 4.9, accordingly.

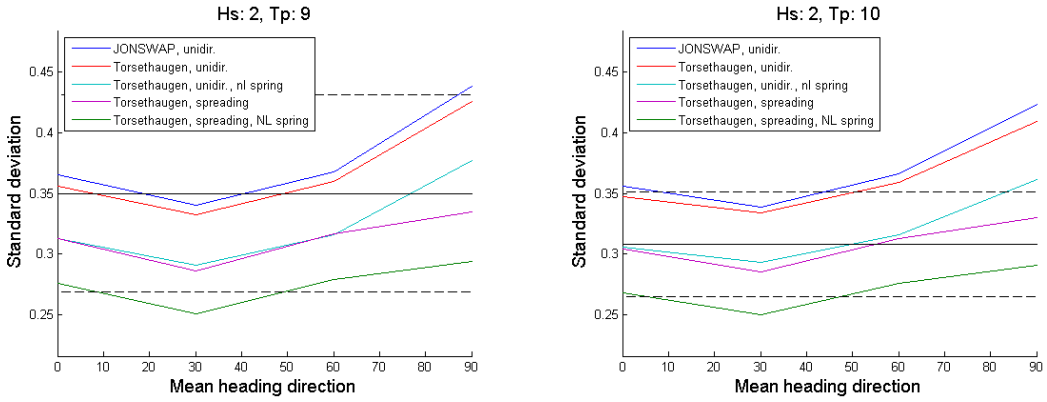

(a) H_S 2, T_P 9

(b) H_S 2, T_P 10

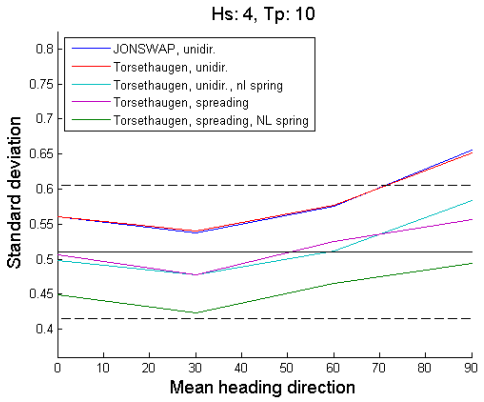

(c) H_S 4, T_P 10

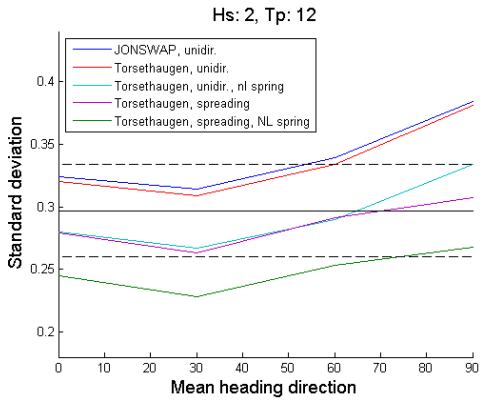

(d) H_S 2, T_P 12

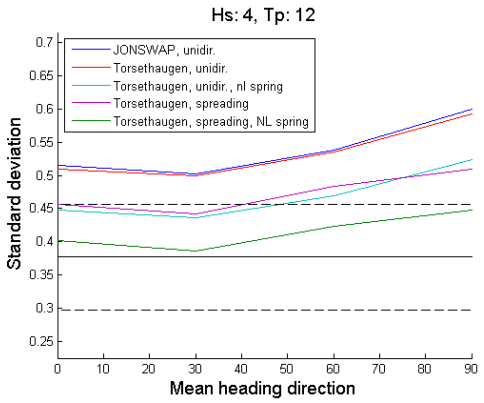

(e) H_S 4, T_P 12

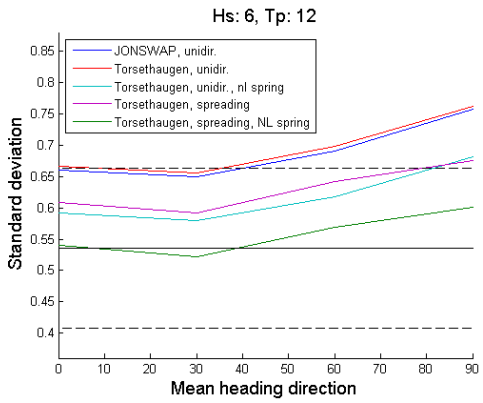

(f) H_S 6, T_P 12

Figure 8.1: Comparison of standard deviation from RIFLEX and full scale data. The horizontal solid black line is the averaged standard deviations from the full scale data and the dashed black lines are the statistical spreading of the standard deviation.

8.1.2 Miner-Palmgren Summation Comparison

By comparing the blocks in the Miner-Palmgren summation method we get a picture of the distribution of the number of cycles for each $\Delta\theta_i$. Ideally, the full scale measurements and the simulations from RIFLEX would have the same shape. The full scale distribution in a linear-log scale is very close to linear, i.e. a Weibull shape parameter, h close to 1.0. The results from RIFLEX have a higher shape parameter, but a lower maximum $\Delta\theta$. The shapes from RIFLEX are close to the same for all simulations and the implementation of non-linear flex joint and wave spreading is not enough to change the shape drastically. We can see that the maximum $\Delta\theta$ is reduced for the models with wave spreading and non-linear flex joint which is in accordance with the comparison of the standard deviations where we can see a reduction in the angle response.

Model	Cumulative damage	Error
Full scale	0.002544	0 %
Unidirectional JONSWAP waves	0.005817	129 %
Unidirectional Torsethaugen waves	0.006047	138 %
Unidirectional Torsethaugen waves with non-linear spring	0.003713	46 %
Torsethaugen waves with spreading	0.004495	77 %
Torsethaugen waves with spreading and non-linear spring	0.002719	7 %

Table 8.1: Cumulative damage for each simulation model compared to full scale damage using Miner-Palmgren summation

Figure 8.2 show how the different simulation compares to the full scale data directly. The data points for 4-directions shows the distribution when we take into account that the mean wave heading direction changes over time. The 1-direction points shows the distribution when we don't take into account the change in wave heading direction. We can clearly see a shift of the point between these two situations. When using RIFLEX to calculate the cumulative damage it is conservative to assume no change in weather direction since the main response direction is nearly the same as the incoming wave direction (see figure 5.5) which will give more damage at the same point regardless of the true response direction. In the full scale analyses we found that there is little to no relation between the response main direction and the weather direction. This comes from the fact that the ratio between the maximum standard deviation and the minimum standard deviation is very high, often close to 1.0.

Even though there are some differences in the angle spectra they are all very close when it comes to the total number of cycles, n_0. For some RIFLEX analyses there are some small amplitude cycles which appears under the rainflow counting, e.g. the high total number of cycles for 4-directions in figure 8.2(a). The relevance is very small since the total cumulative damage contribution is completely negligible for those cycles, i.e. that block in the Miner-Palmgren sum is as low as 10^{-45} in some cases.

We found in section 5.4.5 that the main contribution to the cumulative damage is from $\Delta\theta$ ranges between ~1 – 4 degrees. Compared to full scale fatigue using Miner-Palmgren

summation we have managed to narrow the gap. Table 8.1 shows the cumulative damage for the simulation models compared to full scale cumulative damage where the cumulative full scale damage is for the direction most damaged.

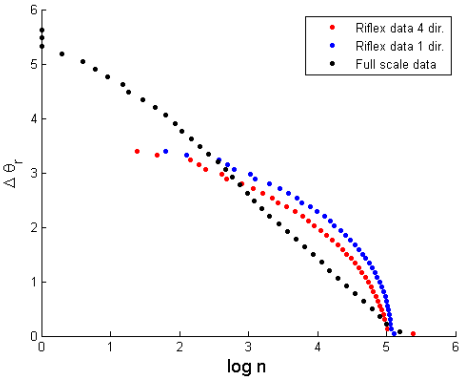

(a) Unidirectional JONSWAP waves

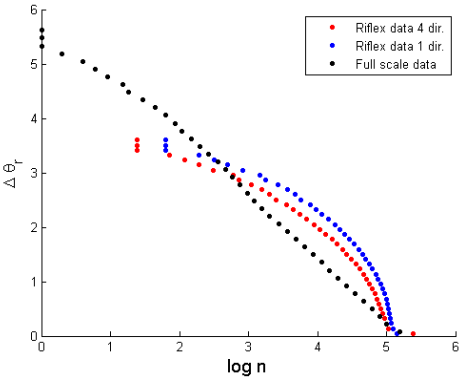

(b) Unidirectional Torsethaugen waves

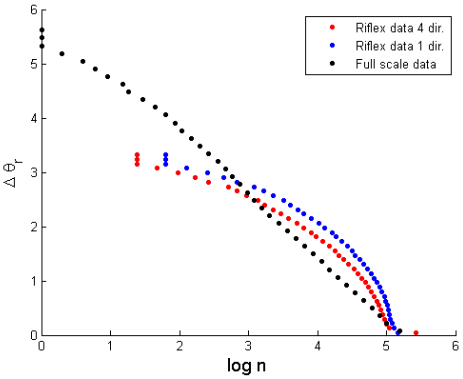

(c) Unidirectional Torsethaugen waves with non-linear flex joint

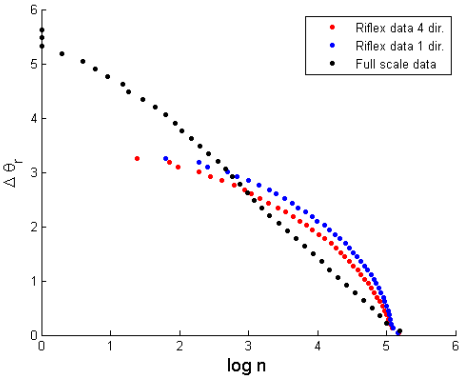

(d) Torsethaugen waves with spreading

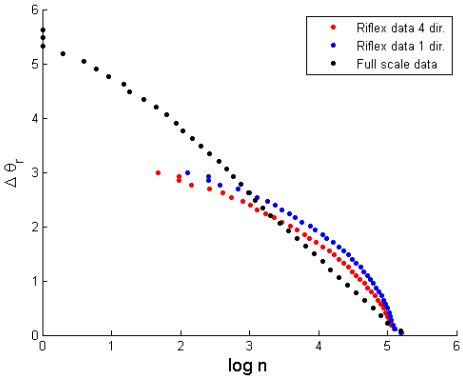

(e) Torsethaugen waves with spreading and non-linear flex joint

Figure 8.2: Comparison between the Miner-Palmgren summation blocks from RIFLEX and full scale analyses

8.1.3 Weibull Fit Damage Comparison

For all simulations and the full scale data we fitted a Weibull distribution to the angle range spectra. The full scale data had a shape parameter close to 1.0, whereas the simulations had much higher shape parameters, i.e. around 2.0.

Model	Cumulative damage	Error
Full scale	0.003201	0 %
Unidirectional JONSWAP waves	0.008821	176 %
Unidirectional Torsethaugen waves	0.005880	83 %
Unidirectional Torsethaugen waves with non-linear spring	0.003651	14 %
Torsethaugen waves with spreading	0.004502	41 %
Torsethaugen waves with spreading and non-linear spring	0.002770	−16 %

Table 8.2: Cumulative damage for each simulation model compared to full scale damage using closed form Weibull solution

Compared to using the Miner-Palmgren summation method we now get larger errors compared to the full scale measurements. The shape of the Weibull fit seems good, but it does not account for the cut-off of the peaks that is not represented by the RIFLEX simulations. And the fact that the largest peak $\Delta\theta_0$ in the RIFLEX analyses are all lower than the full scale analyses introduce another problem. We want to reduce the damage from the RIFLEX analyses, but the main contribution to the damage is not in the peak region of the spectra. The share of the cumulative damage comes from the region where the RIFLEX Weibull fit overestimates the cycle counts which is in the region between 0° and 3°.

If we compare the Weibull fit damage values to the Miner-Palmgren sum we get very close results. The results are to a large degree very comparable. This results are very close for the last four cases.

Model	Cumulative damage	
	Miner-Palmgren summation	Weibull fit
Full scale	0.002544	0.003201
Unidirectional JONSWAP waves	0.005817	0.008821
Unidirectional Torsethaugen waves	0.006047	0.005880
Unidirectional Torsethaugen waves with non-linear spring	0.003713	0.003651
Torsethaugen waves with spreading	0.004495	0.004502
Torsethaugen waves with spreading and non-linear spring	0.002719	0.002770

Table 8.3: Comparison of Miner-Palmgren sum damage and Weibull fit closed form solution damage.

8.1.4 Short-term Angle Spectrum Comparison

From the full scale measurement we found that the angle range spectrum changes when the angle motion is dominated by low frequencies outside the wave frequency range. The simulations from RIFLEX do not contain information about the rig's low frequency motion or characteristics. If this was implemented into the model it would be easier to compare the full scale measurements and computer simulations directly. By finding time series that have low energy in the low frequency region we can determine if this is a factor that should be considered more closely.

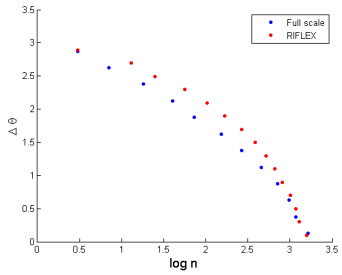

(a) Unidirectional JONSWAP waves

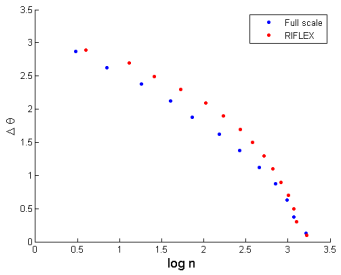

(b) Unidirectional Torsethaugen waves

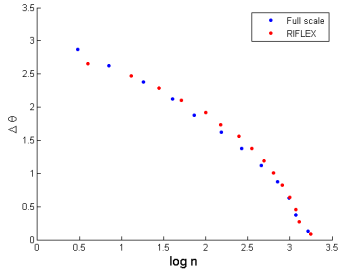

(c) Unidirectional Torsethaugen waves with non-linear flex joint

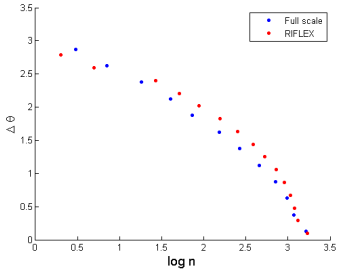

(d) Torsethaugen waves with spreading

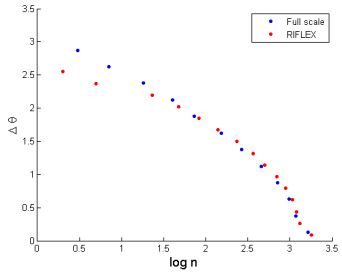

(e) Torsethaugen waves with spreading and non-linear flex joint

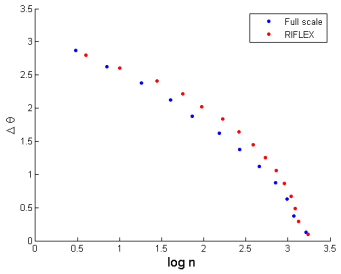

(f) Torsethaugen waves with current

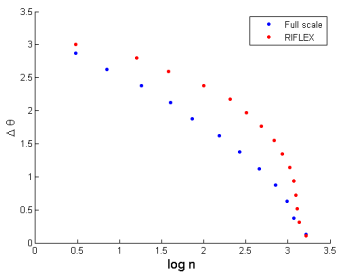

(g) Torsethaugen waves with rig offset

Figure 8.3: Comparison between short-term angle range spectra between full scale and computer simulations. The simulation time is 3 hours and all time series have the same sea state parameters. $H_S = 4$ m, $T_P = 10$ s.

8.1.5 Spectrum and Spectrum Broadness

The broadness parameter for a power spectrum ϵ gives a picture of the variety of frequencies represented in the realisation of the angle motion. The broadness parameter can be used to find a reduction factor for the cumulative damage if we find the damage assuming a narrow band process. The correction factor will then correct the actual damage by taking into account for the facts that the process isn't narrow banded.

From full scale analyses we found that the broadness is very high. The distribution is shown in figure 5.16(b) and spans from 0.5 to almost 1.0. Depending on the slope in the θ-N curve we can assume a completely broad process if the broadness is over ~0.5 where the inverse slope m is 5 and over ~0.7 where the inverse slope m is 3 (see figure 4.2). This mean that we can assume for almost all measured sea states in full scale can be assumed to have full broadness.

From the RIFLEX analyses we have found that the broadness parameter almost never reaches below 0.6. The broadness for most cases are, in fact, very close to 1.0. Using the same logic explained above we can use the same assumption for the broadness for our RIFLEX analyses, i.e. when calculating fatigue from narrow band process theory we can correct the fatigue with a correction factor where $\epsilon = 1.0$.

When comparing the power spectra for the angle response we do see some differences. The peak period for the full scale analyses are in many cases very high. Sometimes the peak period can be on the order of minutes.

8.2 Result Assessment

8.2.1 Modification of the Model

We have seen that the introduction of wave spreading and non-linear effects on the Lower Flex Joint will reduce the response and the cumulative damage. However, there are some differences that cannot go unnoticed. The reduction of fatigue is a result of the generic trend of reducing the standard deviation of the motion. The fatigue result was only 7 % above the full scale fatigue analyses. Due to the large difference in the shape of the Weibull fit this should be regarded as a coincidence. By taking into account the spreading of waves and different incoming heading directions we take away much of the conservatism of the environmental actions. Also introducing non-linear effects with higher tangential stiffness for small angles also takes away much of the conservatism.

8.2.2 Long-Term Angle Range Spectrum Differences

The shape of the angle range spectrum is very different between the full scale analyses and the simulations of the system. There is an over-representation of cycles in the

small-range region and an under-representation of cycles in the large-range region. This is an indication of a model that doesn't represent the true full scale situation.

The total number of cycles n_0 are at least on the same order of magnitude, but the number of cycles exceeding range above ~1° is too high. We showed in figure 5.20 that this is the most vulnerable region for the full scale damage, and this is even higher for the simulations. From figure 8.2 the difference is largest for the original model without modification than for the model with non-linear flex joint and wave spreading.

8.2.3 Short-term Angle Range Spectrum Differences

To isolate time series which can be compared directly to full scale measurements we found time series which were not dominated by low frequencies in the power spectrum. In most cases the computer simulation over-estimated the number of cycles for each $\Delta\theta$ except in the highest region where the full scale measurements had some higher peaks. Especially in the current simulation we can detect very large dependencies of the angle range spectra's shape on the current strength. Higher current velocities "flattened" the shape making it similar to the full scale spectrum where the low frequency energy was low.

8.2.4 Support Vessel Motion

The transfer function for the support vessel is linear, i.e. the motion of the support vessel is proportional to the amplitude of the excitation force. For a semi-submersible rig one may get higher order effects in different ways. The wave elevation will give pressure forces on the structure above the mean sea water line on a wave crest, and no pressure forces below on a wave trough. Another effect is the frequency difference effect due to Bernoulli's velocity term explained in section 6.6.1. Mean drift forces and slowly oscillating motions can be important for moored structures where the horizontal eigenfrequencies may be on the order of minutes. We have shown from the spectral analyses for the angle at the bottom of the riser that low frequencies can be governing. This effect may be a direct result of the motion of the support vessel. Full scale measurements from the semi-submersible "Uncle John" have shown that the motion of the rig often is dominated by low frequencies outside the wave frequency domain (Jackson and Wilson, 1988).

RIFLEX is able to use low frequency motion spectra when simulating the full motion of the support vessel. While the direct wave frequency motion has a certain phase with respect to the incoming waves the low frequency motion is random (Marintek, 2010). One can also import direct full scale measurement of the support vessel motion into RIFLEX, but without the exact wave realisation the simulation must be run without waves. This would still give an important understanding of the angle response of the riser, but the combined effect would still be missing. However, such low frequency data or rig response is not used in our analyses.

8.2.5 True Non-Linear Flex Joint

The true characteristics of the flex joint in a dynamic context are far more complex than what is shown in figure 6.7. Representing the non-linearities in a good way requires more investigation of the true characteristics. Dynamic stiffness and damping can be represented by a combination of parallel and serial coupled springs and dashpots.

The stiffness can differ from the static stiffness and in many cases the stiffness is higher. The results from our support vessel offset analyses showed an increasing tendency of the angular motion (see section 7.7). This is a result of the change in tangential stiffness for angles different than zero. If the true tangential (or equivalent) stiffness is higher, then those results can give a wrong picture of the true behaviour.

8.2.6 Wave Spreading

Spreading the energy of the incoming waves to a wider range of directions will give a reduction of the response. There is a generic tendency of higher directional energy concentration for high sea states, i.e. a higher exponent in the cosine wave spreading formula, equation 6.16. There are large uncertainties involved in this exponent. It changes from field to field and from day to day. Using an exponent proportional to the significant wave height H_S was used to mimic the concentration effect. For sea states with low H_S the waves can be either wind sea or swell sea and sometimes a combination. But the uncertainty of the exponent spreading parameter is also linked to the type of waves. From the full scale data we have seen that the angle motion is larger than expected for calm sea states. This may be an explanation to why the calculated standard deviations from the simulations are underestimated. The true motion may be dominated by slowly varying oscillations which isn't included in the models.

8.2.7 Current

The presence of current will reduce the motion of the system. The coupling of the terms in the velocity in Morison's equation will give a dominant static force, i.e. from the current contribution of the total force. From the results we have shown that the current introduce a significant damping to the angular motion both when the current has the same direction as the incoming waves and when the current direction is perpendicular to the wave direction. We could also take the Coriolis spiral into account to find the effect of that as well.

In all our analyses where we took a closer look at the damage we didn't have any simulations with current. Current could have a positive damping effect which in turn could "reshape" the angle range spectrum into our favour.

8.2.8 Heave Compensator behaviour

The heave compensator has been modelled with a constant stiffness. Natural variation in the tension forces will occur. The system may be *slow*, meaning that it need time to enter equilibrium. In a dynamic case this may cause lag in the tension forces. The tension force is an important part of the forces acting on the wellhead.

Conclusion

The target has been to compare the response of the marine riser between measured full scale response and computer simulated models using the simulation software RIFLEX. The measured angular response data has been coupled to weather hindcast data from the Norwegian Reanalysis (NORA10) data. The comparison was made by comparing the standard deviation of the response and by comparing the angle range spectra in order to find the cumulative damage.

The scattering of standard deviation from the full scale data was fairly small compared to the differences in the angular power spectra. The energy of the motion which is directly linked to the area under the power spectra curve was in other words similar in almost all full scale measurements whether the motion was low frequency dominated or dominated by frequencies in the wave-domain. The simulations showed that the standard deviations were within natural variations of the measured standard deviations. There was a tendency of under-estimation of the standard deviation for the sea states with the smallest significant wave heights. For sea states with lower H_S we observed that the uncertainty of the standard deviations were higher than for sea states with higher H_S. A possible explanation is that the low frequency oscillation of the rig may be even more dominant for those sea states than for the higher sea states. Since the exponent may also be linked to whether the sea state is swell dominated or wind dominated we introduce another uncertainty since we didn't take this into account when performing the analyses.

After modelling with spreading of the waves and a non-linear flex joint we have managed to reduce the response of the angle. This is as expected, but the characteristics of the motion and the shape of the angle range spectra are far from comparable to the full scale distribution.

By taking away some of the conservatism in our model the calculated cumulative damage using the Miner-Palmgren summation method we are closer to the measured damage. However, the shape of the angle range spectra affects each block in the summation to a very large degree. Narrowing of the gap between full scale damage and simulation damage should be considered to be a coincidence and not necessarily a result of "correct" simulations.

For the angle range spectrum for full scale measurements we found that the Weibull parameter h is very close to 1.0, which is typical for long term, environmentally loaded offshore structures. For the angle range spectra from the RIFLEX simulation the shape

parameter varied from 1.79 to 2.0 when we assume changes in mean heading direction of the incoming waves. The lowest value correspond to the case where both non-linear flex joint and wave spreading were present and the highest correspond to the case where those effects aren't present.

For the standard deviations alone there are very little discrepancies compared to the full scale data. The calculated values are within the natural variances of the full scale data. This is also found in the literature when they compare the standard deviation of an arbitrary motion and the match becomes better for motion measured away from the wave-active zone.

Before using these calculation methods to document any fatigue life time on wellheads it is recommended that the gap in the angle range spectra are closed. It is clear that the current effect and the low frequency motion of the rig can affect the results significantly. Further analyses should be made to identify effects that yet are unaccounted for.

Recommendations for Further Work

In this thesis we have found some discrepancies between measured and calculated response for the angle of the riser at the lower flex joint. The results are comparable when investigating the standard deviation of the motion and the fatigue life there are some aspects that need further investigations before we can use this kind of computer simulations to assess the fatigue life time of the wellhead.

The angle range spectrums that we used to find the cumulative damage with the Miner-Palmgren summation method are very different in the real world and in the simulations. In this thesis we only looked at removing conservatism using wave spreading instead of unidirectional waves and introducing a non-linear flex joint behaviour.

For further work it is recommended that a more realistic model of the non-linearities are taken into the RIFLEX model, i.e. stiffness and damping hysteresis data so that both static and dynamic effects are properly modelled. We have already shown that changing the properties will introduce significant changes in the results and more realistic models would help getting better results.

As one of the discussed papers pointed out there may be some effects from the values in Morison's equation that may vary due to change in Reynolds number and Keulegan-Carpenter number along the length of the riser. The changes in drag coefficient and mass coefficient could alter the results significantly. These effects are also coupled to the damping effect when a current is present.

The slowly varying oscillation of the support vessel is also an important factor to investigate. We've shown that a large portion of the full scale spectra are low frequency dominated. This was also pointed out in one of the papers in the literature review which also was based on a semi-submersible rig. Allowing the rig to slowly drift away from its equilibrium point with its mooring can give some larger peaks in the spectra which we miss in our analyses.

Also, we have assumed no current at all in our analyses which may be a severely bad assumption. The current will reduce the response of the angle, but the effect it has on the angle range spectrum is still unknown.

References

4Subsea (2012). Rex measurement system description.

Almar-Næss, A., Andersson, H., Bardal, E., Berge, S., Engesvik, K., Fines, S., Gibstein, M. B., Haagensen, P. J., andJon Lereim, A. K., Lotsberg, I., Moan, T., Moe, E. T., Slatcher, S., and Wästberg, S. (1985). *Fatigue Handbook - Offshore Steel Structures*. Tapir.

Anzai, H. and Endo, T. (1979). On-site indication of fatigue damage under complex loading. *International Journal of Fatigue*, 1:49–57.

Ariduru, S. (2004). Fatigue calculation by rainflow cycle counting method. Master's thesis, The Graduate School of Natural and Applied Sciences of Middle East Technical University.

Cartwright, D. E. and Longuet-Higgins, M. S. (1956). The statistical distribution of the maxima of a random function. *National Institute of Oceanography*.

Connolly, J. and Wybro, P. (1984). Riser analysis methods: Comparison with measured field data. *Offshore Technology Conference*.

DNV (2010). Offshore standard dnv-os-f201 - dynamic risers.

Faltinsen, O. M. (1990). *Sea Loads on Ships and Offshore Structures*. University of Cambridge.

Framnes, E. and Gleditsch, S. (1994). *Boreplattformen med utstyr*. Vett & Viten.

Hamedani, G. G. and Tata, M. N. (1975). On the determination of the bivariate normal distribution from distribution of linear combinations of the variables. *The American Methematical Monthly*, 82:913–915.

Holden, H. (2012). Correspondence. E-mail.

Jackson, G. and Wilson, D. (1988). Full-scale measurements on the semisubmersible 'uncle john'. *Offshore Technology Conference*.

Kvitrud, A. (1996). Wave kinematics reduction factor for north sea applications. *http://home.c2i.net/kvitrud/Arne/kinematic-reduction-factor.htm*.

Marintek (2010). *RIFLEX User's Manual*. Sintef.

Marintek (2011). *RIFLEX Theory Manual*. Sintef.

Myrhaug, D. (2005). *Statistics of narrow band processes and equivalent linearization*. Department of Marine Technology, NTNU.

Myrhaug, D. (2007). *Marin Dynamikk - Uregelmessig sjo*. Institutt for Marin Teknikk, NTNU.

Newland, D. (1993). *An introduction to random vibrations, spectral and wavelet analysis*.

NORSOK (2007). Norsok standard n-003 - actions and action effects.

Pytte, T. (2012). Correspondence. E-mail.

Sødahl, N., Hanson, T., Ottersen, A., and Fylling, I. (1992). Influence from nonelastic material modelling in computer simulation of flexible riser system verified by full-scale measurements. *Offshore Technology Conference*.

Sparks, C. P. (2007). *Fundamentals of Marine Riser Mechanics*. PennWell Corporation.

Torsethaugen, K. and Haver, S. (2004). Simplified double peak spectral model for ocean waves. *SINTEF/STATOIL*.

Verbeek, P. (1983). Analysis of riser measurements in the north sea. *Offshore Technology Conference*.

WAFO-group (2000). *WAFO - A Matlab Toolbox for Analysis of Random Waves and Loads - A Tutorial*. Math. Stat., Center for Math. Sci., Lund Univ., Lund, Sweden. http://www.maths.lth.se/matstat/wafo.

Wikipedia (2012). Blowout preventer. http://en.wikipedia.org/wiki/Blowout_preventer.

Øyvind Breivik, Reistad, M., and Haakenstad, H. (2011). A high-resolution hindcast study for the north sea, the norwegian sea and the barents sea. *Journal of Geophysical Research*, 116.

Appendix A

Marine Riser Static Displacement

Segmented Riser

Curvature and Displacements

Data	
Top end offset, y_t (m)	**27,38**
Top tension, T_t (kN)	**950**
Attention: LOW Tension, Tt/wL <1.2	
Moment top end (kN-m)	**0**
Moment btm end (kN-m)	**-193,87**

Deduced values	
Total app. weight (kN)	-364
Btm end tension (kN)	1 314
T_t / ΣwL	-2,61
Max. tension (kN)	1 337
Min. tension (kN)	834

				Drag coeff. C_d	**0,8**
Data per segment	**App.wt** (kN/m)	**Length** (m)	**Stiffness** EI (kN-m²)	**Diam.** ϕ (m)	**Current velocity** (m/s)	**Mid-pt. load** (kN/m)
Segment 1 (top end)	**1,418**	**10,079**	**177 310**	**0,563**	**0,00**	0,000
Segment 2	**3,706**	**1,200**	**137 700**	**1,533**	**0,00**	0,000
Segment 3	**3,706**	**20,826**	**267 670**	**0,69**	**0,00**	0,000
Segment 4	**1,494**	**13,716**	**177 310**	**0,512**	**0,00**	0,000
Segment 5	**-1,836**	**274,320**	**177 310**	**0,993**	**0,00**	0,000
Segment 6 (bottom end)	**1,494**	**15,240**	**177 310**	**0,512**	**0,00**	0,000
	Total:	335	**Bottom end current :**		**0,00**	

Global results	**Riser** (numerical)	**Cable** (analytical)
Top end angles	**5,38°**	**5,15°**
Bottom end angles	**3,00°**	**3,72°**
Maximum sag (m)	**1,84**	**1,78**
Height of maximum sag x/L	**0,503**	**0,520**
Top end setdown (m)	**1,143**	**1,142**
Top end reaction H_t (kN)	**-85,92**	**-85,42**
Bottom end reaction H_b (kN)	**85,92**	**85,42**

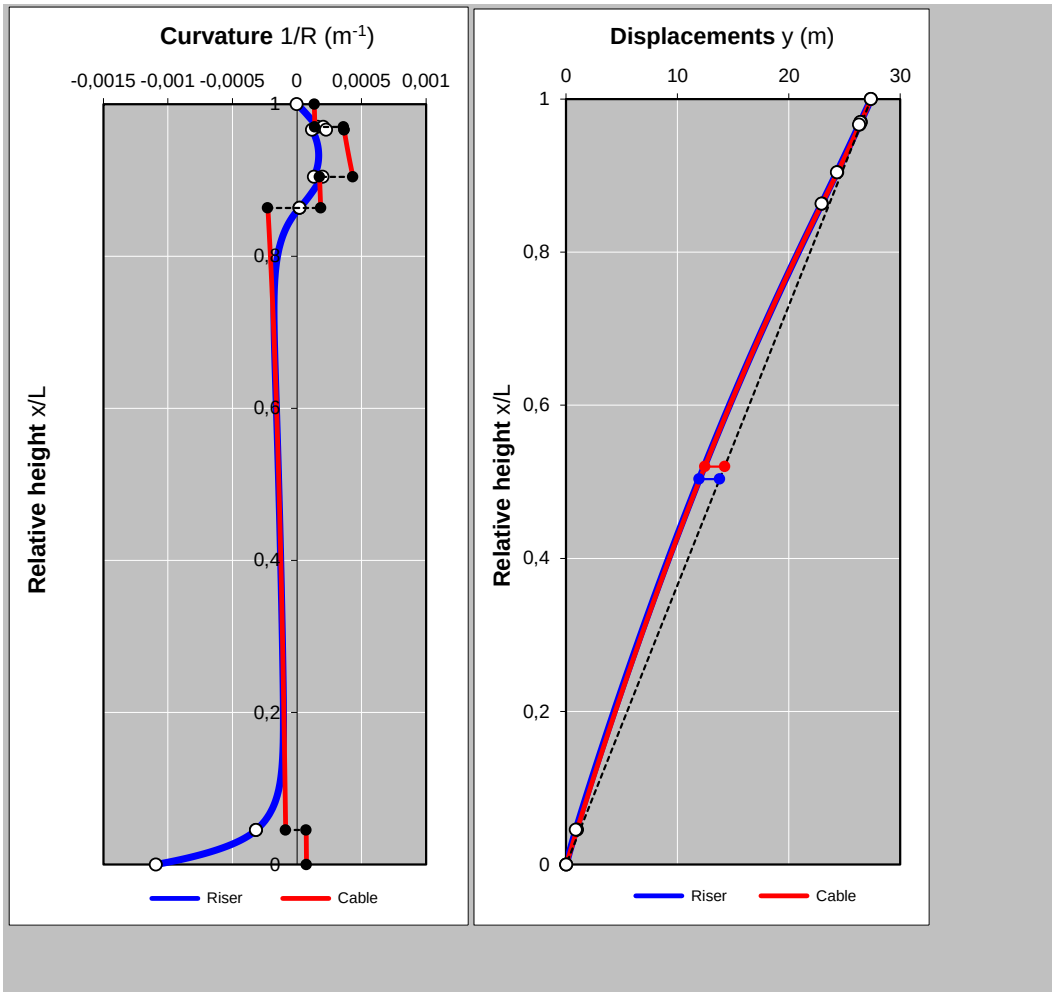
Curvature 1/R (m-1)
-0,0015 -0,001 -0,0005 0 0,0005 0,001
1
0,8
0,6
0,4
0,2
0
Relative height x/L
Riser
Cable
Displacements y (m)
0 10 20 30
1
0,8
0,6
0,4
0,2
0
Relative height x/L
Riser
Cable

Appendix B

Tabulated θ-N Curve Values

Δθ	N	Δθ	N	Δθ	N
30	821	4,041576	333044	1,959552	6175332
6,062364	98006	3,98034	348888	1,898316	7247208
6,001128	101027	3,919104	365749	1,83708	8549891
5,939892	104174	3,857868	383709	1,775844	10142629
5,878656	107452	3,796632	402861	1,714608	12104411
5,81742	110870	3,735396	423303	1,653372	14538843
5,756184	114434	3,67416	445147	1,592136	17584095
5,694948	118153	3,612924	468423	1,5309	21426430
5,633712	122035	3,551688	493343	1,469664	26319875
5,572476	126089	3,490452	520058	1,408428	32615227
5,51124	130325	3,429216	548731	1,347192	40803530
5,450004	134776	3,36798	579545	1,285956	51582356
5,388768	139432	3,306744	612704	1,22472	65958773
5,327532	144305	3,245508	648434	1,163484	85404043
5,266296	149407	3,184272	686988	1,102248	112137746
5,20506	154753	3,123036	728652	1,041012	149550296
5,143824	160357	3,0618	773744	0,979776	202957520
5,082588	166235	3,000564	842999	0,91854	280921365
5,021352	172403	2,939328	920610	0,857304	397656783
4,960116	178880	2,878092	1007232	0,796068	577592346
4,89888	185685	2,816856	1104138	0,734832	864404157
4,837644	192907	2,75562	1212813	0,673596	1,33985E+09
4,776408	200508	2,694384	1334999	0,61236	2,16546E+09
4,715172	208514	2,633148	1472740	0,551124	3,68153E+09
4,653936	216949	2,571912	1628452	0,489888	6,66319E+09
4,5927	225845	2,510676	1804994	0,428652	1,30552E+10
4,531464	235232	2,44944	2005766	0,367416	2,83788E+10
4,470228	245145	2,388204	2277937	0,30618	7,10929E+10
4,408992	255622	2,326968	2596643	0,244944	2,18755E+11
4,347756	266702	2,265732	2970295	0,183708	9,31688E+11
4,28652	278430	2,204496	3410254	0,122472	7,18183E+12
4,225284	290895	2,14326	3930646	0,061236	2,35783E+14
4,164048	304114	2,082024	4549137	5,17366E-09	1,00000E+50
4,102812	318142	2,020788	5287970		